# A REVISED MODEL FOR DOSIMETRY IN THE HUMAN SMALL INTESTINE

## Final Progress Report

Submitted by:

John W. Poston, Sr., Professor
Nasir U. Bhuiyan
R. Alex Redd
Neil D. Parham
Jennifer A. Watson
Department of Nuclear Engineering
Texas A&M University
3133 TAMU
College Station, TX 77843-3133

To:

**The U.S. Department of Energy**
**Nuclear Engineering Education Research Program**
**Idaho Operations Office**

February 28, 2005

# ABSTRACT

A new model for an adult human gastrointestinal tract (GIT) has been developed for use in internal dose estimations to the wall of the GIT and to the other organs and tissues of the body from radionuclides deposited in the lumenal contents of the five sections of the GIT. These sections were the esophagus, stomach, small intestine, upper large intestine, and the lower large intestine. The wall of each section was separated from its lumenal contents. Each wall was divided into many small regions so that the histologic and radiosensitive variations of the tissues across the wall could be distinguished. The characteristic parameters were determined based on the newest information available in the literature. Each of these sections except the stomach was subdivided into multiple subsections to include the spatiotemporal variations in the shape and characteristic parameters. This new GIT was integrated into an anthropomorphic phantom representing both an adult male and a larger-than-average adult female. The current phantom contains 14 different types of tissue. This phantom was coupled with the MCNP 4C Monte Carlo simulation package. The initial design and coding of the phantom and the Monte Carlo treatment employed in this study were validated using the results obtained by Cristy and Eckerman (1987). The code was used for calculating specific absorbed fractions (SAFs) in various organs and radiosensitive tissues from uniformly distributed sources of fifteen monoenergetic photons and electrons, 10 keV - 4 MeV, in the lumenal contents of the five sections of the GIT. The present studies showed that the average photon SAFs to the walls were significantly different from that to the radiosensitive cells (stem cells) for the energies below 50 keV. Above 50 keV, the photon SAFs were found to be almost constant across the walls. The electron SAF at the depth of the stem cells was a small fraction of the SAF routinely estimated at the contents-mucus interface. Electron studies showed that the “self-dose” for the energies below 300 keV and the “cross-dose” below 2 MeV were only from bremsstrahlung and fluorescent radiations at the depth of the stem cells and were not important.

## INTRODUCTION

Research was undertaken at Texas A&M University to improve the model used to estimate dose due to internally deposited radionuclides in the small intestine. The current model is simply a large tissue region with no definition of the wall and the contents of the intestine. This effort remodeled the small intestine based on present anatomical and histological information. The revised model attempted to represent the many folds found in the small intestine and separated the wall and contents in the lumen so that the more radiosensitive cells could be distinguished from the more radioresistant cells in the wall. The research goal was to use the revised model in calculations of the absorbed fractions of energy (AF) and the specific absorbed fractions of energy (SAF) for monoenergetic photon and electrons sources with energies ranging from 0.005 to 5 MeV. In addition, it was planned that these results would be used to modify currently accepted values of the annual limit on intake (ALI) when the small intestine is the "limiting organ." That is, in the ICRP approach to establishing the ALI for a radionuclide, there are situations in which the ALI is based on the 0.5 Sv committed dose equivalent to a single organ rather than the 0.05 Sv committed effective dose equivalent. Once these new ALI values were obtained, new derived air concentrations for these radionuclides can be calculated. This report summarizes the results of this research.

## A BRIEF REVIEW OF GASTROINTESTINAL TRACT (GIT) MODELS

Over the years, many changes have been made to the individual organ models of the original Snyder phantom (Snyder et al. 1974) to make the models more realistic. But the GIT model remained essentially the same since the model was developed by Snyder et al. in 1974. The small intestine (SI) was modeled as a solid soft tissue region without delineation of the wall and its contents. The many folds found in the SI were not considered in this model and the old model was simply a volume of tissue occupying the appropriate space inside the human body. The other three sections of the GIT, the stomach (ST), the upper large intestine (ULI) and the lower large intestine (LLI), were modeled as "organs with walls and contents." The entire wall of each of these sections was treated as a single tissue layer. Thus, only average quantities (e.g., average dose, average SAF, etc.) to the wall could be obtained using this model. The results of these calculations did not provide a dose distribution across the wall. The dose distribution information was important for two reasons: tissues forming the wall have varying degrees of radiosensitivity and the locations of these tissues vary within and between individuals.

The epithelial cells, lining the GIT mucosa, are believed to be at risk for radiation induced malignancy as these cells are the most radiosensitive cells in the wall. The distinction among the tissue types in the wall may not have been important in the earlier models because those were used only for photon dose calculations. Dose variations across the wall were not significant for photons if the wall thickness was smaller than the mean free paths of the photons under consideration, i.e., for the photon energies >15

keV. But for the weakly-penetrating radiations (beta, conversion electrons, Auger electrons, low-energy x-rays), the dose varies significantly because of the limited range of these radiations in tissue. Bhuiyan (2000) showed that the dose varies by several orders of magnitude over a small fraction of a centimeter of wall thickness for low-energy electrons.

Obviously, the earlier models were not suitable for electron dose calculations. It should be noted that the photon-induced electrons (secondary electrons) also were not transported in the early calculations for photon sources. The energies of the secondary electrons were assumed to be locally deposited. This assumption was reasonable and Poston et al. (1996b) showed electron transport was not important in most photon transport calculations.

For a very long time, no attempt was made to perform calculations for electron-emitting sources deposited in the lumen contents of the GIT because of the difficulties in modeling the complex structure of GIT and the complexity in the electron transport calculations. The International Commission on Radiological Protection (ICRP) "one-half assumption" (1979) continued to be used for estimates of dose from weakly-penetrating sources in the lumen of walled organs. This assumption states that the absorbed fraction of energy (AF) for sections of the GIT is one-half and the specific absorbed fraction (SAF) is simply the AF divided by the mass of the contents (not the mass of the GIT wall). The factor of one-half was introduced "because the dose at the surface of the contents will be approximately half that within their volume for np radiations." (ICRP 1979). In addition, parameter called "υ" was introduced to represent "the degree to

which these radiations penetrate the mucus." (ICRP 1979). For β radiation, υ was taken to be unity and for α radiation and fission fragments, υ was assumed to be 0.01 (ICRP 1979).

Many calculations, including those for the ICRP and the Medical Internal Radiation Dose (MIRD) Committee, were based on the above assumption. Recent calculations using the GIT models with Monte Carlo electron transport codes showed that this assumption for the walled organs was overly simplified for many useful electron energies (< 500 keV) (Poston et al. 1996b, Stubbs et al. 1998, Bhuiyan 2000). With the development of improved radiation transport codes, especially those available to transport beta and electron radiation, many difficult modeling tasks were revisited.

Poston et al. (1996a) described a model of the GIT for use in dose calculations for radiation uniformly distributed in the contents of the GIT. The goal of their research was to define the sensitive cell region in the tract. This simple model was comprised of right circular cylinders representing sections of the tract located inside the heterogeneous phantom. Sections of the tract wall were defined by 10 regions, each 100-μm thick, over the region from the wall-contents interface to 1,000 μm. These models were used in the calculation of photon and electron absorbed fractions for a number of discrete energies. The annual limit on intake (ALI) for a single radionuclide was recalculated to demonstrate the effect of the improved absorbed fraction values on internal dose assessment. In this specific case, the revised ALI was a factor of three higher (less restrictive) than the value in ICRP Publication 30 (1979). However, even though there were a number of radionuclides for which the committed dose equivalent to a section of

the GIT was the "controlling organ," no additional calculations were made. The effects of this GIT model on the other organs also were not investigated.

Stubbs et al. (1998) modeled the GIT for use in calculating radiation absorbed dose to the wall. In this model, the GIT was composed of three isolated sections — the ST, SI, and large intestine or colon — surrounded by vacuum. The contents and wall of each section were defined. The wall plus contents of the SI and the colon were represented as two coaxial circular cylinders 10 cm in length. The volume within the inner cylinder represented the lumen. The volume between the inner and the outer cylinders represented the wall. The lumen radii and the wall thicknesses were taken from the anatomical data for the ICRP Reference Man (1975). The same Cristy and Eckerman adult ST model (1987) was used. The organ walls were divided into many small segments so that Monte Carlo simulation results could be obtained practically at any point in the wall. Stubbs and his colleagues concluded, as did Poston et al. (1996a, 1996b), that the ICRP assumption for weakly-penetrating radiations for hollow organs is overly conservative. They used this model to calculate the "S values" (in units of Gy/Bq-s) as a function of distance from the contents-mucus interface for four radionuclides important in nuclear medicine. The radionuclides were Y-90, Tc-99m, I-123, and I-131.

More recently, an improved, but very simple, geometric model for the SI has been developed and used in the study of electron energy deposition in the wall. Bhuiyan modeled the SI as a 10 cm long isolated segment surrounded by void and described the SI model by a set of right circular cylinders (Bhuiyan 2000; Bhuiyan and Poston 2005). The lumen was assumed to be full of contents. Results were obtained using this model,

and the MCNP4A Monte Carlo simulation package (Briesmeister 1993), for more than 50 monoenergetic electron energies in the range 10 keV to 500 keV. The wall was divided into many small regions and a depth-dose profile was developed for each energy studied. Electron transport results showed that only a small fraction of the available energy reached the critical cells for monoenergetic electron sources in the contents of the tract ranging in energy from 10-500 keV. Normally, the absorbed dose at the wall-contents interface is reported as the dose to the wall. The results of these calculations indicated this practice should be discontinued and should be replaced by reporting the dose to the stem cell population. For electron energies below about 330 keV, the only contribution to the absorbed dose at the stem cell position came from bremsstrahlung. For higher energy electrons (i.e., 330 keV – 500 keV), the dose distribution curves were dominated by monoenergetic electrons at the stem cell depth.

Jönsson et al. (2002) presented an improved model of the SI for calculation of the absorbed dose to the radiosensitive crypt cells in the SI wall from sources in the wall and the contents. The absorbed dose calculation included contributions of both "self-dose" and "cross-dose" from neighboring loops; factors not incorporated before into dosimetric models of the SI. They simulated the SI by using 19 circular cylinders. These cylinders were hexagonally arranged. Each cylinder consisted of two concentric cylinders, where the inner cylinder, 2.5 cm in diameter, represented the contents and the volume between the inner and the outer represented the wall. They used two wall thicknesses, 0.3 cm and 0.6 cm, for the calculations. Each cylinder, except the cylinder located at the center of the hexagon, was 20 cm in length. The central cylinder was taken to be 3 m in length.

Sources were uniformly distributed in the contents and the walls. Total absorbed dose, obtained by adding the self-dose and the cross-dose from the sources in both wall and contents, were calculated only for the central cylinder. The calculations were performed, using the EGS4 Monte Carlo simulation package, for 10 monoenergetic electrons, 50 keV–10 MeV, and for the radionuclides $^{99m}$Tc, $^{111}$In, $^{131}$I, $^{67}$Ga, $^{90}$Y, and $^{211}$At. They found that the self-dose from the wall was considerably greater than the self-dose from the contents and the cross-dose from the wall and the contents except for high electron energies. For the radionuclides investigated and electrons in the range 100-200 keV and 8-10 MeV, the cross-dose was found to be higher than the self-dose from the contents.

The models described above have not provided a satisfactory rendition of the GIT. While the results obtained from these calculations provide significant insight into energy deposition in the wall, the fact remains that there was no comprehensive model of the GIT, especially the SI, for use in internal dose assessments for both electrons and photons for a broad spectrum of energies.

The calculations described above simulated only a small segment of the SI and ignored the influence of the "folded nature" of this section of the GIT. Therefore, a more complete model of the SI, as well as of the other sections of the GIT, is needed to bring dosimetry of these walled organs to the same level as that of other organs of the body. The esophagus (ESP) has not been considered as a section of the GIT in any of the GIT models developed thus far. The latest ICRP recommendations introduced specific risk estimates and tissue weighting factors, $w_T$, for radiation-induced cancer of the ES, ST and colon (ULI and LLI) (ICRP 1991), requiring dose estimations for these organs.

Thus, a careful effort has been undertaken to remodel the entire GIT with all histologic, anatomic, and physiologic features pertinent to both photon and electron dosimetry for all energies.

This new GIT model has five sections representing the ES, ST, SI, ULI, and LLI. The wall of each section is separated from its lumen contents. Sources are uniformly distributed in the contents. The contents and wall of each are divided into many small regions so that the dose distribution inside and outside of the source contents of various geometric shapes can be obtained. The shape, size, and the location for each section are more anatomically structured in this model. The characteristic parameters were determined based on the newest information available to better approximate the true anatomic values. Each section except the ST consists of a number of subsections so that the spatiotemporal variations in the structure can be delineated in the model. The model is described in detail in the next section.

## THE REVISED GASTROINTESTINAL TRACT MODEL

A new model for an adult human gastrointestinal tract (GIT) was developed for use in internal dose assessments for the body organs including the GIT from radioactive sources in the lumen contents. The new GIT model was intended for use in Monte Carlo transport calculations of both penetrating (gamma, x-rays) and weakly-penetrating radiations (beta, conversion electrons, Auger electrons) having any energy. The histologic, anatomic, and physiologic features of the GIT were investigated and features pertinent to both photon and electron dosimetry were incorporated into this GIT model.

This model was a significant improvement on the earlier models, discussed in the previous section.

The new GIT model was integrated into an anthropomorphic adult phantom which was similar but not identical to the adult male phantom of Cristy and Eckerman (1987). There were a number of differences between these two phantoms: (1) the new phantom was composed of fourteen different tissue types including the same three tissues used in the Cristy and Eckerman adult phantom (1987) for lung, skeleton and soft tissue; (2) a small portion of the heart that was intercepted by the esophagus was excluded; (3) the pancreas was shifted slightly to accommodate the duodenum; and (4) the GIT was redesigned to include more structural details pertinent to both photon and electron dosimetry. This phantom (Figs. 1-6) was surrounded by air instead of void as in the Cristy and Eckerman phantom (1987). Organs such as the adrenals, thymus, gall bladder, and spleen were not included in this phantom as these organs were not important for internal dose estimations.

The major difference between the two phantoms was in the GIT. The GIT model of Cristy and Eckerman (1987) was identical to that of Snyder et al. (1978) in which the small intestine (SI) was modeled as a solid soft tissue region without delineating the wall and the contents, or the folds that this organ takes in its position in the abdomen. The other sections — stomach (ST), upper large intestine (ULI) consisting of ascending colon (AC) and transverse colon (TC), and lower large intestine (LLI) consisting of descending colon (DC) and sigmoid-rectum colon (SRC) — were modeled as organs with walls and contents. Each wall was treated as a single tissue layer. A distinction

among the tissue types within the wall was not made because the Cristy and Eckerman phantom was designed for the photon dosimetry, not for electron dosimetry. Cristy and Eckerman considered primarily the total mass (wall plus contents) of a section in their model. The individual detail of the characteristic parameters such as the length, lumen diameter, wall thickness, and masses of the wall and contents were ignored. These values differed largely from the true anatomic data. It was noted that these parameters may have little effect on the energy deposition pattern for photons. But for the weakly-penetrating radiations, the effects were strong enough to require real anatomic data to be incorporated into the model (Bhuiyan 2000, Bhuiyan and Poston 2005).

The GIT model developed in this study was suitable for both electron and photon transport calculations. There were five sections, namely the esophagus (ESP), ST, SI, ULI, and LLI. The wall of each section was separated from its lumen contents. Each wall was divided into many small regions so that the more radiosensitive tissues could be distinguished from the less radiosensitive tissues. The epithelial cells lining the GIT mucosa were recognized as the cells at risk to radiation as these cells were the most radiosensitive cells in the wall and the epithelium was the location of radiation-induced malignant growths. The average stem cell depth, measured from the wall-contents interface, for each section was determined by reviewing the available histologic data. The shapes, sizes, and the locations of these sections were more anatomically structured. The characteristic parameters were determined based on the newest information available to better approximate the actual anatomic values. Each section, except the ST,

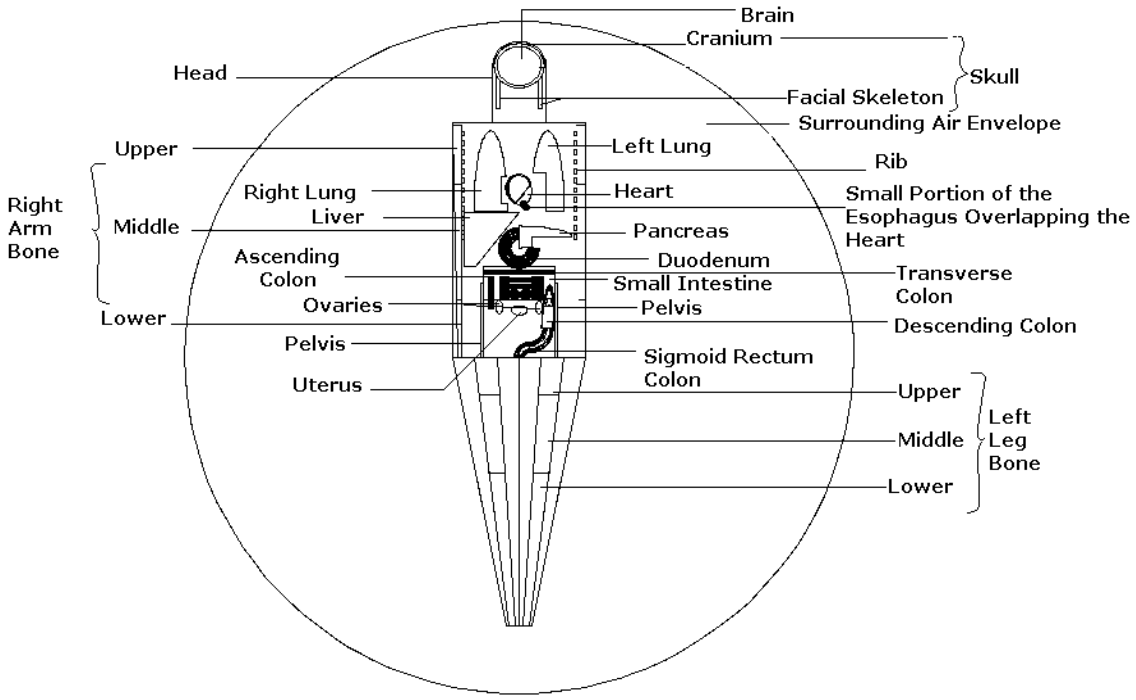


**Fig. 1.** Front view of the adult phantom developed in this study showing the principal organs in the head, trunk, and the legs. The phantom was sectioned along the coronal plane y = 0 in a reference frame centered at the base of the trunk. The positive y-axis is directed towards the posterior of the phantom, the positive x-axis is directed to the phantom's left (the reader's right in the figure), and the positive z-axis is directed toward the head of the phantom.

consisted of a number of subsections so that the spatiotemporal variations in the structure could be delineated in the model.

The spatiotemporal behavior of the ES was captured by dividing the section into three subsections — upper esophagus with closed lumen, middle esophagus with closed lumen, and lower esophagus with a full lumen — representing the states of the ESP at resting, contraction, and distension, respectively, observed during passage of a food bolus through the ESP (Fig. 2).

This was the first GIT model that included the ESP as a section of the GIT. A number of different models for the GIT for use in internal dose assessments have been proposed since the first GIT model developed by the ICRP in 1959. But, the ESP was not included in any of these models. The ESP was not considered as an organ at risk to radiation-induced cancer in the early ICRP recommendations. This might be the reason for not including the ESP as part of the GIT model for internal dosimetry. A relatively short transit time (~ 40 s per bolus) for the ESP lumen contents might be another reason. The latest ICRP recommendations introduced specific risk estimates and tissue weighting factors for many other organs (ICRP 1991), requiring dose estimations for all these organs.

Anatomically, a full ST assumes an oblique position between the ESP and the duodenum in erect posture (Warren 2000). Cristy and Eckerman (1987) modeled the ST as full but the organ was positioned upright on the left side of the transverse colon (TC) in their erect phantom. The ST in the new model inclines to the left at an angle of 45 degrees and reaches as far as the bottom of the left lung. It is moved to a new position between the ESP and the duodenum. The postero-superior surface of the stomach is in contact with the bottom of the ESP while the postero-inferior surface touches the antero-superior surface of the duodenum. The liver is on the right side of the ST. The wall and the contents of the stomach are defined by two concentric ellipsoids with the geometric factors identical to the Cristy and Eckerman ST model (1987).

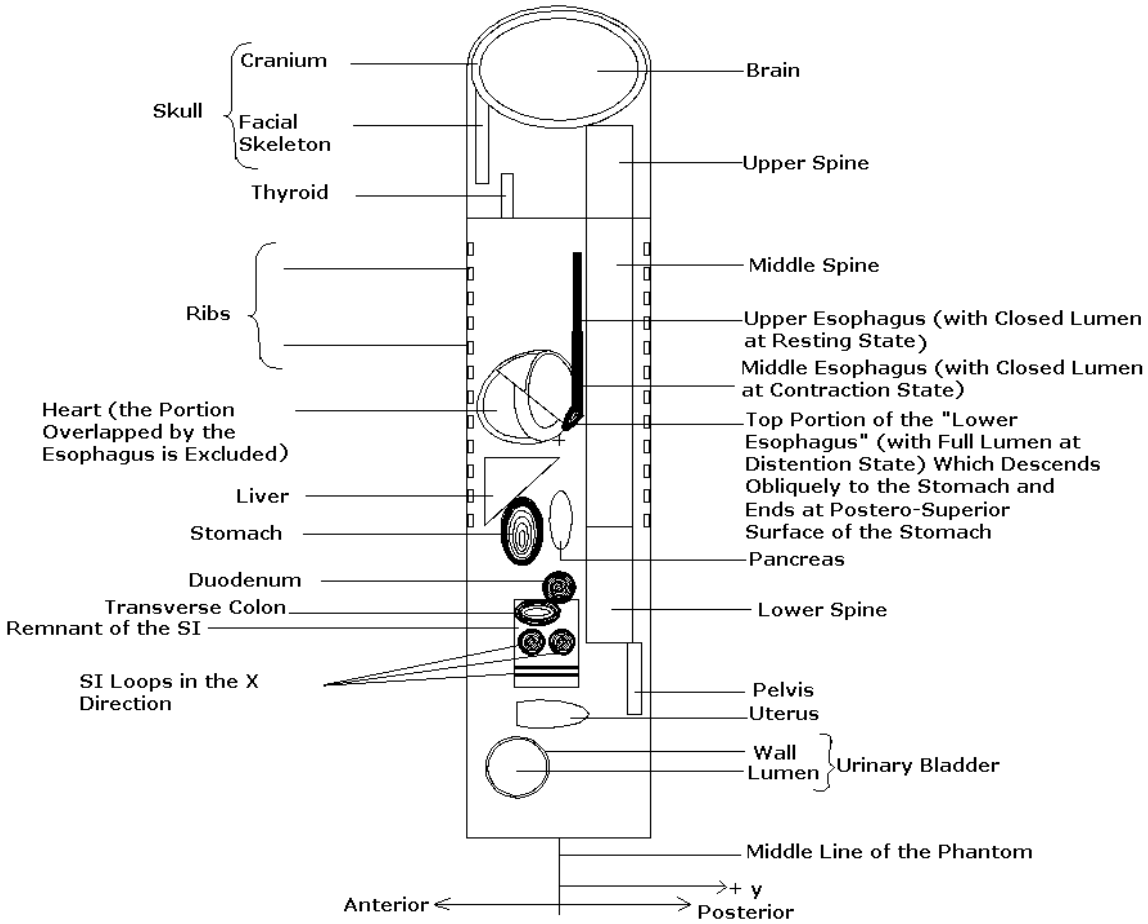


**Fig. 2.** Lateral view of the phantom sectioned along the sagittal plane x = 0.

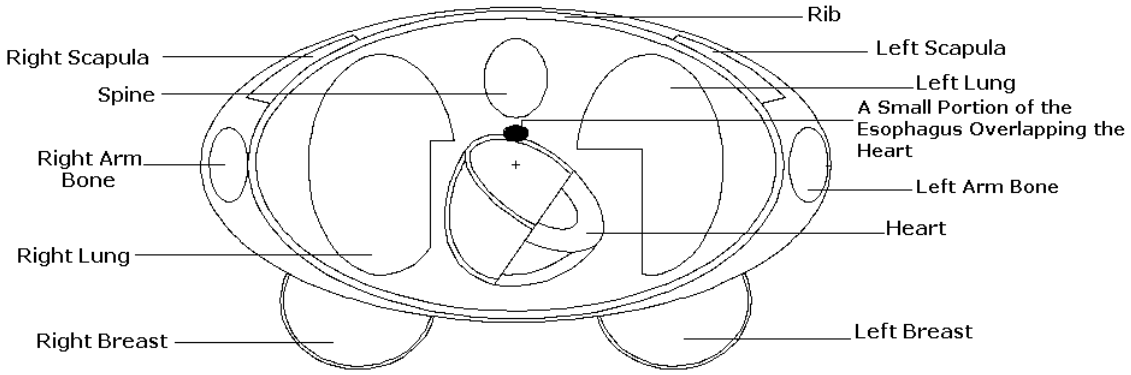


**Fig. 3.** Major organs/regions in the upper trunk region, sectioned along the transverse plane z = 52 cm, of the phantom representing adult male and larger-than-average adult female.

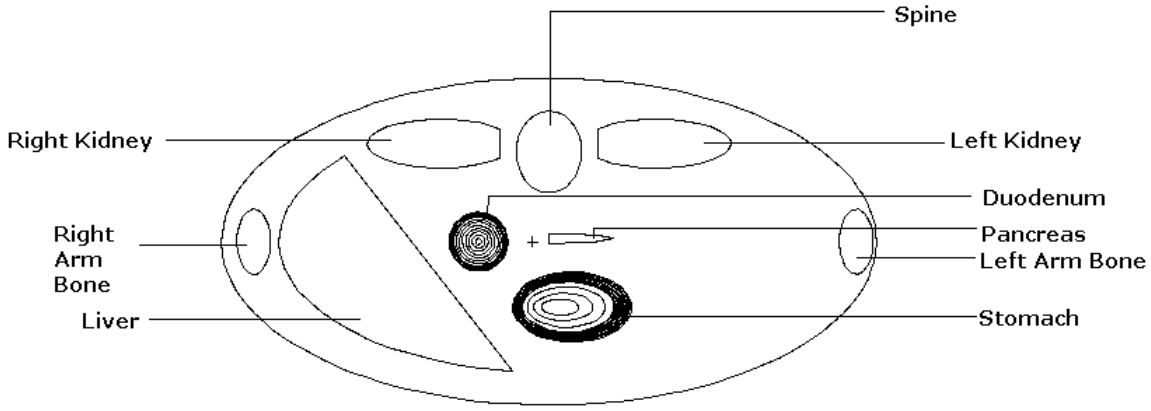


**Fig. 4.** Major organs/regions in the middle trunk sectioned along the transverse plane z = 32.7 cm.

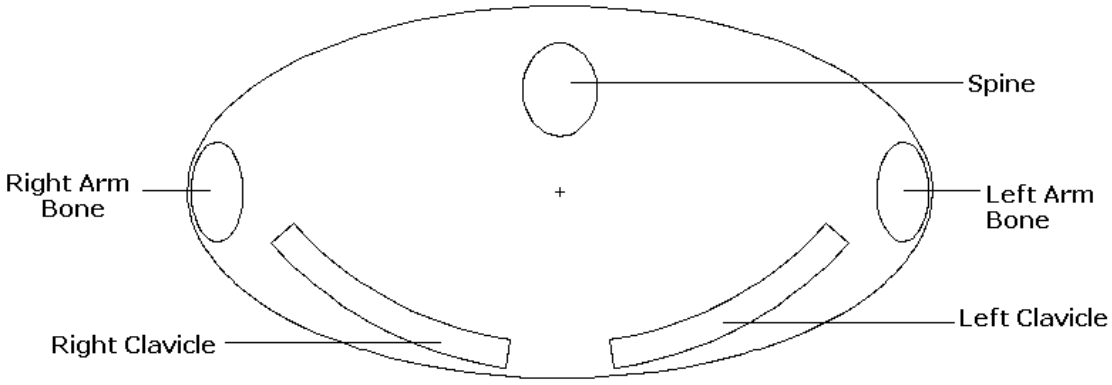


**Fig. 5.** Transverse view of the upper trunk region of the adult phantom.

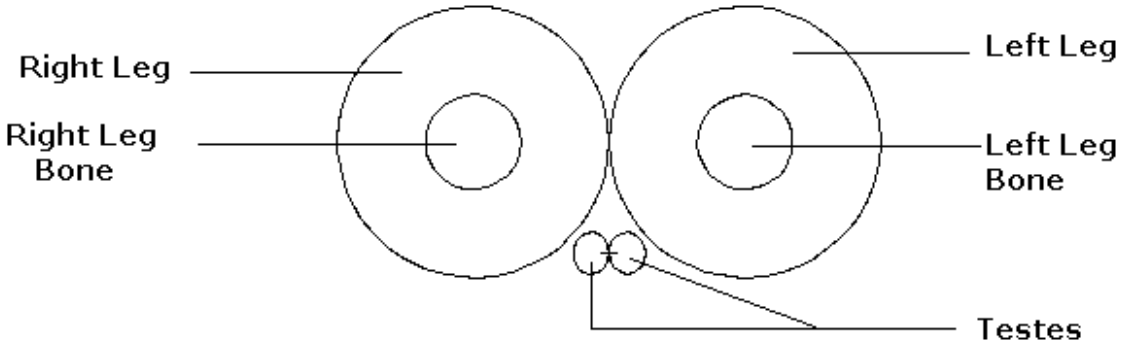


**Fig. 6.** Transverse view of the phantom sectioned along the transverse plane z = -2.3 cm with the testes identified at (± 1.3 cm, -8 cm, -2.3 cm).

The SI consists of four regions. These regions are different in shape and size and represent the duodenum, jejunum, and ileum with full lumens, and the remnant of the jejuno-ileum region with an empty lumen. The wall of the SI with empty lumen cannot withstand external pressure and as a result the wall collapses closing the lumen. The "remnant" is modeled as a solid region without lumen and represents that part of the SI where the lumen is empty and closed. Thus, in the dosimetric calculations, it is assumed there is no source in the remnant. In contrast, radiation sources are assumed to be homogenously distributed in the contents of the other three subsections. The folds are considered to be only in the jejuno-ileum region with full lumen. The folds are not considered in the remnant as the "cross-dose" to the remnant without folds is not considerably different from the dose with the folds. The folds are delineated by repeating the basic structures of jejunum and ileum in the x-, y- and z-directions. The jejuno-ileum region, bounded by the ULI and the LLI, occupies the same space defined by Snyder et al. (1974) and later adopted by Cristy and Eckerman (1987) for their phantoms. The parameters for each subsection were based on anatomic data.

The ULI consists of the ascending colon (AC) and transverse colon (TC) while the LLI consists of the descending colon (DC) and recto-sigmoid colon (RSC). As indicated previously, Cristy and Eckerman (1987) considered only the organ masses in their model. They ignored the other structural parameters such as length, wall thickness, and lumen diameter. The lumens were full in their model. The masses of the contents were different from the real masses. The Monte Carlo simulation results were not corrected for these deviations. In the new model, all colon lumens, except the lumen of

the RSC, are partly filled and partly empty. The RSC lumen is entirely filled in the new model. Except for the length, the other structural parameters and the masses of the wall and the contents are based on the anatomic data available in the literature. Though the lengths used in the Cristy and Eckerman colon models (1987) are smaller than the real anatomic lengths, the same lengths are used in the revised model to fit the colon in the correct anatomic space. Appropriate factors are applied to the simulation results to correct for deviations in the length as well as in the other parameters. Transit times are taken into account in the calculations.

The parameters describing the sections of the GIT in the current model, along with specific drawings, are presented in Appendix I. Data are included from various other references and models, e.g., ICRP Reference Man (1975), the MIRD model (Snyder et al. 1978), the ICRP model (1979), the Cristy and Eckerman model (1987), the Poston et al. model (1996a, 1996b), the Stubbs et al. model (1998), the Bhuiyan model (2000), the Jönsson et al. model (2001), and the ICRP Human Alimentary Tract (HAT) document (2001). The HAT document, prepared for the newest ICRP GIT model, is expected to be published in the year 2004. The model values were based on data obtained from review of various books, references and journal articles.

The phantom developed in the research was coupled with the MCNP4C Monte Carlo simulation package (Briesmeister 2000). The code was used for calculating specific absorbed fractions (SAFs) in various organs and radiosensitive tissues from fifteen uniformly distributed sources of monoenergetic photons and electrons, ranging from 10 keV to 4 MeV, in the lumen contents of the five GIT sections.

A detailed description of the new GIT model, including a discussion of the elemental composition of the regions, is presented in Appendix I. In addition, the heart and the pancreas are described but the other organs are not described as they are identical to those of the Cristy-Eckerman adult phantom (1987).

## MONTE CARLO RADIATION TRANSPORT

The absorbed dose due to internally deposited radionuclides is usually evaluated by Monte Carlo simulation because the complex nature of radiation transport and the complexity of the exposure geometry (e.g., the human body), make analytical solution intractable. The use of Monte Carlo methods in solving dosimetric problems has dramatically increased in recent years due to a rapid increase in speed and a decrease in cost of data processing, as well as the availability of large, general-purpose software packages. MCNP is such a general-purpose Monte Carlo N-Particle code package that can be used for neutron, photon, electron, or coupled neutron/photon/electron transport (Briesmeister 2000).

The most important condition for an accurate Monte Carlo simulation is that one takes into account accurately all the relevant physical processes. As radiation passes through matter, it undergoes various physical processes depending on the type of radiation (photon, neutron, or electron/positron), energy, and on the interacting medium. The fundamental quantities describing the properties of the medium for photon and electron interactions are atomic number or "effective atomic number" ($Z_{eff}$) for compound media, electron concentration per unit mass, which can be represented

basically by the ratio of effective atomic number to effective mass number ($(Z/A)_{eff}$), and mass-density. A multiplication of the Avogadro constant with $(Z/A)_{eff}$ gives electron concentration per unit mass that increases with increasing the contents of low-Z elements, in particular hydrogen, in the compound. Rogers and Bielajew (1990) reviewed how the interaction cross sections vary with energy and properties of matter to show which processes are relevant in a given simulation. This review briefly describes almost all possible interaction processes of photons and electrons. Details of these interaction mechanisms can be obtained from the standard reference works of Heitler (1954) and Evans (1955).

A Monte Carlo simulation code has four major components: (1) the cross-section data for all the processes being considered in the simulation, (2) the algorithms that account for the processes and govern the particle transport, (3) the methods used to specify the geometry of the problem and to determine the physical quantities of interest, and (4) the analysis of the information obtained during the simulation.

The first two components affect the underlying physics of the simulation, while the last two of these components can greatly affect the running time without affecting the physics. The physics of radiation interactions is the very essence of a Monte Carlo code. Two Monte Carlo codes may be different simply because the physics treatments in the codes are different.

MCNP has two photon interaction models: simple and detailed. The simple model considers the photoelectric effect without fluorescence and Auger electrons, considers Compton (incoherent) scattering from free electrons without the use of form

factors, which accounts for electron binding effects, and considers pair production. The highly forward-peaked coherent scattering is ignored.

In contrast, the detailed model considers both coherent and incoherent scattering with the use of form factors, pair production, and accounts for fluorescent photons and Auger electron after photoelectric absorption. But both the models ignore several other photon interactions, such as nuclear Thomson scattering, Delbrück scattering, triplet production and high-energy photonuclear interaction because these are rare events and rarely important in radiation dosimetry calculations.

This research used the detailed physics treatment for the present MCNP calculations. In the detailed model, the MCNP code uses modified Klein-Nishina differential cross sections (Briesmeister 2000) to determine the angle and energy of the Compton-scattered photon and the recoil kinetic energy of the electron. The modification is made to take into account the form factor. For sampling of the differential cross section for coherent scattering, MCNP uses Thomson differential cross sections (Attix 1986) with some modification to take into account the combined scattering action of the whole atom and the binding effect of electron in the atom, and to reduce the Thomson cross section more extremely for backward scattering for high-energy and low-Z materials. The MCNP code includes the fluorescent X-rays or Auger electrons, resulting from the photoelectric effect, in three ways: fluorescent X-rays or Auger electrons or both types can be emitted but, (1) no fluorescence photon is emitted with energy greater than cutoff energy; (2) one fluorescent photon with energy greater than the cutoff energy is emitted; (3) two fluorescent photons with energy exceeding the

cutoff energy can occur. MCNP considers all shells in the relaxation process. MCNP handles all photon-induced charged particles (electrons and positrons) in three distinct ways, which are the same for both the simple and detailed photon physics treatment. The kinetic energy of the photon-induced charged particle can be deposited locally irrespective of its energy, can be transported, or (default) can be treated with the thick-target bremsstrahlung (TTB) approximation. The charged particles are transported in the calculations described here.

## RESULTS AND DISCUSSION

This section presents the results obtained from benchmark calculations and from the calculations using the revised gastrointestinal tract (GIT) model developed in this research. It also provides a discussion of the results of each task.

### BENCHMARK CALCULATION

The Cristy and Eckerman adult male phantom (1987), which was a modified version of the revised MIRD phantom (Snyder et al. 1978), was coded into the MCNP 4C Monte Carlo simulation package (Briesmeister 2000) for calculation of "specific absorbed fraction" (SAF) values in various organs (target organs) of the body from sources of the same 12 monoenergetic photons, 10 keV-4 MeV, distributed uniformly in the stomach (ST) contents. The SAF for a given source-target pair was defined as the fraction of the source energy absorbed per unit mass of the target organ. The SAF values obtained from the calculations were compared to the "best" estimates of Cristy and Eckerman (1987) with the ST as source organ to verify and benchmark the initial design

and coding of the phantom and the Monte Carlo treatment to be employed in this research.

Cristy and Eckerman (1987) described the procedures used in choosing the "best" estimate of SAF from the estimates generated by three methods—direct Monte Carlo method, converse Monte Carlo method based on the reciprocal dose principle (Loevinger 1969), and the point-source kernel method (Berger 1968; Brownell et al. 1968) — for a given source-target pair. They used the ALGAM Monte Carlo computational package (Warner and Craig 1968), which lacked electron transport capability. So the photon-induced electrons (or secondary electrons) were not transported in their Monte Carlo calculations, i.e., the electron energy was assumed to be deposited at the site of the photon interaction.

In this benchmark calculation, two sets of Monte Carlo calculations — with and without transporting the secondary electrons — were performed. The SAF values obtained from these calculations are presented in Table 1 for various target organs with the source in the stomach contents. Each cell in Table 1 contains two values. The upper and lower values were obtained with and without electron transport, respectively. The SAFs without electron transport were used for benchmark comparisons presented in Figs. 7(a-c).

Table 1 shows that the SAFs with and without electron transport are almost the same, as demonstrated by Poston et al. (1996b). The small difference between the two values may be attributed to statistical fluctuations in the Monte Carlo calculation. Figs. 7(a-c) shows that the SAF values for all organs, except for the whole body, obtained

from benchmark calculations closely agree with those of Cristy and Eckerman (1987). The differences between these two calculations are relatively large at 10 and 15 keV for those organs located at relatively large distances from the stomach. This is due to the greater difference in the interaction cross-section data and in algorithms used in the ALGAM and MCNP 4C, and higher statistical fluctuations for lower energy photons.

As demonstrated in Fig 7(c), the SAF values for whole body obtained in the benchmark calculation are significantly larger than those provided by Cristy and Eckerman (1987) for photon energies ≤ 30 keV. The best estimates of SAF values made by Cristy and Eckerman (1987) are $6.8\times10^{-4}$ $kg^{-1}$ at 10 keV, $2.3\times10^{-3}$ $kg^{-1}$ at 15 keV, $4.5\times10^{-3}$ $kg^{-1}$ at 20 keV, and $7.5\times10^{-3}$ $kg^{-1}$ at 30 keV for whole body with a mass of 73.7 kg without female breasts. The SAFs for the whole body were expected to be $1.35\times10^{-2}$ $kg^{-1}$ (≈ 1/73.7 kg) at energies ≤ 20 keV because the photons with these energies would deposit almost all their energy within the body if they had to traverse several mean free paths (= $1/\mu_{en}$) to escape the body. In the benchmark calculations, the SAF values obtained were $1.36\times10^{-2}$ $kg^{-1}$, $1.36\times10^{-2}$ $kg^{-1}$, $1.35\times10^{-2}$ $kg^{-1}$, and $1.24\times10^{-2}$ $kg^{-1}$ (see Table 1) as theoretically expected. Obviously, the Cristy and Eckerman (1987) SAFs for the whole body (≤ 30 keV) were incorrect at the low energies. For 50 keV and above, percent differences between the two SAFs were in the range of 15-20%. In the benchmark calculations, the SAFs obtained were essentially zero at low energies for small organs located at large distances from the stomach (the source organ) (see

Table 1. Specific absorbed fraction (SAF) of photon in $kg^{-1}$ for adult male or larger-than-average-adult female developed by Cristy and Eckerman (1987) when source is stomach contents.[a]

| Target | Energy (MeV) | | | | | | | | | | | |
|---|---|---|---|---|---|---|---|---|---|---|---|---|
| | 0.010 | 0.015 | 0.020 | 0.030 | 0.050 | 0.100 | 0.200 | 0.500 | 1.000 | 1.500 | 2.000 | 4.000 |
| Brain | 0.0 | 0.0 | 0.0 | 0.0 | 3.39E-6 | 1.59E-5 | 2.75E-5 | 6.07E-5 | 1.05E-4 | 1.38E-4 | 1.77E-4 | 1.96E-4 |
| | 0.0 | 0.0 | 0.0 | 0.0 | 3.31E-6 | 1.61E-5 | 2.84E-5 | 6.12E-5 | 1.02E-4 | 1.32E-4 | 1.56E-4 | 1.90E-4 |
| LLI Wall | 0.0 | 3.18E-6 | 2.19E-4 | 2.27E-3 | 4.69E-3 | 4.43E-3 | 4.16E-3 | 4.05E-3 | 3.82E-3 | 3.76E-3 | 3.79E-3 | 2.99E-3 |
| | 0.0 | 3.75E-6 | 2.22E-4 | 2.25E-3 | 4.68E-3 | 4.50E-3 | 4.17E-3 | 4.09E-3 | 3.95E-3 | 3.76E-3 | 3.61E-3 | 3.11E-3 |
| SI Wall | 3.68E-6 | 2.03E-4 | 1.17E-3 | 6.19E-3 | 1.14E-2 | 1.03E-2 | 9.26E-3 | 8.66E-3 | 8.08E-3 | 7.59E-3 | 7.17E-3 | 5.91E-3 |
| | 3.78E-6 | 2.01E-4 | 1.17E-3 | 6.09E-3 | 1.14E-2 | 1.04E-2 | 9.27E-3 | 8.63E-3 | 8.01E-3 | 7.49E-3 | 7.07E-3 | 5.94E-3 |
| Stomach | 2.99E-1 | 7.02E-1 | 8.47E-1 | 6.51E-1 | 3.20E-1 | 1.87E-1 | 1.81E-1 | 1.80E-1 | 1.66E-1 | 1.49E-1 | 1.38E-1 | 1.06E-1 |
| Wall | 2.99E-1 | 7.01E-1 | 8.44E-1 | 6.43E-1 | 3.20E-1 | 1.88E-1 | 1.81E-1 | 1.80E-1 | 1.65E-1 | 1.50E-1 | 1.39E-1 | 1.11E-1 |
| ULI Wall | 5.57E-6 | 9.94E-4 | 5.41E-3 | 1.49E-2 | 1.76E-2 | 1.37E-2 | 1.21E-2 | 1.17E-2 | 1.01E-2 | 9.62E-3 | 8.54E-3 | 8.35E-3 |
| | 5.31E-6 | 9.83E-4 | 5.38E-3 | 1.48E-2 | 1.75E-2 | 1.36E-2 | 1.21E-2 | 1.13E-2 | 1.05E-2 | 9.70E-3 | 9.10E-3 | 7.57E-3 |
| Kidneys | 0.0 | 8.02E-7 | 4.03E-4 | 7.62E-3 | 1.58E-2 | 1.40E-2 | 1.25E-2 | 1.16E-2 | 1.06E-2 | 9.89E-3 | 9.26E-3 | 7.83E-3 |
| | 0.0 | 6.08E-7 | 3.91E-4 | 7.47E-3 | 1.58E-2 | 1.41E-2 | 1.25E-2 | 1.16E-2 | 1.08E-2 | 1.00E-2 | 9.42E-3 | 7.88E-3 |
| Liver | 0.0 | 9.87E-6 | 3.59E-4 | 3.57E-3 | 7.68E-3 | 7.45E-3 | 6.81E-3 | 6.57E-3 | 6.26E-3 | 5.87E-3 | 5.54E-3 | 4.75E-3 |
| | 0.0 | 9.92E-6 | 3.58E-4 | 3.52E-3 | 7.71E-3 | 7.52E-3 | 6.86E-3 | 6.57E-3 | 6.22E-3 | 5.87E-3 | 5.58E-3 | 4.74E-3 |
| Lungs | 1.80E-7 | 1.34E-4 | 1.20E-3 | 4.89E-3 | 6.98E-3 | 5.83E-3 | 5.27E-3 | 5.14E-3 | 4.85E-3 | 4.60E-3 | 4.48E-3 | 3.70E-3 |
| | 2.02E-7 | 1.35E-4 | 1.19E-3 | 4.83E-3 | 6.98E-3 | 5.87E-3 | 5.30E-3 | 5.12E-3 | 4.84E-3 | 4.54E-3 | 4.29E-3 | 3.62E-3 |
| Ovaries | 0.0 | 0.0 | 0.0 | 2.77E-4 | 1.75E-3 | 3.00E-3 | 2.72E-3 | 2.82E-3 | 2.94E-3 | 2.69E-3 | 2.85E-3 | 4.45E-3[b] |
| | 0.0 | 0.0 | 0.0 | 2.68E-4 | 1.85E-3 | 2.76E-3 | 2.81E-3 | 2.88E-3 | 2.88E-3 | 2.85E-3 | 2.63E-3 | 2.40E-3 |
| Pancreas | 5.90E-5 | 9.26E-3 | 5.10E-2 | 1.15E-1 | 9.80E-2 | 6.36E-2 | 5.57E-2 | 5.19E-2 | 4.64E-2 | 4.33E-2 | 3.98E-2 | 3.16E-2 |
| | 6.01E-5 | 9.28E-3 | 5.06E-2 | 1.13E-1 | 9.81E-2 | 6.41E-2 | 5.59E-2 | 5.17E-2 | 4.67E-2 | 4.26E-2 | 3.95E-2 | 3.20E-2 |
| Skeleton | 3.87E-8 | 5.29E-5 | 5.84E-4 | 2.88E-3 | 5.25E-3 | 3.87E-3 | 2.53E-3 | 2.00E-3 | 1.85E-3 | 1.76E-3 | 1.75E-3 | 1.51E-3 |
| | 3.69E-8 | 5.24E-5 | 5.82E-4 | 2.86E-3 | 5.22E-3 | 3.86E-3 | 2.53E-3 | 1.99E-3 | 1.85E-3 | 1.77E-3 | 1.70E-3 | 1.51E-3 |
| Testes | 0.0 | 0.0 | 0.0 | 6.92E-6 | 2.63E-5 | 1.19E-4 | 2.51E-4 | 2.79E-4 | 5.87E-4[c] | 4.23E-4 | 4.40E-4 | 1.50E-3[b] |
| | 0.0 | 0.0 | 0.0 | 6.80E-6 | 2.79E-5 | 1.04E-4 | 1.54E-4 | 3.11E-4 | 3.89E-4 | 4.44E-4 | 4.66E-4 | 5.06E-4 |
| Urinary | 0.0 | 0.0 | 0.0 | 3.24E-5 | 4.17E-4 | 9.16E-4 | 1.02E-3 | 1.32E-3 | 1.10E-3 | 1.48E-3 | 1.20E-3 | 1.97E-3[b] |
| Blad Wall | 0.0 | 0.0 | 0.0 | 2.82E-5 | 4.19E-4 | 8.76E-4 | 9.93E-4 | 1.17E-3 | 1.29E-3 | 1.34E-3 | 1.33E-3 | 1.27E-3 |
| Uterus | 0.0 | 0.0 | 0.0 | 1.99E-4 | 1.64E-3 | 2.58E-3 | 2.60E-3 | 2.71E-3 | 2.65E-3 | 2.57E-3 | 2.55E-3 | 2.32E-4[b] |
| | 0.0 | 0.0 | 0.0 | 1.93E-4 | 1.64E-3 | 2.54E-3 | 2.58E-3 | 2.64E-3 | 2.65E-3 | 2.60E-3 | 2.53E-3 | 2.24E-3 |
| Whole | 1.36E-2 | 1.36E-2 | 1.35E-2 | 1.24E-2 | 9.37E-3 | 6.67E-3 | 6.13E-3 | 5.98E-3 | 5.59E-3 | 5.19E-3 | 4.85E-3 | 3.96E-3 |
| Body | 1.36E-2 | 1.36E-2 | 1.35E-2 | 1.24E-2 | 9.36E-3 | 6.68E-3 | 6.13E-3 | 6.00E-3 | 5.59E-3 | 5.18E-3 | 4.85E-3 | 3.97E-3 |

[a] Each cell contains two values—upper and lower, where the upper and lower are obtained from Monte Carlo calculations with and without electron transport, respectively. [b] Relative errors are 0.32 for ovaries, 0.57 for testes, 0.18 for urinary bladder wall, and 0.13 for uterus at 4 MeV. [c] Relative error is 0.40.

Table 1). The SAFs with zero values are not shown in Fig. 7(c) as zero cannot be plotted on a log chart.

The SAFs provided by Cristy and Eckerman (1987) do not follow a smooth variation with photon energy. The SAFs obtained in this benchmark calculation vary smoothly with photon energy.

The relative errors associated with the Monte Carlo calculations in the benchmark calculations were below 0.1, but most of them were less than 0.05. These errors are not shown in the figures as they were indiscernible from the data points. The relative errors in the calculations with electron transport were relatively high because of the energy straggling. In some cases, the errors exceeded 0.1, shown in Table 1, for the organs with small masses (e.g., ovaries, testes) located at relatively large distances from the source.

In conclusion, the SAF values for all organs, except for the whole body, obtained in the benchmark calculations were in good agreement with those provided by the Cristy and Eckerman (1987). The SAFs for the whole body in the benchmark calculations were obtained as expected. So the design and the coding of the phantom and Monte Carlo treatment to be employed in this study were considered valid.

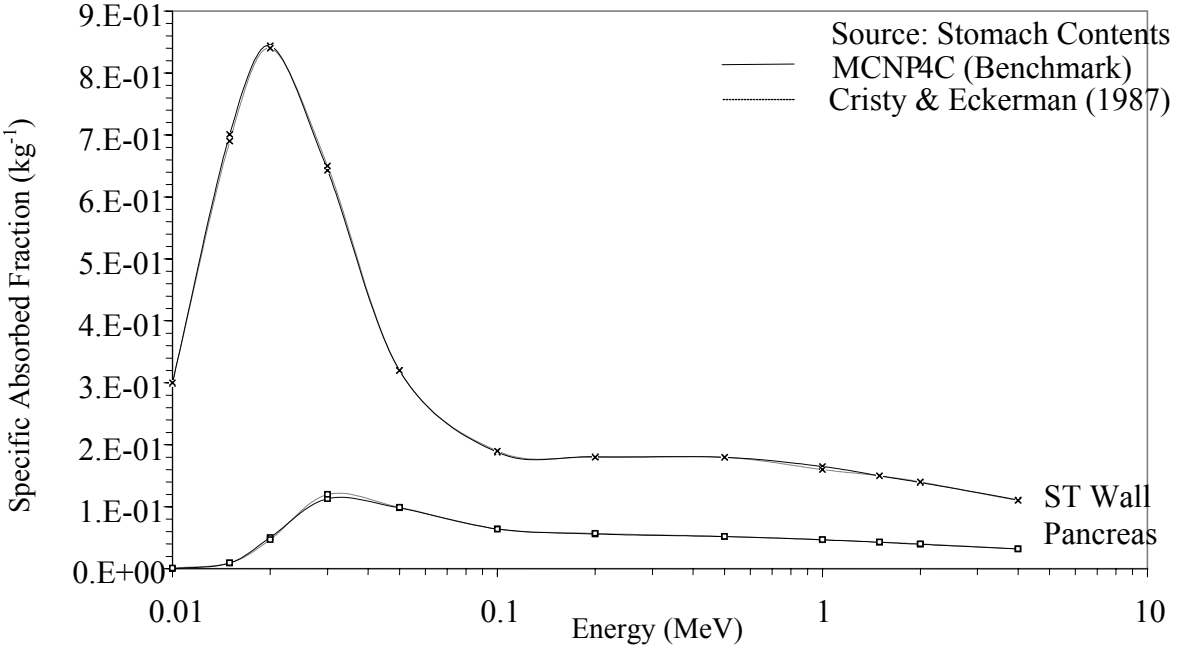
Source: Stomach Contents
MCNP4C (Benchmark)
Cristy & Eckerman (1987)
ST Wall
Pancreas
Specific Absorbed Fraction (kg-1)
Energy (MeV)
9.E-01
8.E-01
7.E-01
6.E-01
5.E-01
4.E-01
3.E-01
2.E-01
1.E-01
0.E+00
0.01
0.1
1
10

Fig. 7(a)

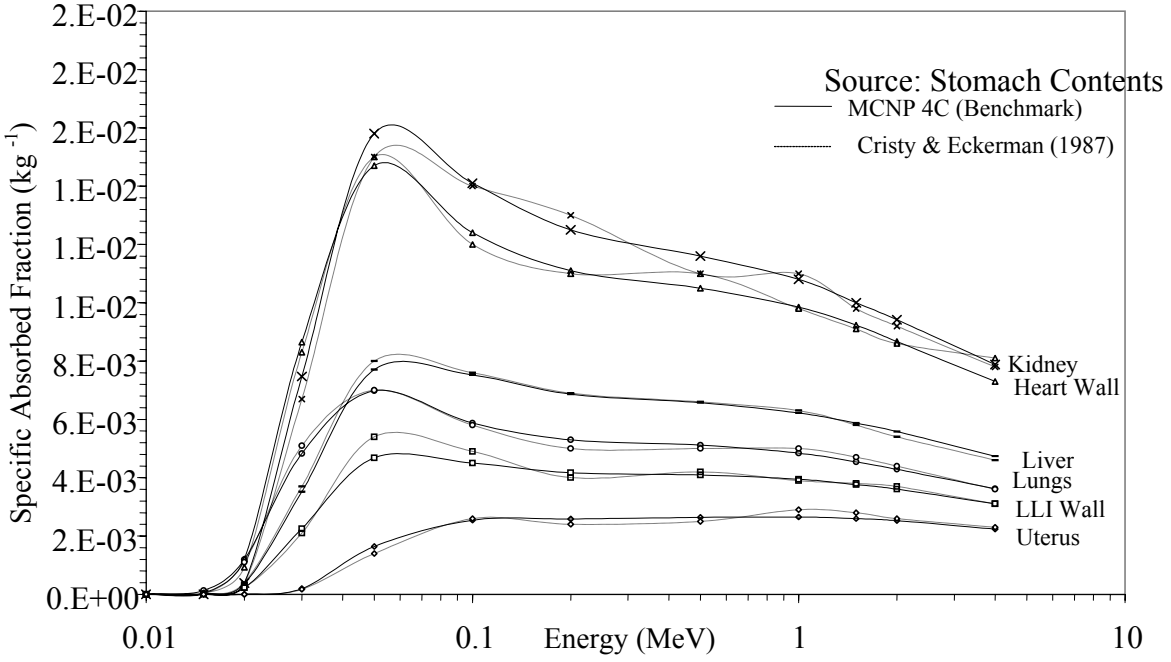
Source: Stomach Contents
MCNP 4C (Benchmark)
Cristy & Eckerman (1987)
Kidney
Heart Wall
Liver
Lungs
LLI Wall
Uterus
Specific Absorbed Fraction (kg -1)
Energy (MeV)
2.E-02
2.E-02
2.E-02
1.E-02
1.E-02
1.E-02
8.E-03
6.E-03
4.E-03
2.E-03
0.E+00
0.01
0.1
1
10

Fig. 7(b)

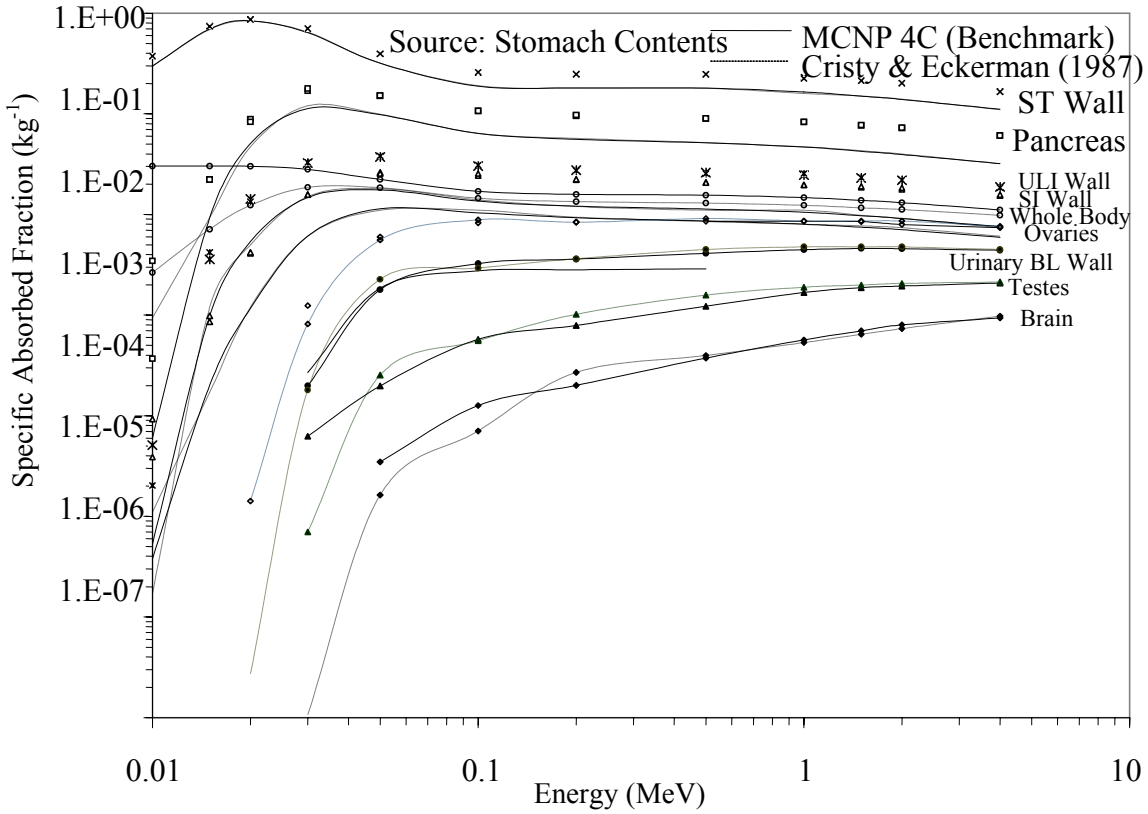


Fig. 7(c)

**Figs. 7(a-c).** Benchmark comparisons of specific absorbed fractions obtained with MCNP 4C in this study to the "best" estimates of Cristy and Eckerman (1987) in various organs of the body from sources of 12 monoenergetic photons, 10keV-4MeV in the stomach contents for an adult male (73.7 kg Reference Man) modeled by Cristy and Eckerman (1987).

## REVISED MODEL

Specific absorbed fractions (SAFs) in various organs and tissues from 15 uniformly distributed monoenergetic electron and photon sources, in the energy range 10

keV-4 MeV, in the lumenal contents (source contents) of the five sections of the GIT of an adult human male or a larger-than-average-female (72.63 kg) were calculated. These These five sections of the GIT were the esophagus (ESP), stomach (ST), small intestine (SI), upper large intestine (ULI), and the lower large intestine (LLI). The SAFs were calculated for 19 targets, including the walls of the five sections of the GIT, for each of the five source contents. Except for walls of the GIT, average SAFs were calculated. For the GIT, the SAFs were calculated as a function of distance or depth in the wall of the sections of the GIT. The distance in the wall was measured from wall-contents interface. Complete results are presented in Tables II-1 and II-2 in Appendix II. For an efficient discussion, only a few of the results are presented here in Figs. 8 and 19. The following relationship can be used to convert the tabulated SAFs (in $kg^{-1}$) into the absorbed dose in Gy per source particle with energy E in MeV: $SAF \times E \times 1.602 \times 10^{-13}$.

The SAFs for all organs except the SI, ULI, and LLI, were obtained from the direct results of the Monte Carlo simulations performed using MCNP4C. The simulation results for the SI, ULI, and the LLI needed to be adjusted due to the differences between the model and the actual anatomic data.

The relative errors associated with the Monte Carlo calculations were below 0.1, but most of them were less than 0.05. These errors were not shown in the figures as they were indiscernible from the data points. The relative errors in the calculations with electron transport were relatively high because of the stochastic energy loss-rate of the electrons. This fluctuation of energy loss-rate is commonly termed as the energy or range straggling. The errors were the highest at the maximum penetration depth or range

of the electrons. The errors also were high for organs with small masses (e.g., ovaries, testes) located at relatively large distances from the sources (e.g., esophagus, stomach). In some cases, these errors exceeded 0.1, shown in Tables II-1 and II-2.

Figs. 8(a) - 8(h) show SAFs in some organs and tissues with a high risk of radiation-induced cancer as a function of energy of the source particles in the five sections of the GIT. These SAF curves have some general characteristics discussed below.

For a given source-target pair, the photon SAF rises sharply with increasing energy and reaches a maximum at around 50 keV. This is because of the strong energy dependence of mass energy-absorption coefficient ($\mu_{en}/\rho$) below 50 keV. As the $\mu_{en}/\rho$ decreases rapidly with the increase of photon energy, the attenuation by the intervening medium between the source and the target drops sharply; conversely, a sharp rise in the energy fluence in the target region occurs. Above 60 keV, the energy fluence becomes almost constant for most of the source-target pairs because the distance between each of these source-target pairs is less than the mean free-path of a 60-keV photon which is 30 cm in water. It is noted that the $\mu_{en}/\rho$ in the human body, except in the skeletal system, is similar to that of water. The $\mu_{en}/\rho$ also is almost constant over the energy range 60 keV - 4 MeV in all organs but the skeletal system for which the $\mu_{en}/\rho$ is almost constant between 150 keV – 4 MeV. A constant $\mu_{en}/\rho$ and a constant energy fluence essentially give a constant SAF, as demonstrated in Figs. 8(a) through 8(g), over the energy range 60 keV – 4 MeV, for all the target organs but the skeleton for which the SAF curve is almost flat between 150 keV and 4 MeV.

The flat regions in the SAF-energy curves in these figures have small negative or positive slopes. The small negative slopes are due to the slow decrease in the $\mu_{en}/\rho$ with increasing energy. If targets are located from a source at distances greater than the mean free path of the relevant source photon, the curves have small positive slopes, i.e., the SAF slowly increases with increasing energy. This is because of the combined effects of the increase in the fluence at the target regions and the slow decrease in the $\mu_{en}/\rho$ with increasing photon energy.

For example, at least one of the three bones — the middle spine, ribs and the pelvis — containing the highest percentages of the active marrow in the body is located within the 30 cm of any of the five sections of the GIT. About 70% of the active marrow is located in these three bones. As shown in Fig. 8(a), the photon SAF curves for the active marrow follow the pattern having negative slope for all five sections of the GIT as source organs. A similar pattern is observed for the liver as a target when the sources are the GIT sections except the LLI (Fig. 8(e)). The curve for the LLI as a source follows the pattern with a positive slope.

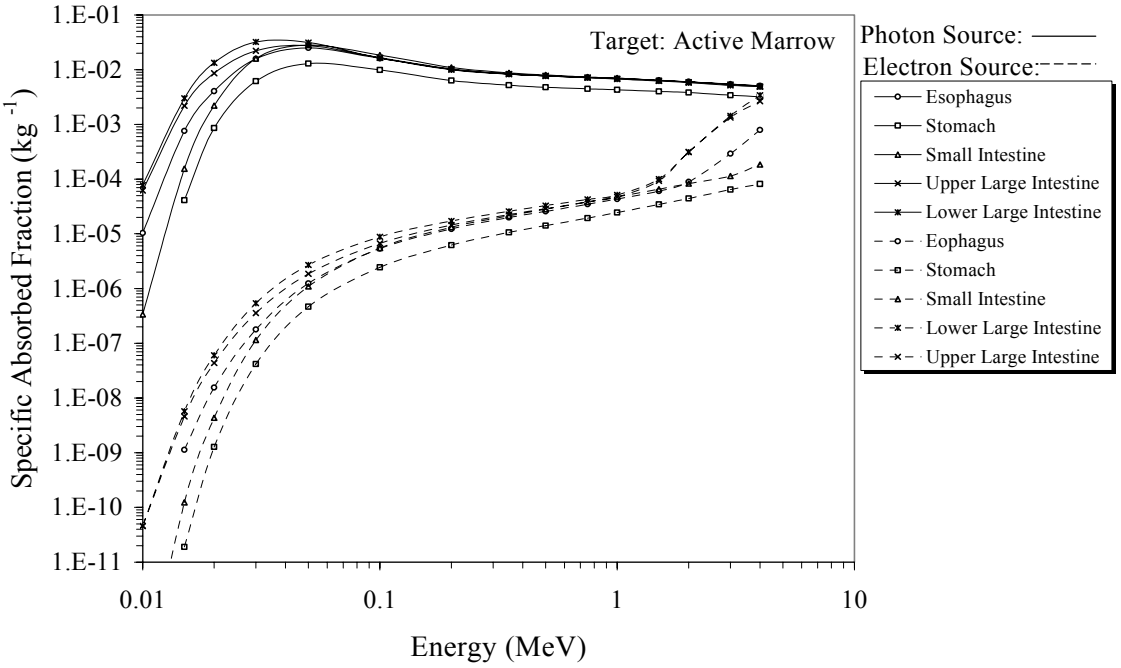


Figure 8(a)

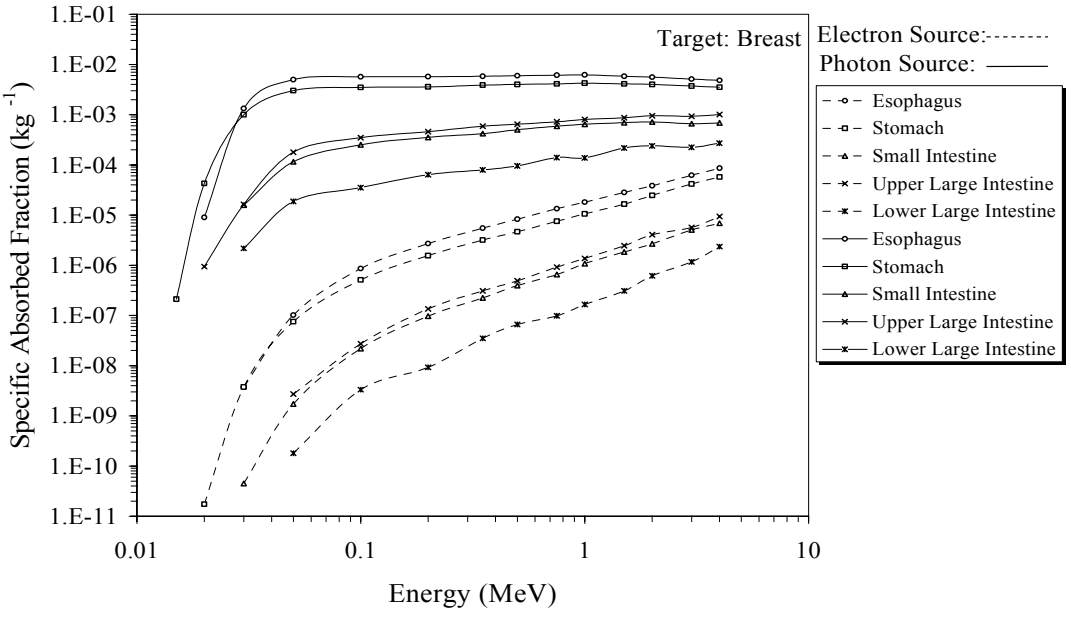


Figure 8(b)

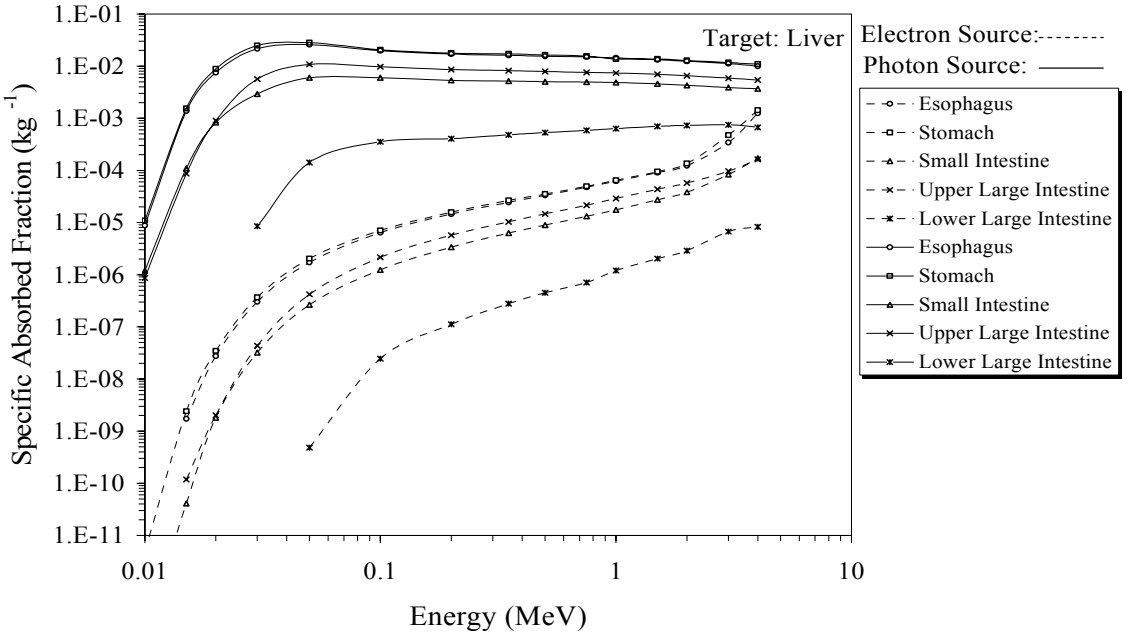


Figure 8(c)

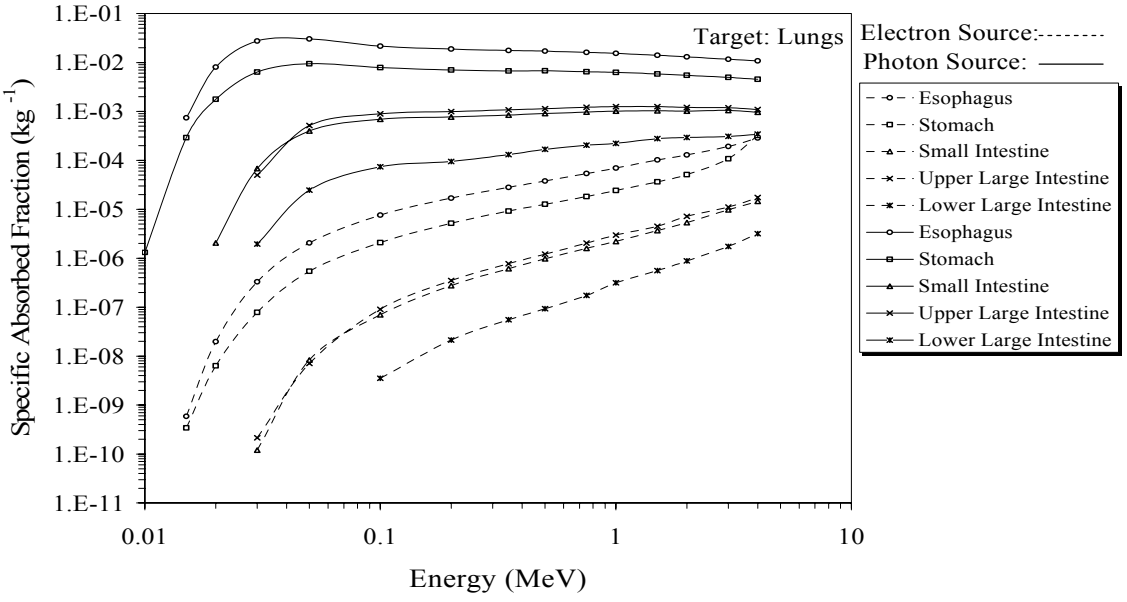


Figure 8(d)

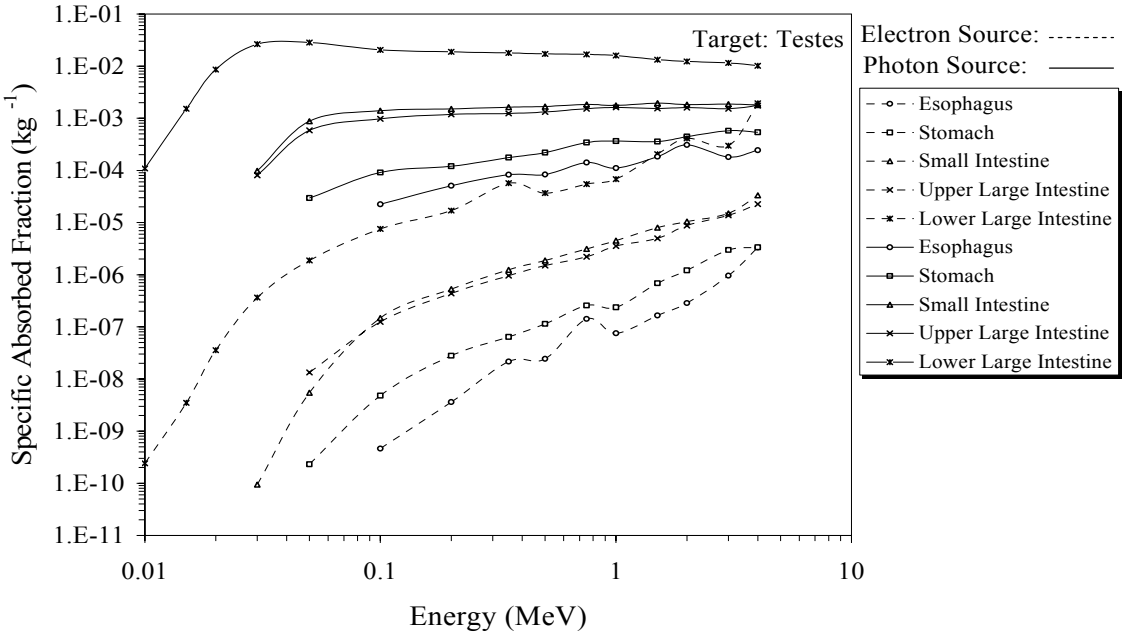


Figure 8 (e)

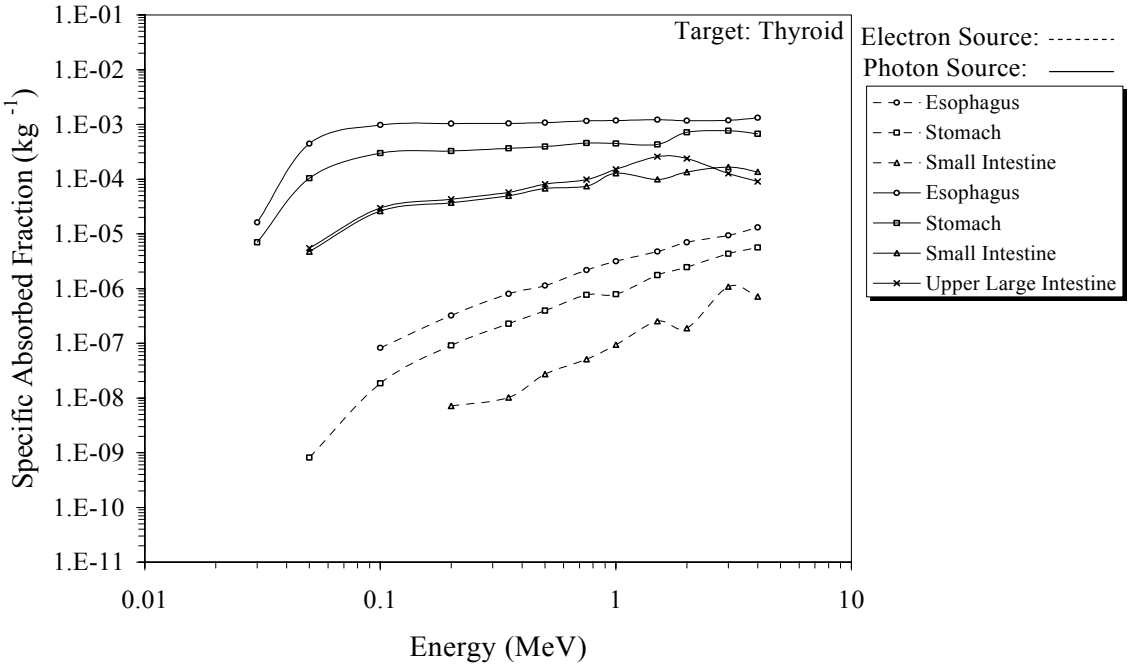


Figure 8(f)

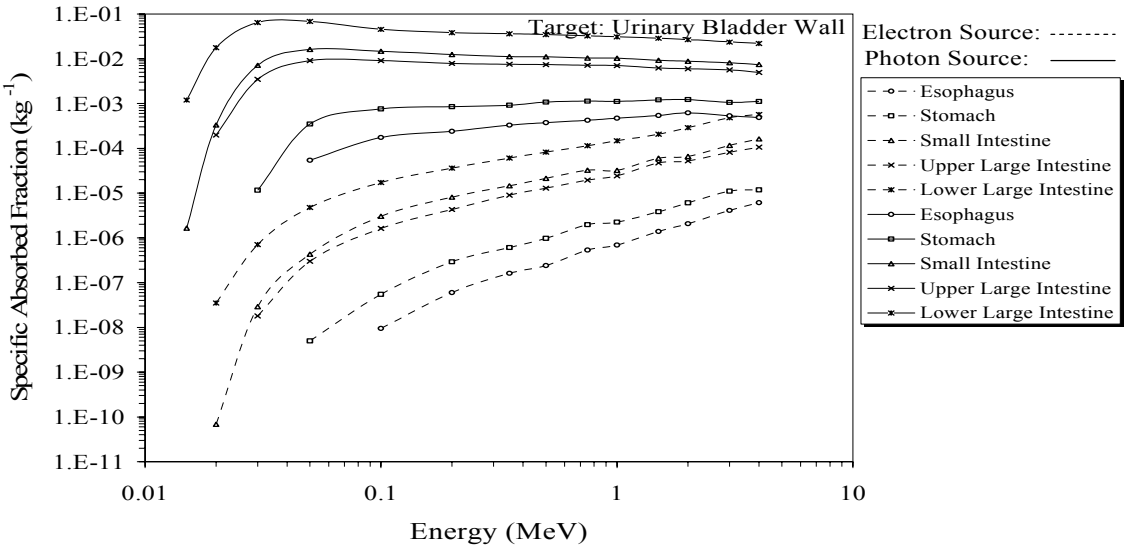


Figure 8(g)

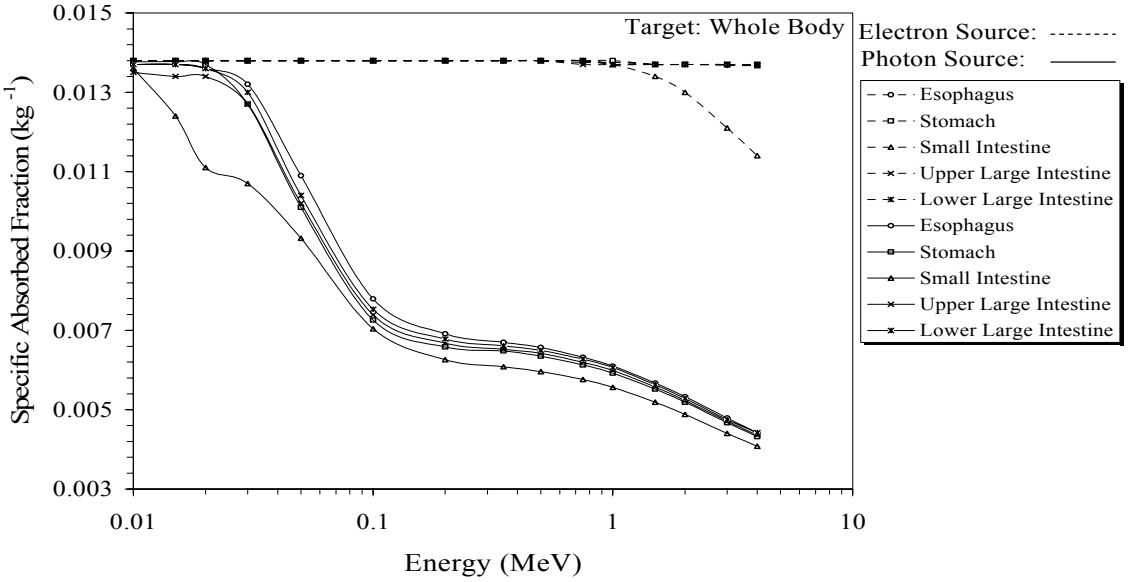


Figure 8(h)

**Figs. 8(a-h).** Specific Absorbed Fractions (SAFs) in various organs and tissues from 15 uniformly distributed monoenergetic electron and photon sources in the lumenal contents of the five sections of the gastrointestinal tract of an adult human male or a larger-than-average-female (72.63 kg).

Primarily, the distance between a source and a target determines the photon SAF for a given energy. The greater the distance, the smaller is the SAF value. The effects of the size and shape of the source organ on the photon SAF for other organs were not investigated. The separation between two SAF curves for the same target with two different sources is relatively small for energies above 50 keV while the separation is relatively large and increases rapidly with decreasing energy below 40 keV. This behavior reflects the same processes of photon interaction as discussed before.

The curves of photon SAFs for the whole body (Fig. 8(h)) are different in pattern than those for the other organs. The SAF is almost constant for the energies 10-20 keV for all the source organs, except the SI, because the source energy is completely absorbed within body. The complete absorption of the source energy gives an SAF-value in the body that is equal to $1.38 \times 10^{-2}$ $kg^{-1}$ (=1/72.63 kg). For the SI, a fraction of the source energy in two of the 8 loops of the SI, those directed in the y-direction, escapes from the body even for the energy as low as 15 keV. Above 20 keV, the SAF decreases for all source organs with increasing energy as the penetrability increases with the energy.

A preliminary comparison of photon SAFs obtained in this research with those obtained by Cristy and Eckerman showed that the two values differ by a factor of 1.5 to 3. Generally, the difference is the highest at low energies (<30 keV) and the lowest at the medium energies (100-500 keV). But a detailed comparative study of photon SAF values obtained in this research with those obtained in other studies was not performed.

Figures 8(a)-8(g) demonstrate that the electron SAF values are smaller by several orders of magnitude than the photon SAFs for the same energy in a given source-target pair. But, for the whole body, the electron SAFs are greater than the photon SAFs. For target organs other than the source organs, the electron SAFs for most targets in the body are due only to the bremsstrahlung radiation. The electron SAFs for the same target and source are discussed later. A large portion of the source electron energy is absorbed within the source organ.

A source electron contributes directly to the SAF if the target organ is located within the range of the electron. Figure 8(a) shows that the electron SAF for the active bone marrow abruptly increases with increasing energy for the energies above 1.5 MeV when the source organs are ULI, LLI, and the ESP. This is because the pelvis, which contains more than one-third of the active bone marrow, is located within the range of these electrons in the ULI and the LLI while the ribs and the middle spine, containing 19% and 17% of the active marrow, respectively, are located within the range of these electrons in the ESP. These three organs become critical for the active bone marrow for high energy electrons (>3 MeV). At these high energies, the electron exposure is significant for the liver and the lungs when source in the ESP and ST (Figs. 8(c) and 8(d)), and for the testes and the urinary bladder wall when the source in the LLI (Figs. 8(e) and 8(g)). These curves indicate that the electron SAF may be greater than the photon SAF for very high energies (>4 MeV).

Figure 8(h) shows that the electron SAF is greater than the photon SAF in the whole body. The electron SAF is almost constant for all the source organs except the SI

over the energy range investigated (10 keV – 4 MeV). For the SI, the electron SAF decreases with increasing energy for energies above 1 MeV.

Electron SAFs at different depths or positions in the walls from uniformly distributed sources of 15 monoenergetic electrons in the lumenal contents of the five sections of the GIT are shown in Figs. 9(a) – 9(e). The depths were measured from the wall-contents interface. Also shown are positions of the most radiosensitive stem cells and different regions across the wall, namely mucus layer, epithelium for the ESP, gastric pit for the ST, villus and crypt for the SI, and crypt for the ULI and the LLI, for interpreting the doses at different distances from the contents.

The SAF within the penetration depth or range of the source electrons is a strong function of depth. The SAFs decrease several orders of magnitude over this short distance. The "stopping power" of source electrons determines the steepness of SAF curve. For lower energy electrons (higher stopping power), the SAF curves fall very rapidly with steep slope. The SAF at depths beyond the range becomes almost flat and decreases slowly with almost a constant logarithmic relation that depends on the energy of the source electrons. Beyond the range of the source electron, bremsstrahlung radiation and fluorescent x-rays are the only contributors to the SAF (Figs. 9(a) and 9(b)) for all organs except the ESP. For the ESP, direct electron exposure also contributed to the SAF in the outer layers of the wall; because the outer layers of the middle ESP with closed lumen were irradiated directly by a fraction of the source electrons in the lumen of the lower ESP in which the majority of its lumen was empty. Figure 9(a) shows the bremsstrahlung and fluorescent x-ray contribution to the SAF for the depths beyond the

electron range of 10 keV electrons in the ESP. The esophageal SAF curves for electron energies from 10 keV-1 MeV rise at around 4250 μm, thus forming a hump. This is due to the direct exposure of source electron to the outer layers of the wall of the middle ESP. Similar humps are seen in the ULI SAF curves (Fig. 9(d)) at 1850 μm. This was because of the outer layers of the wall of the transverse colon were irradiated by source electrons in the ascending colon, which is mostly empty.

As shown in the Figs. 9(b)-9(e) and in Table II-2**,** the SAF curves for 10-keV electrons decrease by about 4 orders of magnitude over the distances 3-4 μm**,** consistent with the electron range in soft tissue, for all the source organs except the ESP. For the ESP, the SAF decrease rate is smaller. Generally, 200-keV electrons can barely penetrate a 500 μm thickness of soft tissue. Therefore, for the energies below 200 keV, the electron doses decrease sharply to negligible levels before penetrating the insensitive tissue layers overlying the stem cells (Figs. 9(a)-9(e)). The doses to the bottom of the esophageal

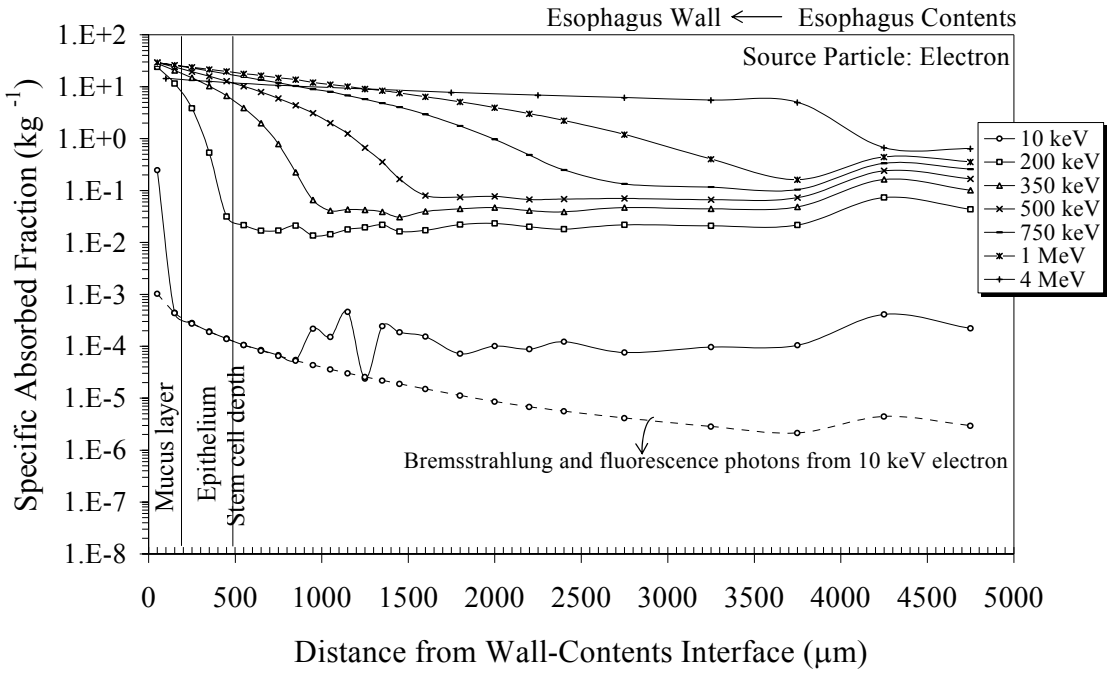
Esophagus Wall ⟵ Esophagus Contents
Source Particle: Electron
Specific Absorbed Fraction (kg -1)
1.E+2
1.E+1
1.E+0
1.E-1
1.E-2
1.E-3
1.E-4
1.E-5
1.E-6
1.E-7
1.E-8
Mucus layer
Epithelium
Stem cell depth
10 keV
200 keV
350 keV
500 keV
750 keV
1 MeV
4 MeV
Bremsstrahlung and fluorescence photons from 10 keV electron
0
500
1000
1500
2000
2500
3000
3500
4000
4500
5000
Distance from Wall-Contents Interface (μm)

Figure 9(a)

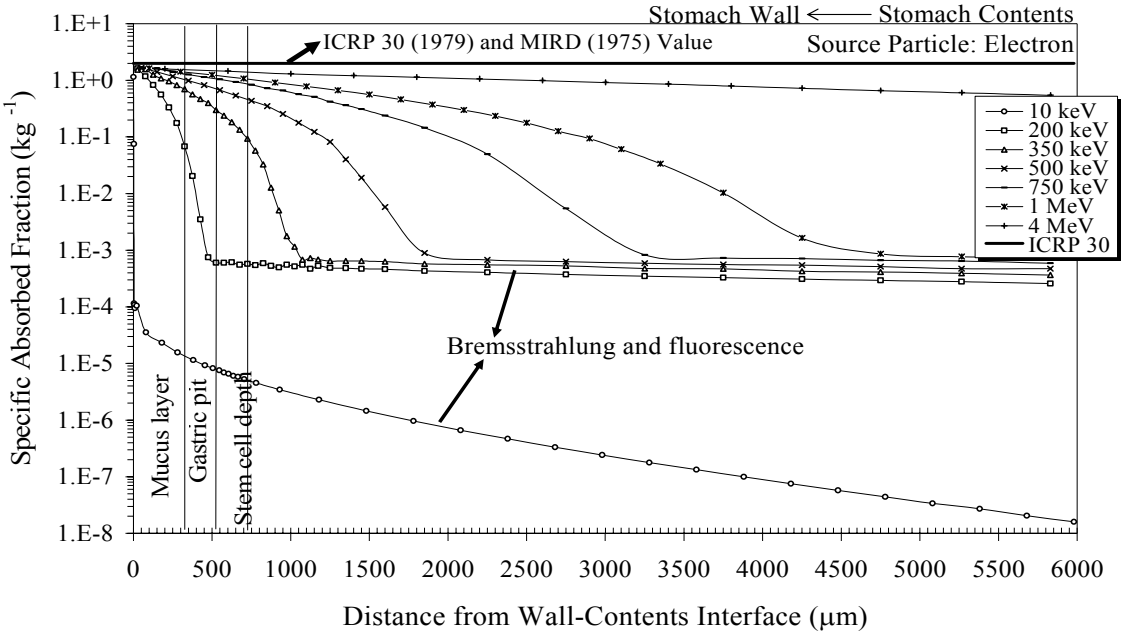
Stomach Wall ⟵ Stomach Contents
Source Particle: Electron
ICRP 30 (1979) and MIRD (1975) Value
10 keV
200 keV
350 keV
500 keV
750 keV
1 MeV
4 MeV
ICRP 30
Bremsstrahlung and fluorescence
Mucus layer
Gastric pit
Stem cell depth
Specific Absorbed Fraction (kg -1)
Distance from Wall-Contents Interface (μm)

Figure 9(b)

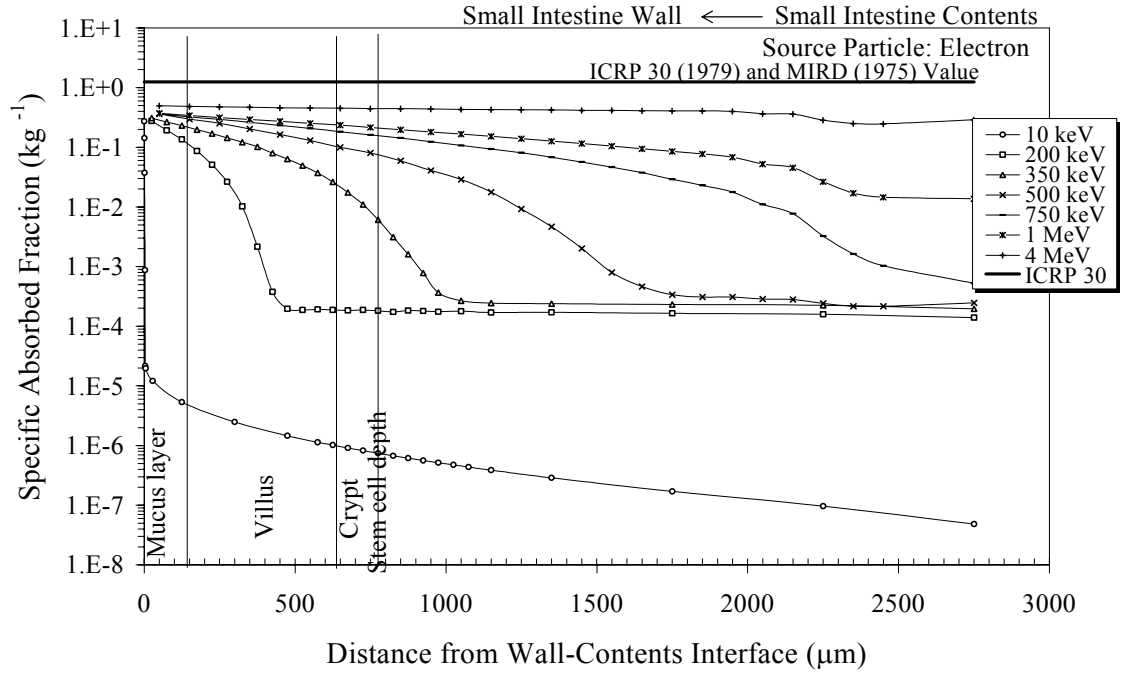
Small Intestine Wall ⟵ Small Intestine Contents
Source Particle: Electron
ICRP 30 (1979) and MIRD (1975) Value
10 keV
200 keV
350 keV
500 keV
750 keV
1 MeV
4 MeV
ICRP 30
Mucus layer
Villus
Crypt
Stem cell depth
Specific Absorbed Fraction (kg -1)
Distance from Wall-Contents Interface (μm)

Figure 9(c)

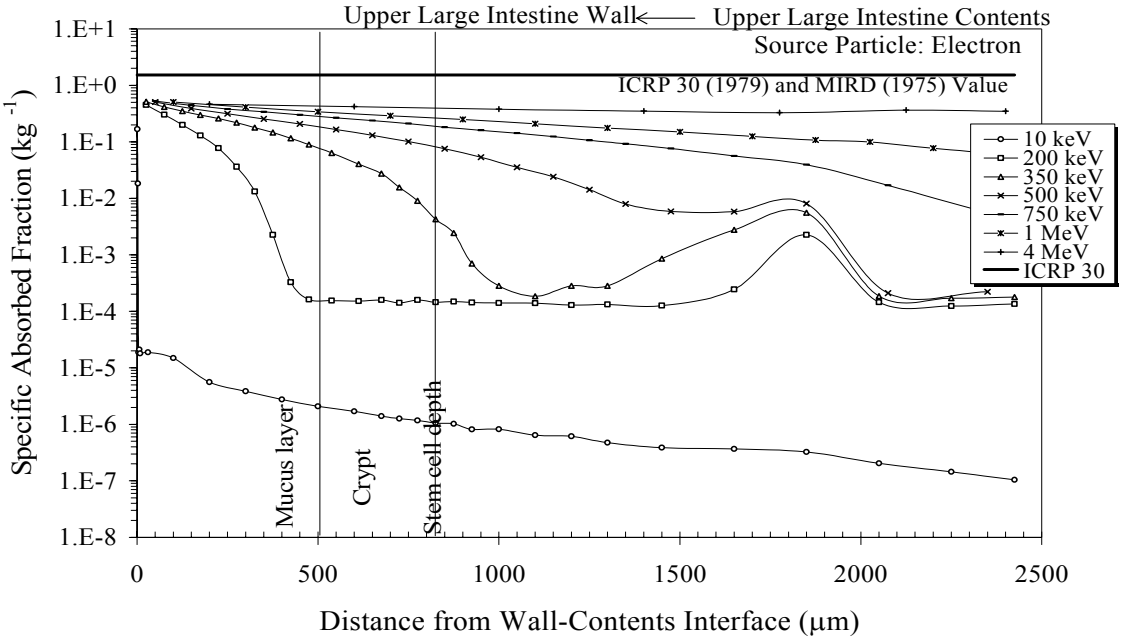


Figure 9(d)

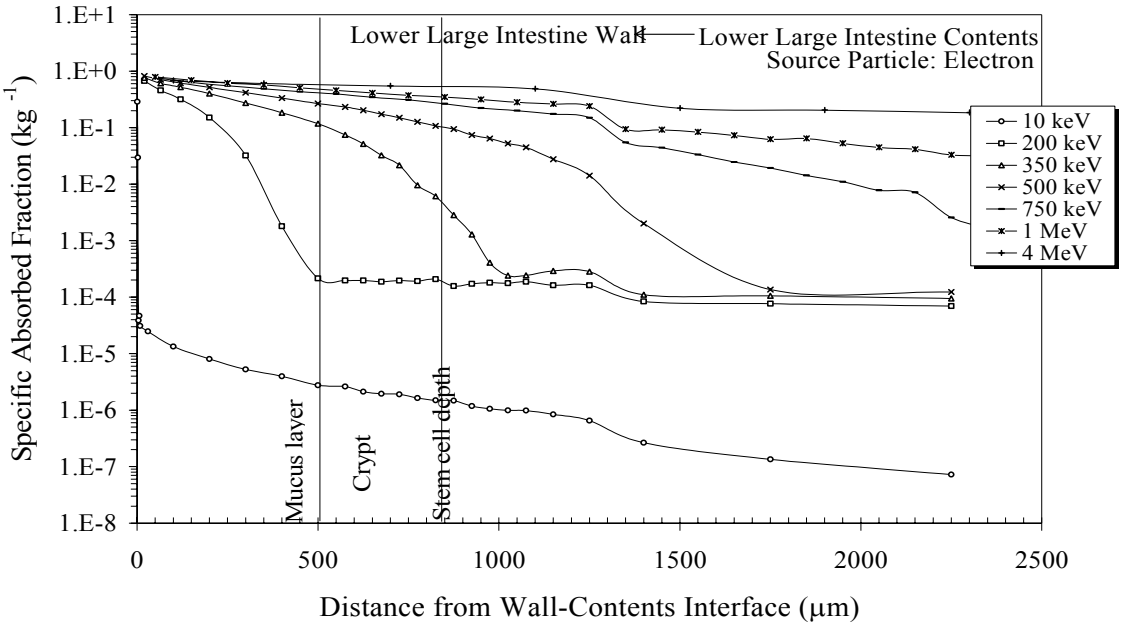


Figure 9(e)

**Figs. 9(a-e).** Specific Absorbed Fractions (SAFs) at different depths or positions in the walls from 15 uniformly distributed monoenergetic electron sources in the lumenal contents of the five sections of the Gastrointestinal Tract of an adult human male or a larger-than-average-female (72.63 kg). The depths were measured from the wall-contents interface. The ICRP 30 (1979) and MIRD (1975) SAF values for the stomach, small intestine, and upper large intestine are shown here for comparison purposes.

epithelium, to the gastric glands in the ST, to the villi and crypts in the SI, and to the crypts in the ULI and LLI are markedly lower than the doses at the contents-mucus interface for electron energies less than 200 keV. For 350-keV electrons, the dose has fallen off by more than a factor of 1.5 before reaching the villus tip (at a depth of 210 μm), more than a factor of 25 before reaching the bottom of the villi (710 μm) and more than an order of magnitude before reaching at the bottom of the crypt. The radiosensitive stem cells are located near the base of each intestinal crypt at 800-850 μm depth, which

is equal to the penetration depth of 300-keV electrons in soft tissue. Thus, below 300 keV, the doses to the stem cells are due only to bremsstrahlung radiation. A 300-keV electron, originating in the vicinity of the contents-mucus interface, can barely reach the stem cell level and contributes only a small dose to the stem cells. For electron energies above 300 keV, the average dose to stem cells increases rapidly with energy. This rapid increase, shown in Figs. 9(a)-9(e), results from the fact that more electrons with higher average energies can now reach the stem cell depth. The SAF values are almost constant across the walls of all the sections of the GIT for 4-MeV electrons.

It is interesting to note that SAF values are 2.0 $kg^{-1}$ for the ST, 1.25 $kg^{-1}$ for the SI, 1.52 $kg^{-1}$ for the ULI, and 3.7 $kg^{-1}$ for the LLI based on both the MIRD (1975) and the ICRP (1979) dosimetric formulations for weakly-penetrating radiations in the walled organs. Regardless of the source particle energy, the SAFs are constant across these walls while Figs. 9(a)-9(e) demonstrate that the SAF has a strong dependence on electron energy as well as the distance of the target tissues from the wall-contents interface. For a given energy, the SAF varies by several orders of magnitude across the wall thickness.

## PREVIOUS APPROACHES

Let us digress briefly to discuss the MIRD (1975) and the ICRP (1979) dosimetric formulations for non-penetrating radiations. The absorbed dose to hollow organs from non-penetrating (np) radiations (alpha, beta, conversion electrons or Auger electrons, etc.) emitted in their contents was assumed to be the dose at the surface of the

wall, which was approximated as one-half the equilibrium dose to the contents volume under radiation equilibrium conditions (MIRD 1975; ICRP 1979). Using this υ approximation, the specific absorbed fraction for the wall as the target organ and contents as the source organ, SAF (Wall ← Cont) is

$$\text{SAF (Wall} \leftarrow \text{Cont)} = \frac{1}{2M_{cont}}\nu \qquad (1)$$

where $MB_{contB}$ is the mass of the contents and υ is a factor between 0 and 1 representing the degree to which the radiation penetrates to the cells at risk. Regardless of the radition energies, the value of υ was set to 1.0 in both the MIRD (1975) and ICRP (1979) dosimetric formulations for weakly-penetrating radiations.

The use of unity for the value of υ ignores radiation penetrability to the cells at risk. The dose at the interface was considered as the dose to the organ. There was enough evidence that the stem cells are the most radiosensitive and critical of the all five sections of GIT. This suggets that the absorbed dose to the stem cells should represent the dose to these sections rather than the interface dose that was routinely reported as the organ dose. If the stem cell dose represents the wall dose, then υ in Eq. 1 corresponds to the ratio of the absorbed dose to the stem cells to the absorbed dose at interface.

To prevent confusion, we have defined a parameter, called ε, that represents, for our calculations, the ratio of the absorbed dose (or SAF) to the stem cells to the absorbed dose (or SAF) at contents-mucus interface. The values of ε, listed in Table 2 for the energies 10 $keV^{-4}$ MeV for the all five sections of the GIT. The table shows that the ε varies from $2.6 \times 10^{-6}$ at 10 keV to $9.0 \times 10^{-1}$ at 4 MeV.

Therefore, the routinely reported absorbed doses that are calculated using Eq. (1) with υ taken as 1 are severe overestimates of the actual doses to the radiosensitive target cells (stem cells) for energies below 750 keV. For electron energies above 2 MeV, the value of ε is close to unity. The ε-values shown in Table 2 suggests that ICRP and MIRD models are not overly conservative for mid-energy electrons (1-4 MeV). However, more accurate dose estimates must use the appropriate ε-values for the weakly-penetrating

Table 2. Ratio ($\varepsilon$) of electron SAF at mean depth of stem cells (radiosensitive cells) to SAF at contents-mucus interface of the five sections of the GIT.

| Source / Organ / Energy (MeV) | $\varepsilon$ | | | | |
|---|---|---|---|---|---|
| | ESP | ST | SI | ULI | LLI |
| 0.01 | 5.00E-04 | 4.27E-06 | 2.60E-06 | 6.25E-06 | 5.192E-06 |
| 0.015 | 9.99E-04 | 1.97E-05 | 1.86E-05 | 2.76E-05 | 2.53E-05 |
| 0.02 | 1.43E-03 | 4.30E-05 | 5.88E-05 | 6.23E-05 | 5.07E-05 |
| 0.03 | 1.19E-03 | 9.48E-05 | 8.62E-05 | 1.17E-04 | 9.11E-05 |
| 0.05 | 1.08E-03 | 1.75E-04 | 2.60E-04 | 1.93E-04 | 1.65E-04 |
| 0.10 | 7.00E-04 | 2.30E-04 | 5.02E-04 | 2.14E-04 | 1.79E-04 |
| 0.20 | 1.10E-03 | 3.54E-04 | 6.45E-04 | 3.22E-04 | 3.11E-04 |
| 0.35 | 1.87E-01 | 6.03E-02 | 1.49E-02 | 8.30E-03 | 8.06E-03 |
| 0.50 | 3.93E-01 | 2.94E-01 | 1.92E-01 | 1.62E-01 | 1.30E-01 |
| 0.75 | 5.64E-01 | 5.19E-01 | 4.20E-01 | 3.58E-01 | 3.61E-01 |

| | | | | | |
|---|---|---|---|---|---|
| 1.00 | 6.41E-01 | 6.56E-01 | 5.55E-01 | 5.28E-01 | 4.49E-01 |
| 1.50 | 5.58E-01 | 7.34E-01 | 6.96E-01 | 6.44E-01 | 5.87E-01 |
| 2.00 | 6.26E-01 | 7.99E-01 | 7.78E-01 | 7.11E-01 | 6.64E-01 |
| 3.00 | 4.87E-01 | 8.64E-01 | 8.55E-01 | 8.19E-01 | 7.32E-01 |
| 4.00 | 5.05E-01 | 8.65E-01 | 9.00E-01 | 8.57E-01 | 7.56E-01 |

particle-emitting radionuclides typically used in the nuclear medicine procedures, as well as for other internal dosimetery calculations.

Two other grossly incorrect assumptions were made to formulate equation (1). It was assumed that walled organs are cylindrical in shape with the lumen full of contents. And it was assumed that the wall was irradiated in a $2\pi$-geometry by the source only in the luminal contents. Based on these assumptions, the absorbed dose at the contents-wall interface was approximated as one-half the equilibrium dose to the contents. This approximation is known as "ICRP one-half approximation." Based on this approximation, the SAF at the interface should be 1.92 $kg^{-1}$ for the ST, 0.1.79 $kg^{-1}$ for the SI, 3.33 $kg^{-1}$ for the ULI, and 5.26 $kg^{-1}$ for the LLI if the masses of the contents of these organs modeled in this study were used. But our calculations showed that the SAFs at the interfaces were energy dependent and varied between 1.2 and 1.7 $kg^{-1}$ for the ST, 0.3 and 0.5 $kg^{-1}$ for the SI, 0.17-0.53 $kg^{-1}$ for the ULI, and 0.3 and 0.8 $kg^{-1}$ for the LLI. This is because the walled organs, except for the ST, were not full of contents and the walls were irradiated in more than $2\pi$-geometry.

Photon SAFs also were calculated at different depths in the wall of the five sections of the GIT (see Table II-2). For 10-keV photons, the SAFs across the wall vary

by one or two orders of magnitudes depending on the wall thickness. Above 50-keV photons, the SAFs are almost constant across the wall of all these organs. At a given depth, the SAF increases with increasing energy in the low-energy range while it decreases with energy for high energies. This is due to the same photon interaction processes as discussed earlier in this section. In comparison with the results of Cristy and Eckerman, the photon SAFs obtained with this new model differ by about a factor of 2 to 3, except for the ST. For the ST, the SAFs are almost constant in the two studies. It is noted that the two models of the ST are identical in shape and size but are different in the position and orientation in the body. If we consider the SAF at the stem cell position instead of an average value for the entire wall, then the SAFs to the stem cell layer at about 730 μm differ by a factor of about 2.8 for 10-keV photons. The difference gradually diminishes as photon energy increases.

Thus far the discussion has focused on the SAFs due to the "self absorption." That is, situations in which the target and the source are the same organ. We also calculated both photon and electron SAFs due to "cross irradiation." Now the target is different from the source organ. Table II-2 shows results on SAF distributions across the walls for 15 monoenergetic electron and photon sources for all possible source-target combinations. A few points should be mentioned here. Electron SAFs from cross irradiation are not significant, except for the energies above 1 MeV for the following source-target combinations: SI-ULI, SI-LLI, ULI-LLI, and vice versa. Also, cross irradiation is important when the source is the ESP and the target is the ST. But photon SAFs due to the cross irradiation are significant for all source-target combinations for all

energies, except for low-energies when the target is separated by one photon free path from the source.

## CONCLUSIONS

Electron transport studies using the MCNP computer code and a new model of the gastrointestinal tract (GIT) showed that the energy absorbed, or SAF, at the depth of radiosensitive critical cells (stem cells) from electrons emitted in the lumenal contents is a small fraction of the dose routinely estimated at the contents-mucus interface. This fraction increases with increasing electron energy from $2.6 \times 10^{-6}$ to $9.0 \times 10^{-1}$ (with some variation between two sections of the GIT) over the energy range 10 keV-4 MeV. These results clearly demonstrated that the interface dose, which is routinely reported as the "wall" dose (ICRP and MIRD model), might be a severe overestimation of the actual dose to the stem cells for many electron energies (10-500 keV)**.** This fraction for radionuclides emitting very low-energy electrons (<200 keV) is negligibly small, and thus the dose from these radionuclides in the SI contents may be ignored. For low-energy electrons, between 300 keV and 500 keV, the use of the ICRP and MIRD model may overestimate the absorbed dose by orders of magnitude. The ICRP and MIRD model may be conservative for electron energies up to 4 MeV. Appropriate correction factors should be applied for radionuclides emitting weakly-penetrating radiations in the energy range 10 keV – 4 MeV. The results from the calculations for 10 keV – 4 MeV electrons indicate that the model may be closely fit for very energetic electrons (>4 MeV) penetrating through the walls of the GIT**.**

This study demonstrated that the absorbed energies or SAFs for electron sources in the luminal contents of the walled organ were a strong function of distance into wall. Thus, knowing the depth of the target tissue layer, which was considered to be the stem cells in this study, is very important for electron dosimetry in a walled organ.

The "cross dose" or the SAFs due to "cross irradiation" from electron sources is not significant except for the energies above 1 MeV for following source-target combinations: SI-ULI, SI-LLI, ULI-LLI, and vice versa. Also it is important when the source is the ESP and the target is the ST, but is not important when the source is the ST and the target is the ESP. The results showed that the ULI and the LLI were significant sources of radiation for the active marrow and the ovaries for electron energies greater than 2 MeV. The ST as a source is important for the liver and the lungs for the electrons with energies above 3 MeV. Generally, the "cross dose" can be ignored for the electrons with energies below 2 MeV.

Photon transport studies using the revised GIT model showed that the photon SAFs across the wall vary by one or two orders of magnitude depending on the wall thickness for 10 keV photons. Above 50 keV, the SAFs became almost constant across the wall of all the five sections of the GIT. At a given depth, the SAF increases with increasing energy in the low-energy range while it decreases in the high-energy range. The study also showed that the average energy or average SAF to the entire wall was significantly different from that of the radiosensitive cell layer. These results led to the conclusion that the absorbed dose to the radiosensitive cells (e.g., stem cells) should be

reported as the organ dose instead of using the average dose for the energies below 50 keV.

The photon SAFs due to the cross irradiation were significant for all source-target combinations except the source-target separated by a distance comparable to the mean free path of the photons under consideration.

The photon SAFs obtained using the revised model differ by a factor of 1.5 to 3 from photon SAF results obtained by Cristy and Eckerman. Generally, the difference between the two values is highest at low-energies (<30 keV) but lowest at the medium energies (100-500 keV). This difference is mainly attributed to the difference between the two models.

These results may be used to modify currently accepted values of the annual limits on intake (ALI) for 188 radionuclides for which the GIT is significantly irradiated (ICRP 1979). New derived air concentration (DAC) may be recommended based on these calculations.

REFERENCES


Attix FR. Introduction to radiological physics and radiation dosimetry. New York: John Wiley & Sons; 1986: 193-197.

Berger, MJ. Energy deposition in water by photons from point isotropic sources. MIRD Pamphlet No. 2. New York: Society of Nuclear Medicine; 1968.

Bhuiyan NU. A revised dosimetric model for calculation of electron dose in the small intestine. M.S. Thesis, College Station, Texas: Texas A&M University; 2000.

Briesmeister JF. ed. MCNP—A general Monte Carlo N-particle transport code. Version 4A. Los Alamos, NM: Los Alamos National Laboratory; Report LA-12625-M; 1993.

Briesmeister JF. ed. MCNP—A general Monte Carlo N-particle transport code. Version 4C. Los Alamos, NM: Los Alamos National Laboratory; Report LA-12625-M; 2000.

Brownell GL, Ellett WH, Reddy AR. Absorbed fractions for photon dosimetry. MIRD Pamphlet No. 3. New York: Society of Nuclear Medicine; 1968.

Cristy M, Eckerman KF. Specific absorbed fractions of energy at various ages from internal photon sources. I. Methods. Oak Ridge, Tennessee: Oak Ridge National Laboratory; ORNL/TM-8381; 1987.

Evans RD. The atomic nucleus. New York: McGraw-Hill; 1955.

Heitler W. The quantum theory of radiation. 3rd ed. Oxford: Oxford University Press; 1954.

International Commission on Radiological Protection (ICRP). Report of the task group on reference man. Oxford: Pergamon Press; ICRP Publication 23; 1975.

International Commission on Radiological Protection (ICRP). Limits for intakes of radionuclides for workers. Oxford: Pergamon Press; ICRP Publication 30; 1979.

International Commission on Radiological Protection (ICRP). 1990 recommendations of the International Commission on Radiological Protection. Oxford: Pergamon Press; ICRP Publication 60; 1991.

International Commission on Radiological Protection (ICRP). Publication on the human alimentary tract (HAT). Online at http://www.icrp.org/pdf/g_REM_Chapter_6_Alimentary_System.pdf. November 15, 2001.

Jönsson L, Liu X, Jönsson B, Ljungberg M, Strand SA. dosimetry model for the small intestine incorporating intestinal wall activity and cross-doses. J Nucl. Med. 43:1657-1664; 2002.

Loevinger R. Distributed radionuclide sources. In: Attix FH, Tochilin E. Eds. Radiation dosimetry, 2nd ed. New York: Academic Press; 1969: 51-90.

Poston JW, Jr., Kodimer KA, Bolch WE, Poston JW, Sr., Calculation of absorbed energy in the gastrointestinal tract. Health Phys. 71:300-306; 1996a.

Poston JW, Jr., Kodimer KA, Bolch WE, Poston JW, Sr. A revised model for the calculation of absorbed energy in the gastrointestinal tract. Health Phys. 71:307-314; 1996b.

Snyder WS, Ford MR, Warner GG, Watson SB. A tabulation of dose equivalent per microcurie-day for source and target organs of an adult for various radionuclides. Oak Ridge, Tennessee: Oak Ridge National Laboratory; ORNL-5000; 1974.

Snyder WS, Ford MR, Warner GG. "S", absorbed dose per unit cumulated activity for selected radionuclides and organs. MIRD Pamphlet No. 11. New York: Society of Nuclear Medicine; 1975.

Snyder WS, Ford MR, Warner GG. Estimates of specific absorbed fractions for photon sources uniformly distributed in various organs of a heterogeneous phantom. MIRD Pamphlet No. 5 (Revised). New York: Society of Nuclear Medicine; 1978.

Stubbs JB, Evans JF, Stabin MG. Radiation absorbed doses to the walls of hollow organs. J Nucl. Med. 39:1989-1995; 1998.

Warner GG, Craig AM, Jr. ALGAM, a computer program for estimating internal dose from gamma-ray sources in a man phantom. Oak Ridge, Tennessee: ORNL-TM-2250, Oak Ridge Natl. Lab.; 1968.

Warren LH. ed. Gray's anatomy of the human body. New York: Bartleby.com; Online at www.bartleby.com/107/; 2000.

## APPENDIX I

PHANTOM

The phantom used in this research was modeled as erect with three major sections: (1) an elliptical cylinder representing the trunk that includes the arms and the pelvic region to the crotch; (2) two truncated circular cones representing the legs and feet; and (3) an elliptical cylinder capped by half an ellipsoid representing the head and neck. The origin of the coordinate system is located at the center of the base of the trunk section. The positive z-axis extends upward through the head. The positive x and y axes extend to the phantom's left and the posterior of the phantom, respectively. All dimensions given in the description are in units of centimeters.

The trunk of the phantom was described by:

$$\left(\frac{x}{20}\right)^2 + \left(\frac{y}{10}\right)^2 \le 1 \text{ and } 0 \le z \le 70 .$$

The legs were described by:

$$5\left(x^2 + y^2\right) \le \pm x(100 + z) \text{ and } -80 \le z \le 0 ,$$

where the "±" sign was taken as plus for the left leg and the minus for the right leg. The head was given by

$$\left(\frac{x}{8}\right)^2 + \left(\frac{y}{10}\right)^2 \le 1 \text{ and } 70 \le z \le 86.85 ,$$

$$\text{or } \left(\frac{x}{8}\right)^2 + \left(\frac{y}{10}\right)^2 + \left(\frac{z - 86.85}{7.15}\right)^2 \le 1 \text{ and } z > 86.86 .$$

## THE REVISED GIT MODEL

The revised GIT model consisted of five sections — the esophagus, stomach, small intestine, upper large intestine, and lower large intestine. Prior to the description of the each section, the anatomic and histologic features of each section important to photon and electron dosimetric modeling will be described to provide the bases for the model.

### Esophagus

*Anatomic and histologic information.* The esophagus, the narrowest and proximal tubular part of the GIT, is a collapsible muscular tube that, in humans, extends—about 21-30 cm with a mean of 25 cm in the adult male and 20-26 cm with a mean of 23 cm in the adult female—from the laryngopharynx to the stomach. The esophageal wall weighs about 23-50 g with a mean of 37 g in the adult male and about 25-50 g with a mean of 34 g in the adult female (Tipton and Cook 1969, ICRP 23 1975, ICRP HAT document 2001). The esophageal structure varies spatially along its length. There is a temporal variation in the esophageal structure as well. At a given location along the length, the esophagus assumes three distinct structures at three states of peristalsis, which is produced by coordinated waves of circular muscle contraction and local longitudinal muscle shortening made in reflex response to the distension of the GIT walls by a swallowed bolus of food. The peristalsis, triggered by swallowing or deglutition, propagates distally and propels the bolus downward along the length of the esophagus. The three peristaltic states—distension, contraction, and resting—were detected by high-frequency intralumenal ultrasonography techniques in a number of recent studies

(Taniguchi et al. 1993; Miller et al. 1995; Yamamoto et al. 1998; Balaban et al. 1999; Pehlivanov et. el. 2001; Nicosia et. al. 2001). The esophageal wall thickness decreases as intralumenal contents distend the wall in the distension state. The distension state is followed by the contraction state in which the wall muscles contract transversely and shorten longitudinally in a reflex response to the distension, thus increasing the wall thickness. The lumen is closed at the peak contractions (Pehlivanov et al. 2001). The esophagus structure returns to the resting state (before swallowing or the distension) with the muscle layer that is thicker than in distension and is thinner than in contraction. When the esophagus is empty in the resting state, the mucosa and submucosa are thrown into longitudinal folds thus closing its lumen (Pehlivanov et. el. 2001; Bolch et al. 2002).

Pehlivanov et al. (2001) recorded ultrasound images of the esophagus of 15 healthy adult humans. The recordings were made in the resting state and at the peak of swallow-induced contraction in the lower esophageal sphincter (LES), which opens into the ST, and at 2, 4, 6, 8, and 10 cm above the LES. The esophageal muscle in the resting state was measured to be significantly higher in the LES compared with the rest of the esophagus where it was somewhat thicker in the distal compared with the proximal esophagus, as shown in Table I-1. The muscle was significantly thicker at peak contraction than in the resting state at each level (see Table I-1).

Using the same ultrasonography technique, Nicosia et al. (2001) studied *in vivo* the temporal variations in esophageal muscle thickness and geometry during peristalsis. They recorded muscle thicknesses (circular plus longitudinal) in the middle esophagus at the three states. The recorded minimum was 0.9 mm at the distension while the

maximum was 3 mm at the peak contraction. At the resting state, the mean thickness was found to be 1.38 ± 0.07 mm. They did not mention the total wall thickness of the esophagus.

In a critical review, ICRP (1975) reported that the esophagus in the adult human is 3.5-5.6 mm in wall thickness, 13-19 mm in diameter in the contraction state and 16-22 mm in diameter in the distension state.

Ultrasound images showed that the geometry of the esophagus was circular or elliptical during peak contraction and "slit-like" in appearance in the resting and distended states (Pehlivanov et al. 2001; Nicosia et al. 2001). Thus, the esophagus is elliptical in shape with varying major-to-minor-axes-ratio depending on the peristaltic states.

**Table I-1.** Muscle layer thickness in three different states at different levels of the esophagus (Pehlivanov et. el. 2001).

| Level | Resting thickness (mm)[(a)] | | Thickness at peak contraction (mm)[(a)] | |
|---|---|---|---|---|
| | Mean | | Mean | |
| LES[(b)] | 1.92 ± 0.14 | 1.13 ± 0.16 | 2.54 ± 0.13 | 2.17 ± 0.32 |
| 2 cm | 1.28 ± 0.09 | | 2.31 ± 0.17 | |
| 4 cm | 1.14 ± 0.09 | | 2.16 ± 0.16 | |
| 6 cm | 1.09 ± 0.06 | | 2.20 ± 0.15 | |
| 8 cm | 1.07 ± 0.07 | | 2.15 ± 0.15 | |
| 10 cm | 1.06 ± 0.06 | | 2.04 ± 0.14 | |

[(a)] Values are means ± SE
[(b)] LES stands for lower esophageal sphincter

The esophageal wall contains all four of the basic alimentary canal tissue layers. From the lumen outward, these layers are the mucosa, submucosa, muscularis externa, and serosa (or adventitia). As mentioned previously, the esophageal wall thickness varies due to the spatiotemporal variation within an individual. There is a variation between

individuals as well. The wall in the adult is about 3.5-5.6 mm thick in which the mucosa is about 500-800 μm (ICRP 1975). The mucosal epithelium is composed of nonkeratinized stratified squamous cells and is relatively thick, about 300 μm in the adult (ICRP HAT document 2001). The basement membrane (basal layer) of the epithelium consists of the most radiosensitive stem cells that give rise to the epithelium. Overlying the epithelium, there is a thick coating of mucus that serves as a protective barrier and makes the esophageal lumen slippery, facilitating the passage of a food bolus.

Despite the actual variability in the stem cell depth due to the variation in the thicknesses of the mucus layer and epithelium lining, for dosimetry purposes the stem cell depth was assumed to be an average of 500 μm. This depth is based on a mucus thickness 200 μm added to the average epithelium thickness of 300 μm (ICRP HAT document 2001). Thus, the absorbed dose to the esophagus was defined as the absorbed dose at a depth of 500 μm.

*Esophagus model.* The esophagus model represents an adult male esophagus 27 cm in length with a food bolus in the distal region which is in the distension state. The model includes the resting state in the proximal region and the contraction state in the middle region. These three peristaltic states in three regions are modeled by dividing the esophageal length into three segments, each 9 cm in length but with different diameters. From the proximal to distal, these segments are: (1) "upper esophagus," an elliptical solid cylinder with radii of 0.9 cm and 0.4 cm representing a slit-like appearance of the proximal esophagus with closed lumen at resting state; (2) "middle esophagus," an

elliptical solid cylinder with radii of 0.8 cm and 0.5 cm representing the middle esophagus with closed lumen at contraction state; and (3) "lower esophagus," consisting of two concentric elliptical cylinders with the inner radii of 0.7 cm and 0.4 cm, and the outer radii of 1.1 cm and 0.8 cm representing the lumen and the wall of the distal esophagus in the distension state. Note that contents are only in the lower esophagus as this segment has a lumen while the other two segments are solid regions without lumen. The same wall thickness, 0.4 cm, is used for both the upper esophagus at resting and the lower esophagus in distension because the decrease in the wall thickness caused by changing the states from resting to distension is compensated by the increase in the thickness along the length from proximal to distal. The wall of the middle esophagus in contraction is thicker and is assumed to be 0.5 cm. The characteristic parameters of each segment describe an average structure of one of the three peristaltic states. The variation during the period of a particular state is not considered in this model.

The esophagus, in relation to other organs, is placed in the phantom in an approximately true anatomic position (Warren 2000). The upper and the middle esophagus run vertically downward along the front of the middle spine, slightly behind the midline of the phantom. The lower esophagus passes the midline and deviates to the left as it descends obliquely from posterior to anterior and ends at the postero-superior surface of the stomach. A small portion of the middle and lower esophagus intercepts the heart. The upper and middle esophagus are defined by

$$\left(\frac{x-x_0}{a}\right)^2+\left(\frac{y-y_0}{b}\right)^2\le 1,$$

$$\text{and } z_1 \le z \le z_2 .$$

The wall plus contents of the lower esophagus are represented by two coaxial elliptical cylinders. The wall is defined by the space between the two cylinders:

$$\left(\frac{x'}{a}\right)^2 + \left(\frac{y'}{b}\right)^2 \le 1,$$

$$\left(\frac{x'}{a-d}\right)^2 + \left(\frac{y'}{b-d}\right)^2 \ge 1,$$

$$\text{and } z_1 \le z' \le z_2 .$$

The contents are defined by the space within the inner cylinder:

$$\left(\frac{x'}{a-d}\right)^2 + \left(\frac{y'}{b-d}\right)^2 \le 1,$$

$$\text{and } z_1 \le z' \le z_2 .$$

The $(x', y', z')-$coordinate system is related to the $(x, y, z)$-coordinate system by the following rotation-translation equation, given in matrix form:

$$\begin{bmatrix} x' \\ y' \\ z' \end{bmatrix} = \begin{bmatrix} 0.9063 & 0.2424 & 0.3462 \\ 0.0 & 0.8192 & -0.5736 \\ -0.4226 & 0.5198 & 0.7424 \end{bmatrix} \begin{bmatrix} x - x_0 \\ y - y_0 \\ z - z_0 \end{bmatrix}.$$

The above coordinate transformation as a result of the combination of a translation of the origin to $(x_0, y_{0,} z_0)$ and two rotations, the first being clockwise rotation about *x*-axis through an angle 35° and the second being counterclockwise rotation about the new $y'$ axis through an angle 25°. The constants used in the above equations are presented in Table I-2.

**Table I-2.** Parameters describing the adult human esophagus in the new model.

| Sub-section | $x_0$ | $y_0$ | $z_0$ | $a$ | $b$ | $d$ | $z_1$ | $z_2$ | Mass (g) | |
|---|---|---|---|---|---|---|---|---|---|---|
| | | | | | | | | | Wall | Contents |
| Upper Esophagus | 0.0 | 2.0 | - | 0.9 | 0.4 | - | 57.2 | 66.2 | 10.69 | - |
| Middle Esophagus | 0.0 | 2.0 | - | 0.8 | 0.5 | - | 48.2 | 57.2 | 11.88 | - |
| Lower Esophagus | 0.0 | 2.0 | 48.2 | 1.1 | 0.8 | 0.4 | -9.0 | 0.0 | 17.81 | 8.23 |

Each of the three esophageal sections is divided into many shell volumes by using many closely spaced coaxial elliptical cylinders. The thicknesses of these shell volumes are in the range of 1-1000 μm depending on the location of the shells and on the energy of the radiation to be transported.

The characteristic parameters that describe the esophagus in the current dosimetry model as well as in Reference Man (ICRP 1975) and in the ICRP HAT document (2001) are summarized in Table I-3.

**Stomach**

*Anatomic and histologic information.* The stomach, the most distensible part of the GIT, is a J-shaped pouch that provides a temporary storage area of the ingested food and where chemical digestion of proteins begins. It is located left of the midline of the trunk and is immediately inferior to the diaphragm, which separates it from the base of the left lung. The stomach is connected at its proximal end to the esophagus by the lower esophageal sphincter (or cardiac orifice) and at the distal end to the duodenum of the small intestine via the pylorus sphincter, but it is quite flexible in between. The shape, size and position of the stomach vary largely with the posture, with the amount of the stomach contents and with the condition of the intestines on which it rests. The stomach may be cylindrical or roughly crescent shaped when empty of food or pear-shaped when

partially distended, but the most common form in the erect posture is the fish-hook or J-shape. A full ST assumes an oblique position between the ES and the duodenum in erect posture (ICRP 1975; NCRP 1998; Graaff and Fox 1999; Warren 2000; ICRP HAT document 2001; Bolch 2002).

The stomach wall is made up of the same four basic layers of tissues, as is the majority of the GIT, with some differences in the microscopic anatomy that allow its unique digestive functions. For example, the additional third layer of smooth muscle in the muscularis externa enables the stomach to churn, mix, and pummel ingested food, as well as propel the ingesta along the length of the organ through peristalsis. The mucosa of the stomach wall is covered by a single layer of columnar epithelium 20 to 40 μm thick (Trier and Winter 1989; NCRP 1998). The surface epithelium is entirely composed of mucus secreting goblet cells. The surface epithelium is indented by millions of pits, called gastric pits, each about 200 μm deep and 70 μm in diameter (Trier and Winter 1989). These gastric pits are invaginations of the surface epithelium into the submucosa. At the bottom of each gastric pit are one or more secreting glands resembling cylinders with inner diameters in the range of 5 to 10 μm and inner lengths in the range of 200 to 500 μm (Allen 1989). The gland contains radiosensitive stem cells at a depth of approximately 200 μm (Trier and Winter 1989). The secreting glands are divided into three categories based on their role in stomach digestion: the cardiac glands occurring in the region just below the cardiac orifice secrete mucus; the pyloric glands occurring near the duodenum secrete mainly mucus but also gastrin and pepsinogen; and the gastric

**Table I-3.** Parameters describing the adult human esophagus in the new model and in other references.

| Characteristic Parameters | Reference | | | | |
|---|---|---|---|---|---|
| | ICRP Reference Man (1975) | ICRP HAT (2001) | New Model | | |
| | | | Upper Esophagus at Resting | Middle Esophagus in Contraction | Lower Esophagus in Distension |
| Geometry | — | — | Elliptical Cylinder | Elliptical Cylinder | Elliptical Cylinder |
| Length (cm) | 25 (23-30)[1] | 25 (21-30)[1] | 9.0 | 9.0 | 9.0 |
| Outer Radius/Radii (cm) | 0.65-0.95[2] 0.80-1.10[3] | — | 0.9, 0.4 | 0.8, 0.5 | 1.1, 08 |
| Lumen Radius/Radii (cm) | — | — | Closed | Closed | 0.7, 0.4 |
| Wall Mass (g) | 40 | 37 ± 6 | 10.69 | 11.88 | 17.81 |
| Wall Thickness (cm) | 0.35-0.56 | 0.35-0.56 | — | — | 0.4 |
| Contents' Mass (g) | — | — | — | — | 8.23 |
| Transit Time (s) | — | 47/10.3 | — | — | — |
| Mucus Thickness (μm) | — | — | 200 | 200 | 200 |
| Epithelium Thickness (μm) | — | 300 | 300 | 300 | 300 |
| Stem Cell Depth (μm) | — | — | 500 | 500 | 500 |
| Mucosal Layer Thickness (μm) | 500-800 | — | — | — | — |

[1] Average length with the range in parenthesis is presented.
[2] In the contraction state.
[3] In the distension state.

glands occurring between these two extremities host a number of different cells that secrete various enzymes and hormones, hydrochloric acid, mucus and other products such as gastrin, histamine, endorphins, serotonin, etc.

The surface epithelium of the mucosa is exposed to a very corrosive and acidic mixture of the gastric secretions. The epithelial cells wear out and are constantly replaced through cell division of undifferentiated stem cells residing within the glands located at the base of the gastric pits. The entire surface epithelium is replaced every 2-6 days while the turnover time for the glandular cells is longer.

The mucus thickness varies along the length of the stomach. A large variation is observed in the measured values of the wall thickness as well. Measurement techniques considerably influence the measurement result. Two techniques are commonly used for measuring the thickness of the mucus layer on unfixed, fresh mucosa: 1) an indirect method in which a slit lamp and pachymeter are used to measure the mucus thickness over a mucosa bathed with solution; and 2) direct observation of unfixed sections of mucosa by light microscope. The pachymeter is an image-splitting device that allows the measurement of optically distinct objects (i.e., the objects with different refractive indexes) to an accuracy of ± 20 μm. The mucus layer is translucent, thus readily distinguishable from the underlying mucosa. But the site of the mixing boundary between the insoluble mucus gel phase and the bulk lumenal fluid phase is not clearly observed by the pachymeter because the refractive indexes are almost equal. So a component of the bathing solution is added to the mucus layer in the pachymeter measurement. As a result, the measured value might be greater than the actual thickness. Direct observation by light microscope is a relatively simple and more reliable method because the contours of the two phases are clearly observed in this method (Allen 1989).

The mucus thickness was reported to be 192-652 μm (Bickel and Kauffman 1981; Kerss et al. 1982) and 50-450 μm with an average of 180 μm (Allen 1989). Stubbs et al. (1998) assigned 180 μm for the mucus thickness in their stomach model.

Underlying the mucus layer is the mucosa with a thickness of 0.3-2.5 mm (ICRP 1975; ICRP HAT document 2001). The stomach wall is 0.6-1.3 cm thick (ICRP 1975) and with a mass of 110-450 g and an average of 150 g for the adult male and 140 g for

the adult female (ICRP 1975; Tipton and Cook 1969). The mass of the contents was 250 g, taken directly from Eve's review (1966). The reference value for the mass of the contents in the ICRP HAT document (2001) was based largely on autopsy measurements on 15 accident victims (Eve 1966) and was taken to be 175 g for the adult male and 160 g for the adult female. These values are lower than those derived by Eve, who relied more on theoretical considerations than autopsy measurements and who assumed a considerably longer transit time for fluids than that considered in the ICRP HAT document (30-45 minutes for adult male) (ICRP HAT document 2001). The total transit time for stomach contents was taken to be 70 minutes for the adult male and 95 minutes for the adult female in the ICRP HAT document (2001).

The parameters describing the stomach in the current dosimetric model, and in various other models and references, are presented in Table I-4.

*Stomach model.* The stomach was modeled as a full stomach. The stomach is located left of the midline of the trunk with the long axis inclined left making a 45-degree angle with the phantom z-axis. As the stomach is inclined, it reaches as far as the bottom of the left lung. The postero-superior surface of the stomach is in contact with the bottom of the ES while the postero-inferior surface touches the antero-superior surface of the duodenum. The liver is on the right side of the ST.

The wall and the contents of the stomach are represented by two concentric ellipsoids with the centroid at (4.05, -4.0, 37.1) and with radii 4.0 cm, 3.0 cm and 8.0 cm for the outer ellipsoid, and 3.387 cm, 2.387 cm and 7.387 cm for the inner ellipsoid. The

dimensions of these ellipsoids are the same as those used in the Cristy and Eckerman model (1987).

**Table I-4.** Parameters describing the adult human stomach in the new model and in various other dosimetry models and references.

| Characteristic Parameters | Reference | | | | | | | |
|---|---|---|---|---|---|---|---|---|
| | ICRP Reference Man (1975) | MIRD Model (Snyder et al. 1978) | ICRP Model (1979) | Cristy & Eckerman (1987) | Poston et al. (1996) | Stubbs et al. (1998) | ICRP HAT (2001) | New Model |
| Model Geometry | — | Ellipsoid/ Cylinder[(1)] | Ellipsoid/ Cylinder[(1)] | Ellipsoid | Ellip-soid | Ellip-soid | — | Ellip-soid |
| Outer Dimensions (cm) | 37, 15, 11 | 8, 4, 3 | 8, 4, 3 | 8, 4, 3 | 8, 4, 3 | 8, 4, 3 | — | 8, 4, 3 |
| Wall Mass (g) | 150 | 148 | 148 | 158 | 158 | 158 | 150±46 | 156.5 |
| Wall Thickness (cm) | 0.6-1.3 | 0.613 | 0.613 | 0.613 | 0.613 | 0.613 | — | 0.613 |
| Contents Mass (g) | 250 | 247 | 247 | 260 | 260 | 260 | 175 | 260 |
| Transit Time (h) | — | — | 1 | — | — | — | 1.17 | 1.17 |
| Mucus Thickness (μm) | — | — | — | — | — | 180 | — | 300±100 |
| Gastric Pit Height (μm) | — | — | — | — | — | 200 | — | 200 |
| Stem Cell Depth (μm) | — | — | — | — | 100-300 | 600 | — | 730±100 |
| Mucosal Layer Thickness (μm) | 500-2500 | — | — | — | 0-300 | — | 300-1500 | — |

[(1)] Ellipsoid for penetrating radiations and cylinder for weakly penetrating radiations (beta, conversion electron, Auger electron, etc.).

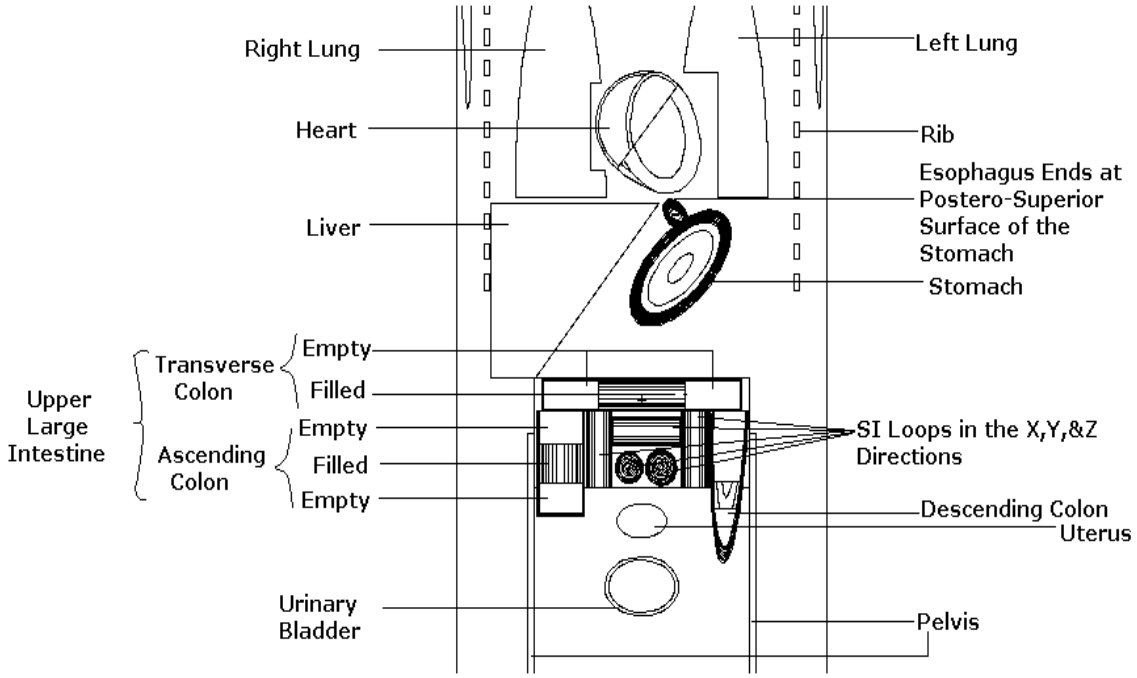


**Fig. I-1.** Front view of the trunk sectioned along the coronal plane y = -2.36 cm in a reference frame centered at the base of the trunk. The y-axis is directed towards the posterior side of the phantom and the x-axis is directed to the phantom's left.

The stomach wall was represented by the volume between the two concentric ellipsoids. The contents were represented by the volume within the inner ellipsoid. The wall was defined by:

$$\left(\frac{x'}{4.0}\right)^2+\left(\frac{y'}{3.0}\right)^2+\left(\frac{z'}{8.0}\right)^2\le 1,$$

$$\text{and } \left(\frac{x'}{3.387}\right)^2+\left(\frac{y'}{2.387}\right)^2+\left(\frac{z'}{7.387}\right)^2\ge 1.$$

The contents were defined by:

$$\left(\frac{x'}{3.387}\right)^2+\left(\frac{y'}{2.387}\right)^2+\left(\frac{z'}{7.387}\right)^2< 1.$$

The primed coordinate system, $(x', y', z')$, is related to the $(x, y, z)$-coordinate system by the following rotation-translation equation, given in matrix form:

$$\begin{bmatrix} x' \\ y' \\ z' \end{bmatrix} = \begin{bmatrix} 0.7071 & 0.0 & -0.7071 \\ 0.0 & 1.0 & 0.0 \\ 0.7071 & 0.0 & 0.7071 \end{bmatrix} \begin{bmatrix} x - 4.05 \\ y + 4.0 \\ z - 37.1 \end{bmatrix}.$$

The above coordinate transformation is the result of the combination of a translation of the origin to $(4.05, -4.0, 37.1)$ and a clockwise rotation about the *y*-axis through a 45° angle.

Thus, the stomach wall is 0.613 cm thick and has a 152 $cm^3$ volume. The volume of the contents is 250 $cm^3$. The wall and contents, each are divided into many shell volumes by using many closely spaced concentric ellipsoids. The space between two adjacent ellipsoids gives the thicknesses of these shell volumes that are in the range of 1-1000 μm depending on the location of the shells as well as on the energy of the radiation to be transported.

**Small Intestine**

*Anatomic and histologic information.* The SI is a convoluted tube that in adult humans extends about 3 m in living persons (~ 6 m in cadavers due to muscle relaxation) from the pyloric sphincter of the ST to the ileocecal valve, which opens into the LI. Based on the function and histologic structure, the SI is divided into three regions: the duodenum, jejunum and ileum. The duodenum (~25 cm long), the first portion of the SI, is a relatively fixed C-shaped tube facing the concave surface to the left around the head of the pancreas. The jejunum and ileum (~110 cm and ~165 cm long, respectively) hang

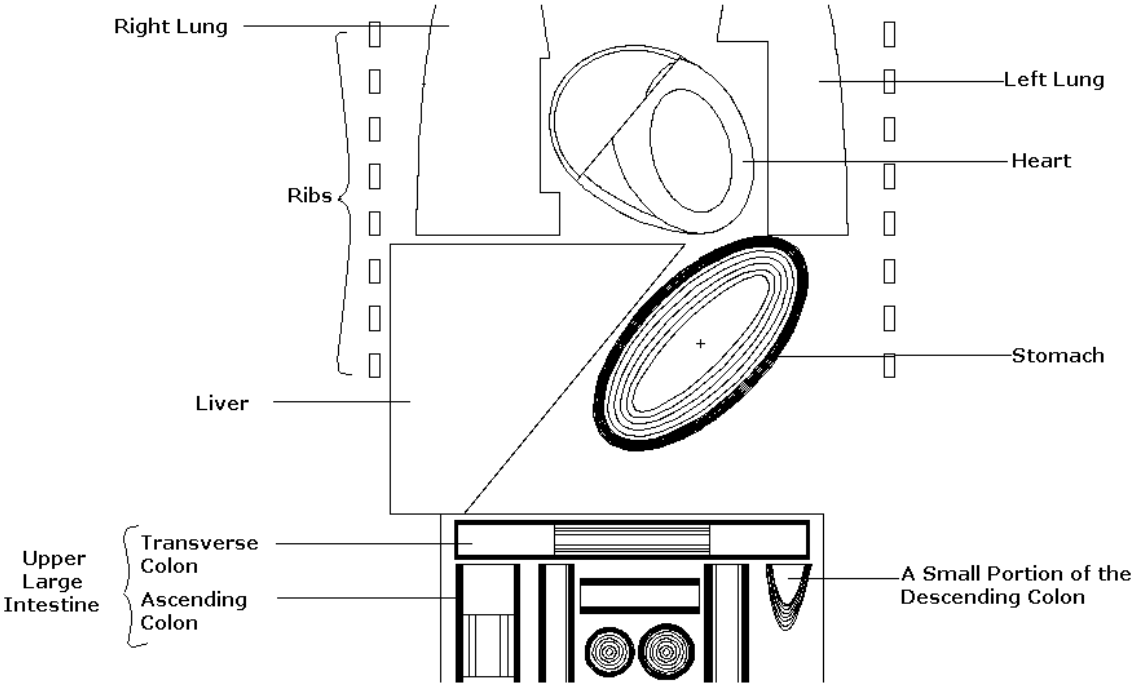


**Fig. I-2.** Front view of the stomach inclined to the left by 45° with spatial relation to the lungs, liver, heart, ribs, and the intestine. The trunk sectioned along the coronal plane y = -4 cm in a reference frame centered at the base of the trunk. The y-axis directed toward the posterior side of the phantom and the x-axis directed to the phantom's left.

within the central and lower part of the abdominal cavity suspended by extensions (mesentery) of the peritoneum (serous membrane covering the abdominal cavity), and are bounded by the large intestine laterally and superiorly. The attachment of mesentery to the SI allows peristaltic movement with little chance of becoming twisted and kinked.

The SI wall is made up of the same four basic layers of tissues, as is the majority of the GIT, with certain modifications to allow the processes of digestion and absorption. From the lumen outward, these layers are the mucosa, submucosa, muscularis externa, and serosa (or adventitia). Each layer, or tunic, of the wall has a dominant tissue type that performs specific functions in the digestive processes. The mucosa, or mucous

membrane, has three components: a single cell thick surface epithelium that lines the lumen, an underlying stroma composed of a vascularized, highly cellular, reticular connective tissue (lamina propia), and a thin layer of smooth muscle (mascularis mucosae). The surface epithelium, which is the site of secretion and absorption, and serves as a protective barrier, is folded to form millions of finger- or leaf-like projections (areal density = 20 to 40 per $mm^2$) called villi into the lumen. The epithelium at the base of each villus invaginates downward to form narrow pouches that open through pores to the lumen. These structures are called the intestinal crypts (crypts of Lieberkühn). The epithelial cells of the villi are predominantly columnar cells specialized for nutrient absorption, and interspersed among these are the mucus-secreting goblet cells. The epithelial cells that line the crypts secrete intestinal juice, a mixture of water and mucus, and antibacterial enzyme lysozome. A large surface area of the epithelium is made available, for digestive and absorptive activities, by the mucosal circular folds (plicae circulares), by crypts, by villi, and by microvilli (thousands of tiny finger-like projections formed by folding of the cell membrane of each absorptive cell on the villus epithelium).

All the differentiated cell lineages of the intestinal epithelium are derived from common multipotent stem cells located near the base of each crypt (Cheng and Leblond 1974). A stem cell in the crypt divides in the normal intestine to produce a daughter stem cell (self renewal) and a more rapidly replicating transit cell. The transit cell, in turn, undergoes four to six rapid cell divisions in the proliferative zone located in the lower half of each crypt. These nascent cells undergo terminal differentiation as they migrate

upward from the zone of proliferation onto the villus epithelium. Eventually, the differentiated epithelial cells are sloughed off as they reach the villus tip, whereby homeostasis of the normal adult intestinal epithelium is maintained (Cheng and Leblond 1974; Gordon and Hermiston 1994; Potten et al. 1997a, 1997b). The undifferentiated cells, especially the stem cells, in the crypts are the most radiosensitive. Hence, the stem cell region is considered to be the critical region for radiation damage to the small intestine.

The anatomic and histologic information required for constructing the geometry of the SI has been gleaned from currently available textbooks and journal articles, ICRP Publication 23 (1975) on Reference Man and Eve's review (1966). Wide variability in the data was observed for some parameters such as lumen diameter, wall thickness and villus height.

A marked structural variation is observed along the length of the small intestine within an individual and between individuals. The variations are in the range of 0.2-0.4 cm in wall thickness and of 1.9-3.1 cm in lumen diameter (Golden 1959; Eve 1966; Gray 1974; ICRP 1975; Solomon and Davis 1978; Tortora and Evans 1986; Haubrich et al. 1995; Marieb 1998). The small intestine gradually diminishes in size from its beginning to its end. The duodenum wall is the thickest and the lumen is the widest while the ileum is the thinnest and the narrowest. Based on this review, the duodenum is 3.0 cm in lumen diameter and 0.3 cm in wall thickness, the jejunum is 2.7 cm in lumen diameter and 0.3 cm in wall thickness, and the ileum is 2.4 cm in lumen diameter and 0.25 cm in wall thickness.

No quantitative information was available on the mucus thickness of the SI. There are a few qualitative analyses found in the open literature. McClean et al. (1996) reported that about half of the mucosal surface of the SI is covered by a mucus gel of variable thickness. The mucus thickness in the duodenum is, in spite of the differences in epithelial surface topology, similar to that in the ST (Flemstrom et al. 1999). The mucus thickness of the stomach was reported to be 192-652 μm (Bickel and Kauffman 1981; Kerss et al. 1982) and 50-450 μm with an average 180 μm (Allen 1989). The mucus thickness of the stomach was taken to be 300±100 μm in the current model. Thus, the mucus thickness of the duodenum was assumed to be 300±100 μm. For the jejunum and ileum, the average mucus thickness was taken as 150±50 μm, which is half the stomach mucus thickness. Note that half of the SI length is devoid of mucus.

The villi appear in different shapes, sizes and numbers in the three regions of the small intestine. In the duodenum the villi are short, leaf-like folds; the villi in the jejunum are rounded, finger-like projections; and those in the ileum tend to have a club-like form. Villi typically are taller and more numerous in the jejunum than in the ileum (ICRP HAT document 2001). The literature suggests that a mean villus height of 500±45 μm is a good average over the range of 300-1500 μm for an adult human SI (Jos 1962; Eve 1966; ICRP 1975; Penna et al. 1981; Stenling et al. 1984; Leeson et al. 1985; Tortora and Evans 1986; Johnson et al. 1987; Trier and Winter 1989; Fawcett 1994; Haubrich et al. 1995; Guyton 1996).

Based on the information on the crypts of Lieberkühn, it was concluded that 150 ± 12 μm was reasonable for the mean crypt depth of an adult human with a range of 120-

170 μm; 45 ± 7 μm was the mean crypt width; 143 ± 25 μm was the mean height from Paneth to top (crypt-villi junction); and 135 ± 20 μm was the mean height of the stem cells measured from the junction (Eve 1966; Penna et al. 1981; Stenling et al. 1984; Potten and Booth 2000). The SI parameters obtained in the review are summarized in Table I-5.

*Distance from contents to the critical cells.* A definite distance between the stem cells and the contents is difficult to specify because of the irregularities of the lumenal surface caused by the presence of protruding villi and indented crypts of Lieberkühn on the internal surface of the SI, and the considerable variations in the number and size of these structures along the SI length. If it is assumed that the crypt space and the space between the villi is filled with material of similar scattering and energy-absorbing properties as that of the wall material, and no contents or more specifically, no source, is present therein, the stem cell distance from the contents is the summation of mucus thickness, villus height and the depth of the stem cells in the crypt measured from the villi-crypt junction. A representative total distance can be obtained from the corresponding mean values of these parameters. Indeed, the crypt lumen is filled with exocrine secretions and mucus, and overflows into the intestinal lumen via the crypt lumen. The scattering and energy-absorbing properties are almost the same, except for mucus, as the soft tissues comprising the SI wall (ICRP 1975). If the ICRP (1975) values for the villus diameter of 130 μm and the number of villi per square millimeter of 75 are used to estimate the gaps between villi, one can show that the villi are closely packed without gaps. However, many of the reported values for the number of villi per unit area

vary from 10 to 40 per $mm^2$ (Eve 1966; Fawcett 1994; Guyton 1996). Nevertheless, the 150 μm mucus thickness on each of the nearer sides of the adjacent villi, along with the exocrine secretions and mucus overflowing from the crypt seems to be sufficient material to fill the space between villi. Eve (1966), quoting Creamer, mentioned that all solid and insoluble materials in the lumen contents are separated from the mucosa by a sheet of mucus. He added that a soluble substance might flow through the mucus and up the crypts to arrive in the mitotic stem cell area. However, it may be necessary to take into account the irregularities of the surface and the small fraction of the source getting into the crypts (ICRP 1975). Since the objective was to calculate an average dose to the critical region, a "representative distance" may be chosen and the small fraction of the source that might be present in the crypt and between the villi may be ignored As outlined earlier, "representative distances" from the contents-wall interface to the critical cells are 935 μm for the duodenum (obtained by adding 300, 500 and 135 μm) and 785 μm for jejuno-ileum region (obtained by adding 150, 500 and 135 μm). The error or standard deviations associated with these distances were obtained using the "error propagation formula" for a normal distribution.

*Small intestine model.* The structural and functional variations along the length of the small intestine were incorporated into the small intestine model by using three different geometries. The duodenum, which was not considered separately in the previous SI models, is part of the SI in the current model. Three-quarters of two concentric circular tori with the axis parallel to the y-axis represents the wall plus lumen of the C-shaped duodenum. Eight circular cylinders with the axes directed in the x, y, and z-directions

**Table I-5.** Parameters describing the adult human small intestine in the new model, and in other models and references.[a]

| Parameter | Reference | | | | | | | | | |
|---|---|---|---|---|---|---|---|---|---|---|
| | ICRP Reference Man (1975) | MIRD Model (Snyder et al. 1978) | ICRP Model (1979) | Cristy & Eckerman (1987) | Poston et al. (1996a) | Stubbs et al. (1998) | Bhuiyan (2000) | ICRP HAT Model (2001) | Jönsson et al. (2001) | New Model |
| Model Geometry | — | Cylinder/ Solid Region[b] | Cylinder/ Solid Region[b] | Solid Region | Cylinder | Cylinder | Cylinder | — | Cylinder | D: Torus<br>J-IL: Cylinder<br>R: Solid Region |
| Length (cm) | D: 25<br>J: 190<br>IL: 285<br>Total: 500 | — | — | — | 21 | 10 | 10 | 300 | 300 | D: 20.26<br>J: 104.90<br>IL: 174.84<br>Total: 300 |
| Lumen Radius (cm) | D: 2<br>J: 1.25-2<br>IL: 1-1.9 | — | 1.0 | — | 1.246 | 1.0 | 1.4 (0.95-1.55) | 1.5 | 1.25 | D: 1.5<br>J: 1.35<br>IL:1.20<br>R: Closed Lumen |
| Wall Mass (g) | D: 60<br>J: 280<br>IL: 300<br>Total: 640 | Total Mass (wall+contents) 1046 | 640 | Total Mass (wall+contents) 1102.4 | 168 | 40.1 | 30.4 | D: 56±9<br>J: 280±39<br>IL: 310±33<br>Total: 650 | — | D: 64.9<br>J-IL: 535.1<br>Total: 650 |
| Wall Thickness (cm) | D: 0.3-0.5<br>J: 0.3<br>IL: 0.2-0.5 | 0.3-0.4 | 0.2-0.3 | — | 0.754 | 0.5 | 0.3 (0.2-0.4) | — | 0.3 & 0.6 | D: 0.30<br>J: 0.30<br>IL: 0.25 |
| Contents Mass (g) | 400 | 400 | 400 | — | 106.5 | 32.7 | 64.0 | 280 | — | D: 10.98<br>J-IL: 269.02<br>Total: 280 |
| Transit Time(h) | — | — | 4.0 | — | — | — | — | 4.0 | — | 4.0 |

**Table I-5** — *continued*

| Parameter | Reference | | | | | | | | | |
|---|---|---|---|---|---|---|---|---|---|---|
| | ICRP Reference Man (1975) | MIRD Model (Snyder et al. 1978) | ICRP Model (1979) | Cristy & Eckerman (1987) | Poston et al. (1996a) | Stubbs et al. (1998) | Bhuiyan (2000) | HAT (2001) | Jönsson et al. (2001) | New Model |
| Mucus Thickness (μm) | — | — | — | — | — | 200 | 210±57 | — | 5-200 | D: 300±100<br>J-IL: 150±50 |
| Villus Height (μm) | 700 | — | 500-1500 | — | — | 500 | 500±45 | — | 500 | 500±45 |
| Crypt Depth (μm) | — | — | 20-450 | — | — | 150 | 150±12 | — | 150 | 150±12 |
| Stem Cell Position (μm) | — | — | — | — | 300-600 | 150 | 135±20 | — | — | 135±20 |
| Stem Cell Depth (μm) | — | — | — | — | — | 850 | 845±75 | — | — | D: 935±111<br>J-IL: 785±70<br>Avg.: 790 |
| Mucosal Layer Thickness (μm) | — | — | — | — | 449±141 | — | — | — | — | — |

[(a)] In the table, D stands for duodenum; J stands for jejunum, IL stands for Ileum; J-IL stands for Jejuno-ileum region; R stands for remnant.

[(b)] Solid region for strongly penetrating radiations (photon) and cylinder for weakly penetrating radiations (beta, conversion electron, Auger electron, etc.).

represent the jejuno-ileum folds in different orientations. Each cylinder, 7 cm in length, consists of two coaxial cylinders. The inner cylinder has the ends closed by two circular discs, each 0.25 cm in width, and represents the lumen (6.5 cm in length). The space between the cylinders represents the wall (7 cm in length). Of the eight cylinders, three with a total wall length of 21 (= 3 × 7) cm and 19.5 (= 3 × 6.5) cm in total lumen length represent the jejunum with filled lumen. The remaining five cylinders, with smaller radii, but each with the same 7 cm length, represent the ileum with thinner walls and narrower lumen with full contents. The remnant of the jejuno-ileum region is modeled as a solid region without lumen. The "remnant" represents that part of the SI where the lumen is empty and closed. The majority of the jejuno-ileum region is empty with a closed lumen, this has been delineated in this model. The folds are not considered in the remnant as the "cross-dose" to the remnant without folds is not considerably different from the dose with the folds. In addition, there is no source in the remnant. The sources are homogenously distributed in the contents of the other regions. The remnant is not directly exposed by the sources as the lumen ends are closed.

The C-shaped duodenum with the axis parallel to the y-axis is positioned around the neck of the pancreas and between the stomach and the transverse colon. The antero-superior surface of the duodenum touches the postero-inferior surface of the stomach and the antero-inferior surface of the duodenum touches the posterior surface of the transverse colon. The jejuno-ileum region, bounded laterally by the ascending and descending colons and superiorly by the transverse colon, occupies the same space defined by Snyder (1974) and later adopted by Cristy and Eckerman (1987) for the SI in

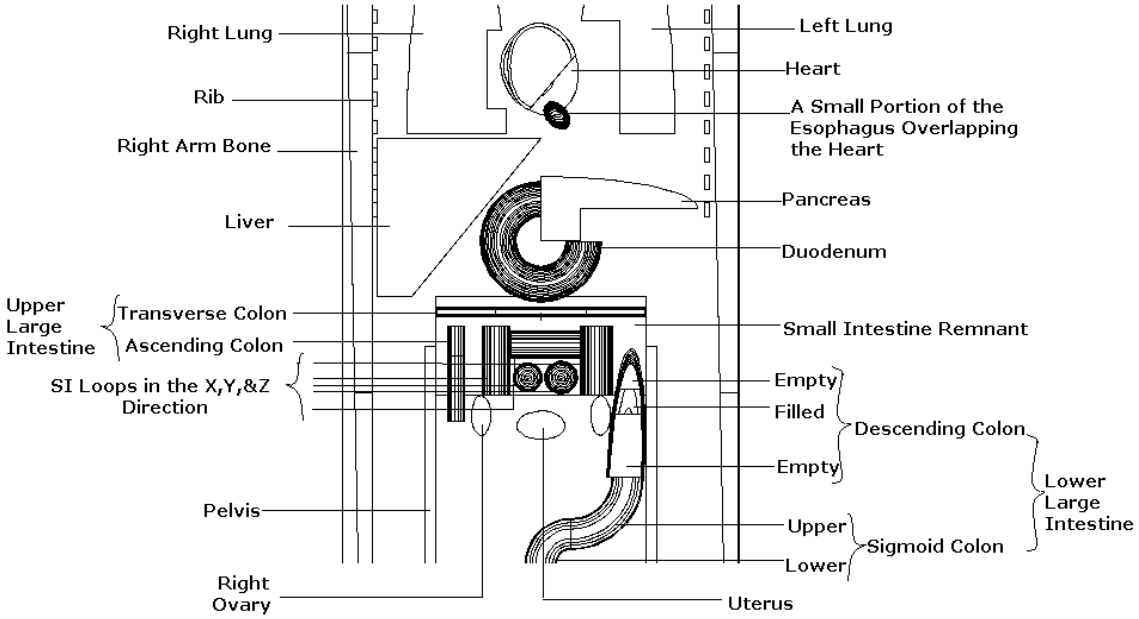


**Fig. I-8.** Front view of the trunk sectioned along the coronal plane y = 0 in a reference frame centered at the base of the trunk. The y-axis directed toward the posterior of the phantom and the x-axis directed to the phantom's left.

their phantoms. The parameters for each subsection are based on anatomic data. Dose calculations were corrected for any deviation from true anatomic data.

The upper portion of the **duodenum wall,** which is one quarter of the space between two concentric tori, is defined by:

$$\left(\sqrt{(x)^2+(z-32.6)^2}-4.3\right)^2+(y)^2 \le (1.8)^2,$$

$$\left(\sqrt{(x)^2+(z-32.6)^2}-4.3\right)^2+(y)^2 \ge (1.5)^2,$$

$$\text{and } x \le 0, \text{ and } z \ge 32.6\,.$$

The lower portion of the **duodenum wall,** which is one-half the space between two concentric tori, is defined by:

$$\left(\sqrt{(x)^2+(z-32.6)^2}-4.3\right)^2+(y)^2 \le (1.8)^2,$$

$$\left(\sqrt{(x)^2+(z-32.6)^2}-4.3\right)^2+(y)^2 \ge (1.5)^2,$$

and $x \le 0,$ and $z \ge 32.6$.

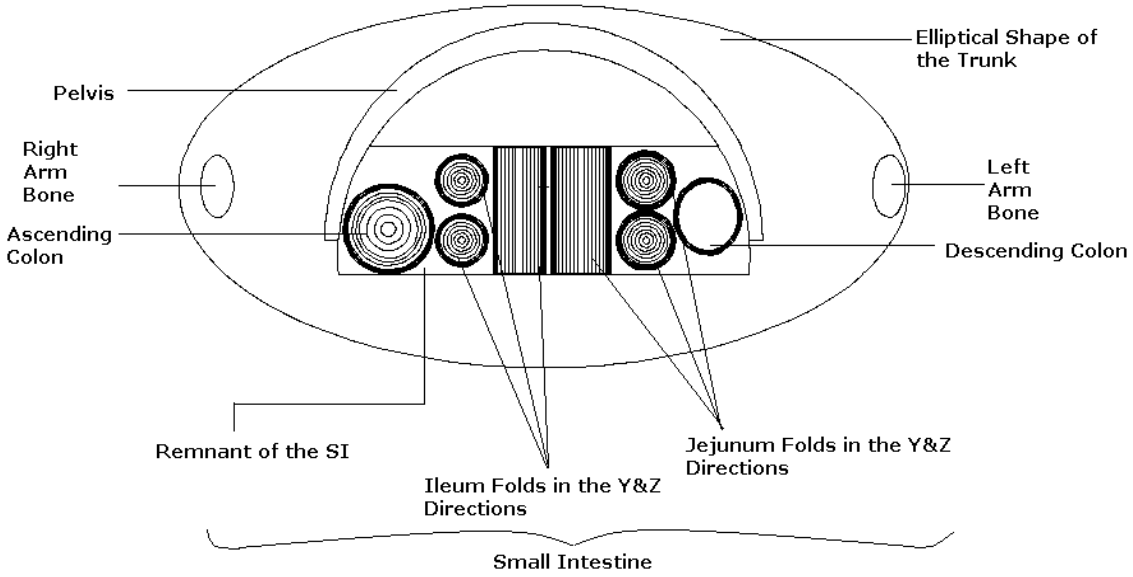


**Fig. I-9.** Pelvis and the intestine in the lower trunk region sectioned along the transverse plane z = 18.85 cm of the phantom. Three folds in the y and z directions for each of the ileum and jejunum are shown. Two more folds in the x-direction, located on z = 22.15 cm, for the ileum are not shown. Solid black rings represent the walls of the intestine. Each wall is divided into many small tissue layers by these cylinders. The contents surrounded by the wall also are divided into many small regions so that the dose profile of the contents can be established. The remnant of the SI is a solid soft tissue region representing that part of the SI where the lumen is empty and closed.

The upper portion of the **duodenum contents,** one quarter of a torus, is defined by:

$$\left(\sqrt{(x)^2+(z-32.6)^2}-4.3\right)^2+(y)^2 < (1.5)^2,$$

and $x \le 0,$ and $z \ge 32.6$.

The lower portion of the **duodenum contents,** one half of the torus, is defined by:

$$\left(\sqrt{(x)^2 + (z-32.6)^2} - 4.3\right)^2 + (y)^2 < (1.5)^2,$$

and $z \le 8.72.$

Thus, the **duodenum** is 20.26 cm long, with a wall thickness of 0.3 cm and a wall mass of 64.9 g with a density of 1.03 g $cm^{-3}$. The lumen radius is 1.5 cm with a mass of contents of 149 g and a density of 1.04 g $cm^{-3}$.

The **jejunum wall** is defined by:

$$\left.\begin{array}{l} (x-2.0333)^2 + (z-18.85)^2 \le (1.65)^2, \\ (x-2.0333)^2 + (z-18.85)^2 \ge (1.35)^2, \\ -4.83 \le y \le 2.17, \end{array}\right\} \text{One jejunal loop 7 cm in length in the y-direction}$$

$$\left.\begin{array}{l} (x-5.6)^2 + (y+2.98)^2 \le (1.65)^2, \\ (x-5.6)^2 + (y+2.98)^2 \ge (1.35)^2, \\ (x-5.6)^2 + (y-0.32)^2 \le (1.65)^2, \\ (x-5.6)^2 + (y-0.32)^2 \ge (1.35)^2, \\ \text{and } 17.0 \le z \le 24.0. \end{array}\right\} \text{Two jejunal loops, each 7 cm in length, in the z-direction}$$

The **jejunum contents** are defined by:

$$\left.\begin{array}{l} (x-2.0333)^2 + (z-18.85)^2 < (1.35)^2, \\ -4.58 \le y \le 1.92, \end{array}\right\} \text{One jejunal lumen 6.5 cm in length in the y-direction}$$

$$\left.\begin{array}{l}(x-5.6)^2+(y+2.98)^2<(1.35)^2,\\ (x-5.6)^2+(y-0.32)^2<(1.35)^2,\\ \text{and } 17.25\le z\le 23.75.\end{array}\right\}\text{Two jejunal lumens, each 6.5 cm in length, in the z-direction}$$

Thus, the jejunum is 21.0 cm long, with a wall thickness of 0.3 cm and a wall mass of 61.2 g with a density of 1.03 g $cm^{-3}$. The lumen is 19.5 cm long, with a radius of 1.35 cm, with a mass of contents of 116 g and a density of 1.04 g $cm^{-3}$.

The **ileum wall** is defined by:

$$\left.\begin{array}{l}(x+1.333)^2+(z-18.85)^2\le(1.45)^2,\\ (x+1.333)^2+(z-18.85)^2\ge(1.20)^2,\\ -4.83\le y\le 2.17,\end{array}\right\}\text{One ileum loop 7 cm in length in the y-direction}$$

$$\left.\begin{array}{l}(y+2.98)^2+(z-22.15)^2\le(1.45)^2,\\ (y+2.98)^2+(z-22.15)^2\ge(1.20)^2,\\ (y-0.32)^2+(z-22.15)^2\le(1.45)^2,\\ (y-0.32)^2+(z-22.15)^2\ge(1.20)^2,\\ \text{and } -3.05\le x\le 3.95.\end{array}\right\}\text{Two ileum loops, each 7 cm in length, in the x-direction}$$

$$\left.\begin{array}{l}(x+4.5)^2+(y-0.32)^2\le(1.45)^2,\\ (x+4.5)^2+(y-0.32)^2\ge(1.20)^2,\\ (x+4.5)^2+(y+2.98)^2\le(1.45)^2,\\ (x+4.5)^2+(y+2.98)^2\ge(1.20)^2,\\ \text{and } 17.0\le z\le 24.0.\end{array}\right\}\text{Two ileum loops, each 7 cm in length, in the z-direction}$$

The **ileum contents** is defined by

$$\left.\begin{array}{l}(x+1.333)^2+(z-18.85)^2<(1.20)^2,\\ -4.58\le y\le 1.92,\end{array}\right\}$$ One ileum lumen 6.5 cm in length in the y-direction

$$\left.\begin{array}{l}(y+2.98)^2+(z-22.15)^2<(1.20)^2,\\ (y-0.32)^2+(z-22.15)^2<(1.20)^2,\\ \text{and } -2.80\le x\le 3.70.\end{array}\right\}$$ Two ileum loops, each 6.5 cm in length, in the x-direction

$$\left.\begin{array}{l}(x+4.5)^2+(y-0.32)^2<(1.20)^2,\\ (x+4.5)^2+(y+2.98)^2<(1.20)^2,\\ \text{and } 17.25\le z\le 23.75.\end{array}\right\}$$ Two ileum loops, each 7 cm in length, in the z-direction

Thus, the ileum is 35.0 cm long, with a wall thickness of 0.25 cm and a wall mass of 75 g with a density of 1.03 g $cm^{-3}$. The lumen is 32.5 cm long, with a radius of 1.20 cm, with a mass of contents of 153 g and a density of 1.04 g $cm^{-3}$.

The **"remnant"** of the jejuno-ileum region is represented by a section of a circular cylinder, defined by

$$(x)^2+(y+3.80)^2\le(11.30)^2,$$

$$-4.86\le y\le 2.20,$$

$$\text{and } 17.0\le z\le 27.0.$$

The jejuno-ileum region with lumen and the portion of the large intestine within this region are excluded. The volume of the remnant is 642.24 $cm^3$.

**Large Intestine**

*Anatomic and histologic information.* The large intestine frames the jejuno-ileum region of the small intestine superiorly and laterally and extends about 1.5 m from the ileocecal valve to the anus. It is shorter in length but larger in diameter than the small intestine. The large intestine is spatially subdivided into the upper large intestine, consisting of the cecum, ascending colon, and transverse colon, and the lower large intestine, consisting of the descending colon, sigmoid colon, and rectum. Its major function is to absorb water from undigested material, which is eliminated from the body through the anus. As in the small intestine, the large intestine mucosa are covered by simple columnar epithelial cells, except the anal canal which is lined with more abrasion-resistant stratified squamous epithelial cells. The surface epithelium consists of absorptive and mucus-secreting goblet cells. Epithelial invaginations form long, straight, tubular glands or crypts than contain numerous goblet cells. The crypts that extend the full thickness of the mucosa vary in length (in the range of 300-700 μm), but are longer than in the small intestine (Trier and Winter 1989; Magee 1986; Christen 1991; ICRP HAT document 2001). The radiosensitive stem cells are located at the base of the crypts in the large intestine while those in the small intestine are slightly above the base of the crypts (Kaur and Potten 1986).

Unlike the small intestine, the mucosa of the colon lack villi and circular folds (plicae circulares), thus the surface appears flat. The rectal mucosa are similar to that of the colon but its mucosa lies in circular folds, and its glands are longer and are composed

almost entirely of goblet cells (ICRP 1975; Graaff and Fox 1999; ICRP HAT document 2001).

Goblet cells are abundant in the epithelium of the large intestine, in that mucus is needed to lubricate the lumenal surfaces and to protect the wall from acids and gases released by resident bacteria. The entire epithelium of the large intestine, and to a lesser extent the ileum, is covered with very thick mucus layer. The mucus thickness of proximal colon of rats was found to be 830±120 μm from *in vivo* measurements of 11 subjects (male Wister rats weighing ~200 g fasted for 18-24 h) using a micropipette technique with intravital microscopy (Atuma et al. 2001). This mucus layer was up to 4-fold thicker compared with that in other regions of the gut (Atuma et al. 2001). Atuma et al. (2001) noted that most of the difference in mucus thickness was due to loosely adherent mucus, which is one of the two components forming the mucus layer. The loosely adherent gel, which can be removed by suction and is rapidly replaced after removal, might have more lubricative properties *in vivo* and an underlying firmly adherent gel, which forms a thick layer over the gastric and colonic mucosal surfaces, would be expected to act as a relatively stable protective barrier (Atuma et al. 2001). The relative thickness of the two component layers of the mucus gel varies for different regions of the gut. Atuma et al. (2001) had to remove 86% of the mucus layer by suction to leave a firmly adherent gel of similar thickness to that in the stomach.

Pullan et al. (1994) measured the thickness of the adherent mucus gel on the colonic mucosa in the human. Their measured adherent mucus thicknesses were 107 μm on the surface of the "right colon" consisting of the ascending colon plus the proximal

half of the transverse colon, 134 μm on the surface of the "left colon" consisting of the distal half of the transverse colon plus the descending colon, and 155 μm on the surface of the rectum. Their study did not indicate whether these thicknesses were for the loosely adherent or firmly adherent or the total gel layer. If these were for firmly adherent gel layers (which might be the case because the overlying sloppy mucus gel may be lost in the process of specimen preparation), the total mucus thicknesses would be, respectively, 764 μm, 957 μm, and 1107 μm, based on the assumption that loosely adherent gel constitutes the 86% of the mucus layer as shown by Atuma et al. (2001).

Christensen (1991) showed that mucus thickness on the mucosal surface of the large intestine varies between 300 and 400 μm. Stubbs et al. (1998) arbitrarily chose 200 μm as the colonic mucus thickness.

In summary, the mucus layer is much thicker in the large intestine than any other section of the GIT but it is hard to find a single value for the mucus thickness of the entire large intestine as the thickness varies along the length of the section and between two measurements that employed different techniques. However, for the sake of simplicity, it is assumed that the entire mucosa of the large intestine is covered by a uniform mucus layer 500 μm thick.

The parameters describing the four segments of the large intestine (AC, TC, DC, RSC) in the new model, and in various other models and references are presented in Table I-6. This table shows that there are two values each for the length, wall mass and mass of contents in the new model. The value outside the parentheses is the actual value used for dose calculations. This value will be called the model value. The other value,

within the parentheses, is used for MCNP simulation. The wall is composed of ICRU recommended GIT material (ICRU 1989) with mass density, 1.03 g/cm$^3$, while the contents are composed of soft tissue with mass density, 1.04 g/cm$^3$ defined by Cristy and Eckerman (1987). The model length is based on the data given in the ICRP HAT document (2001) and ICRP Publication 23 (1975). The masses of the walls and the contents are taken directly from the ICRP HAT document (2001). The locations, geometric shapes, and the outer dimensions are taken directly from the Cristy and Eckerman models (1987). The wall thicknesses and the lumen dimensions are derived from the other known parameters. The transit times are taken directly from the gastrointestinal model proposed by Stubbs et al. (1991, 1992). The mucus thicknesses are based on a number of different studies (Christensen 1991; Pullan et al. 1994; Atuma et al. 2001). The crypt depths were provided by Potten and Booth in a personal communication (2000).

*Large intestine model.* The ULI consists of the ascending colon (AC) and transverse colon (TC), while the LLI consists of the descending colon (DC) and recto-sigmoid colon (RSC). As indicated previously, Cristy and Eckerman (1987) considered only the organ masses in their model. They ignored the other structural parameters such as length (and wall mass per unit length), wall thickness, and lumen diameter. The lumens were full in their model. The contents masses were different from the actual masses. The Monte Carlo simulation results were not corrected for these deviations. In this study, the large intestine was modeled more realistically. All parameters, except the length, were based on the anatomy and histology of the organ. The lengths used for Monte Carlo

simulation were the same as those in the Cristy and Eckerman model. These lengths were much shorter than the real anatomic length. But the wall mass per unit length and the source concentration closely match the anatomic data. However, appropriate factors are applied to the simulation results to correct for the deviations in the length. In the current model, the lumens, except the lumen of the RSC, are partly filled and partly empty. The RSC lumen is entirely filled in this model.

The **ascending colon (AC)** was modeled as two coaxial circular cylinders along the z-axis with the center at (-8.50, -2.36, 19.225). The cylinders were 9.55 cm long with radii 2.50 cm and 2.25 cm. The **AC wall** was defined by the space between the two cylinders:

$$(x+8.50)^2+(y+2.36)^2 \le (2.50)^2,$$

$$(x+8.50)^2+(y+2.36)^2 \ge (2.25)^2,$$

$$\text{and } 14.45 \le z \le 24.0.$$

The lumen was defined by the space within the inner cylinder. The lumen was only 9.30 cm long because the inferior end of the AC was closed by wall material of similar composition and thickness (0.25 cm). The **AC lumen** was given by:

$$(x+8.50)^2+(y+2.36)^2 < (2.25)^2,$$

$$\text{and } 14.7 \le z \le 24.0.$$

The lumen contains 60 g of contents only in its middle part which is 3.63 cm in length. Either side was empty. Each empty side is 2.835 cm in length. The **AC contents** were

**Table I-6.** Parameters describing the adult human large intestine in the new model and in other models and references.

| Segment | Reference | Length (cm) | Wall Mass (g) | Wall Thickness (cm) | Geometry | Lumen Radius (cm) | Contents Mass (g) | Transit Time (h) | Mucus Thickness (μm) | Crypt Depth (μm) | Stem Cell (μm) |
|---|---|---|---|---|---|---|---|---|---|---|---|
| Cecum + AC | HAT (2001) | 20 | 90 | — | — | — | 60 | 5 | — | — | — |
| | ICRP 23 (1975) | 7+18 | 90 | — | — | 2.5-3.5 (cecum) | — | — | — | — | — |
| | Cristy-Eckerman Model (1987) | 9.55 | 94.87 | 0.7085 | Circular Cylinder | 1.7915 | 100.14 | — | — | — | — |
| | Other | — | — | — | — | — | — | 8.4<br>AC: 5 | 830± 120 | AC: 311±64 | — |
| | New Model | 23.42 (9.55) | 90 (36.70) | 0.25 | Circular Cylinder | 2.25 | 60 (60.04) | 8.4 | 500 | 311± 64 | 811±64 |
| TC | ICRP HAT | 50 | 120 | — | — | — | 90 | 13 | — | — | — |
| | ICRP 23 | 50 | 120 | — | — | — | — | — | — | — | — |
| | Cristy-Eckerman Model (1987) | 21 | 125.58 | 0.527 | Elliptical Cylinder | 1.973, 0.973 | 131.72 | — | — | — | — |
| | Other | — | — | — | — | — | — | 12<br>7.3 | — | — | — |
| | New Model | 50 (21) | 120 (50.42) | 0.195 | Elliptical Cylinder | 2.305, 1.305 | 90 (90.02) | 7.3 | 500 | 325 | 825 |
| ULI: Cecum + AC + TC | ICRP HAT | 70 | 210 | — | — | — | 150 | 18 | — | — | — |
| | ICRP 23 | 75 | 210 | — | — | — | 220 | 13 | — | — | — |
| | Cristy-Eckerman Model (1987) | 30.55 | 220.45 | — | — | — | 231.86 | 17<br>15.7 | — | — | — |
| | Other | — | — | — | — | — | — | — | 764 | — | — |
| | New Model | 73.42 (30.55) | 210 (87.12) | — | — | — | 150 (150.07) | 15.7 | 500 | — | 818 |
| DC | ICRP HAT | 20 | 90 | — | — | — | 25 | 6 | — | — | — |
| | ICRP 23 | 30 | 90 | — | — | — | — | — | — | — | — |
| | Cristy-Eckerman Model (1987) | 15.28 | 93.55 | 0.54 | Elliptical Cylinder | 1.34, 1.59 | 106.37 | — | — | — | — |
| | Other | — | — | — | — | — | — | 4.3[7] | — | — | — |
| | New Model | 29.6 (15.28) | 90 (46.48) | 0.25 | Elliptical Cylinder | 1.88, 1.63 | 25 (25.03) | 4.3 | 500 | 340 | 840 |

**Table I-6** —*continued*

| Segment | Reference | Length (cm) | Wall Mass (g) | Wall Thickness (cm) | Geometry | Lumen Radius (cm) | Contents Mass (g) | Transit Time (h) | Mucus Thickness (μm) | Crypt Depth (μm) | Stem Cell (μm) |
|---|---|---|---|---|---|---|---|---|---|---|---|
| SC + R | ICRP HAT | 60 | 70 | — | — | | 70 | 12 | — | — | — |
| | ICRP 23 | 40+15 | 70 | — | — | R: 1.25-3.75 | — | — | — | — | — |
| | Cristy-Eckerman Model (1987) | 13.7 | 73.22 | 0.66 | Circular Torus | 0.91 | 37.06 | — | — | — | — |
| | Other | — | — | — | — | — | — | 11.6<br>10.9±1.6 | R: 1107 | SC: 358±84<br>R: 245±55 | — |
| | New Model | 55.4 (13.7) | 70.15 (17.34) | 0.13 | Circular Torus | 1.44 | 70 (92.8) | 11.5 | 500 | 327±63 | 827±63 |
| LLI: DC + SC + R | ICRP HAT | 80 | 160 | — | — | — | 95 | 18 | — | — | — |
| | ICRP 23 | 85 | 160 | — | — | — | 135 | 24 | — | — | — |
| | Cristy-Eckerman Model (1987) | 28.98 | 166.77 | — | — | — | 143.43 | 20<br>15.9 | — | — | — |
| | Other | | | — | — | — | — | — | 957 | — | — |
| | New Model | 85 (28.98) | 160.15 (63.82) | — | — | — | 95 (117.83) | 15.8 | 500 | — | 830 |
| LI: ULI + LLI | ICRP HAT | 150 | 370 | — | — | — | 245 | 36 | — | 500 | — |
| | ICRP 23 | 160 | 370 | 0.2-0.25<br>0.1 | — | — | 355 | 37 | — | — | — |
| | Cristy-Eckerman Model (1987) | 59.53 | 387.22 | — | — | — | 375.29 | 31.6<br>37.0<br>39±5 | — | — | — |
| | Other | 10[20] | 139 | 0.5<br><0.30 | Circular Cylinder | 1.90<br>4.0<br>3.25 | 523 | — | 200<br>300-400 | 700<br>500<br>500<br>320-345<br>500 | 550<br>300-500 |
| | New Model | 158.42 (59.53) | 370.15 (150.94) | — | — | — | 245 (267.9) | 31.5 | 500 | — | — |

given by:

$$(x+8.50)^2+(y+2.36)^2<(2.25)^2,$$

$$\text{and } 17.41\le z\le 21.04.$$

The ascending colon had a wall-thickness of 0.25 cm with a mass of the contents of 60 g.

The **transverse colon (TC)** was modeled as two coaxial elliptical cylinders along the x-axis with the center at (0, -2.36, 25.0). The elliptical cylinders were 21.0 cm in length with the radii 2.305 cm and 1.305 cm for the inner cylinder and 2.50 cm and 1.50 cm for the outer cylinder. The **TC wall** was defined by the space between the two cylinders:

$$\left(\frac{y+2.36}{2.50}\right)^2+\left(\frac{z-25.0}{1.50}\right)^2\le 1,$$

$$\left(\frac{y+2.36}{2.305}\right)^2+\left(\frac{z-25.0}{1.305}\right)^2\ge 1,$$

$$\text{and } -10.50\le x\le 10.50.$$

The lumen was defined by the space within the inner cylinder. The lumen was only 20.61 cm long because both ends of the TC were closed by wall material of similar composition and thickness (0.195 cm). The **TC lumen** was given by

$$\left(\frac{y+2.36}{2.305}\right)^2+\left(\frac{z-25.0}{1.305}\right)^2<1,$$

$$\text{and } -10.305\le x\le 10.305.$$

The lumen contains 90 g of contents only in its middle part which is 9.16 cm in length. Either side is empty. Each empty side is 5.725 cm in length. The **TC contents** are given by:

$$\left(\frac{y+2.36}{2.305}\right)^2+\left(\frac{z-25.0}{1.305}\right)^2<1,$$

$$\text{and } -4.58\le x\le 4.58.$$

The transverse colon had a wall thickness of 0.195 cm and the mass of the contents was 90 g.

The **descending colon (DC)** was modeled as two coaxial elliptical cylinders with the axis tilted at a small angle with the z-axis of the phantom, but the ends were defined by two horizontal planes (z = 8.72 and z = 24). The wall was defined by the space between the two cylinders with semiradii 1.88 cm and 2.13 cm (outer), and 1.63 cm and 1.88 cm (inner):

$$\left(\frac{x-x_0}{1.88}\right)^2+\left(\frac{y-y_0}{2.13}\right)^2\le 1,$$

$$\left(\frac{x-x_0}{1.63}\right)^2+\left(\frac{y-y_0}{1.88}\right)^2\ge 1,$$

$$\text{and } 8.72\le z\le 24,$$

where

$$x_0=9.25+\frac{0.78(z-24)}{15.28}$$

$$\text{and } y_0=\frac{2.50(8.72-z)}{15.28}.$$

The **DC lumen** was defined by the space within the inner cylinder:

$$\left(\frac{x-x_0}{1.63}\right)^2+\left(\frac{y-y_0}{1.88}\right)^2<1,$$

$$\text{and } 8.72\le z\le 24.$$

The lumen contains 25 g of contents only in its middle part, which is about 2.5 cm in length. Either side is empty. The **DC contents** were given by:

$$\left(\frac{x-x_0}{1.63}\right)^2+\left(\frac{y-y_0}{1.88}\right)^2<1,$$

$$\text{and } 15.11\le z\le 17.61.$$

The descending colon had a wall-thickness of 0.25 cm and the mass of the contents was 25 g.

The **recto-sigmoid colon (RSC)** consists of two regions — upper and lower. The wall plus contents of each region was represented by one-quarter of two concentric circular tori. The wall was defined by the space between the tori. The contents were defined by the space within the inner torus.

*Upper region*

The **RSC wall** was defined by:

$$\left(\sqrt{(x-3.0)^2+(z-8.72)^2}-5.72\right)^2+(y)^2\le(1.57)^2,$$

$$\left(\sqrt{(x-3.0)^2+(z-8.72)^2}-5.72\right)^2+(y)^2\ge(1.44)^2,$$

$$x\ge 3.0,\ \text{and}\ z\le 8.72.$$

The **RSC contents** were defined by:

$$\left(\sqrt{(x-3.0)^2+(z-8.72)^2}-5.72\right)^2+(y)^2<(1.44)^2,$$

$$x\ge 3.0,\ \text{and}\ z\le 8.72.$$

*Lower region*

The **RSC wall** was defined by:

$$\left(\sqrt{(x-3.0)^2+(z)^2}-3.0\right)^2+(y)^2 \le (1.57)^2,$$

$$\left(\sqrt{(x-3.0)^2+(z)^2}-3.0\right)^2+(y)^2 \ge (1.44)^2,$$

$$x \le 3.0, \text{and } z \ge 0.$$

The **RSC contents** were defined by:

$$\left(\sqrt{(x-3.0)^2+(z)^2}-3.0\right)^2+(y)^2 < (1.44)^2,$$

$$x \le 3.0, \text{ and } z \ge 0.$$

The recto-sigmoid colon had a wall-thickness of 0.13 cm and the mass of the contents was 93 g.

ELEMENTAL COMPOSITION OF THE TISSUES

The first heterogeneous phantom, developed by Snyder et al. (1969), contained three regions each assigned a different density and elemental composition. These regions represented the tissues of the skeleton, the lung, and the remainder (soft tissue). The elemental compositions were obtained from Tipton, Snyder, and Cook (1966), who analyzed tissue specimens obtained from autopsies of 150 grossly normal U.S. adults. Cristy and Eckerman (1987) used the same three tissue types but with slightly different elemental compositions and densities in the revised Snyder phantom. The changes were made on the basis of data in Table 105 of ICRP Publication 23 (1975).

The new phantom contains 14 different types of tissue that include the tissues of skeleton, lung and soft tissue defined by Cristy and Eckerman (1987) and 11 other tissue types listed in the International Commission on Radiation Units and Measurements (ICRU) Report 44 (1989). The ICRU recommended elemental compositions and the densities were derived from the ICRP Report on Reference Man (1975) and from the work of Woodard and White (1986) on body tissue compositions. The soft tissue defined by Cristy and Eckerman (1987) is used for the GIT contents while the ICRU (1989) recommended tissue is used for the GIT wall, except the wall of the esophagus. In the absence of more appropriate of data, as recommended by ICRU (1989), ICRU skeletal muscle tissue was used for the esophageal wall and the urinary bladder wall.

Table I-7 presents the elemental compositions and the densities of different tissues used in the new model, the Cristy and Eckerman model (1987) and the Snyder et al. model (1969).

**Table I-7.** The elemental compositions and the mass densities of adult human organs and tissues used in the new model and in other models.

| Model and reference | Tissue | Elemental composition (percentage by mass) | | | | | Density ($g\ cm^{-3}$) |
|---|---|---|---|---|---|---|---|
| | | H | C | N | O | Other | |
| ICRU Report (1989) | Brain | 10.7 | 14.5 | 2.2 | 71.2 | 0.2 Na, 0.4 P, 0.2 S, 0.3 Cl, 0.3 K | 1.04 |
| | Breast | 10.6 | 33.2 | 3.0 | 52.7 | 0.1 Na, 0.1 P, 0.2 S, 0.1 Cl | 1.02 |
| | GIT wall | 10.6 | 11.5 | 2.2 | 75.1 | 0.1 Na, 0.1 P, 0.1 S, 0.2 Cl, 0.1 K | 1.03 |
| | Heart (blood filled) | 10.3 | 12.1 | 3.2 | 73.4 | 0.1 Na, 0.1 P, 0.2 S, 0.3 Cl, 0.2 K, 0.1 Fe | 1.06 |
| | Kidney | 10.3 | 13.2 | 3.0 | 72.4 | 0.2 Na, 0.2 P, 0.2 S, 0.2 Cl, 0.2 K, 0.1 Ca | 1.05 |
| | Liver | 10.2 | 13.9 | 3.0 | 71.6 | 0.2 Na, 0.3 P, 0.3 S, 0.2 Cl, 0.3 K | 1.06 |
| | Muscle (skeletal) | 10.8 | 4.1 | 1.1 | 83.2 | 0.3 Na, 0.1 S, 0.4 Cl | 1.05 |
| | Ovary | 10.5 | 9.3 | 2.4 | 76.8 | 0.2 Na, 0.2 P, 0.2 S, 0.2 Cl, 0.2 K | 1.05 |
| | Pancreas | 10.6 | 16.9 | 2.2 | 69.4 | 0.2 Na, 0.2 P, 0.1 S, 0.2 Cl, 0.2 K | 1.04 |
| | Testes | 10.6 | 9.9 | 2.0 | 76.6 | 0.2 Na, 0.1 P, 0.2 S, 0.2 Cl, 0.2 K | 1.04 |
| | Thyroid | 10.4 | 11.9 | 2.4 | 74.5 | 0.2 Na, 0.1 P, 0.1 S, 0.2 Cl, 0.1 K, 0.1 I | 1.04 |
| Cristy and Eckerman (1987) | Soft tissue | 10.5 | 22.7 | 2.5 | 63.5 | 0.1 Na, 0.1 P, 0.2 S, 0.1 Cl, 0.2 K | 1.04 |
| | Skeleton | 7.4 | 25.5 | 3.1 | 47.9 | 0.3 Na, 0.1 Mg, 5.1 P, 0.2 S, 0.1 Cl, 0.2 K, 10.2 Ca | 1.40 |
| | Lung | 10.1 | 10.2 | 2.9 | 75.8 | 0.2 Na, 0.1 P, 0.2 S, 0.3 Cl, 0.2 K | 0.296 |
| Snyder et al. (1974) | Soft tissue | 10.0 | 23.0 | 2.3 | 63.0 | 0.1 Na, 0.2 P, 0.2 S, 0.1 Cl, 0.2 K | 0.9869 |
| | Skeleton | 7.0 | 23 | 3.9 | 49.0 | 0.3 Na, 0.1 Mg, 6.9 P, 0.2 S, 0.1 Cl, 0.2 K, 9.9 Ca | 1.4862 |
| | Lung | 10 | 10 | 2.8 | 76 | 0.2 Na, 0.1 P, 0.2 S, 0.3 Cl, 0.2 K | 0.296 |

# BIBLIOGRAPHY


Alberts B, Bray D, Lewis J, Raff M, Roberts K, Watson JD. Molecular biology of the cell. 2nd ed. New York: Garland Publishing, Inc.; 1989: 614.

Alpen EL. Radiation biophysics. 2nd ed. San Diego, California: Academic Press, Inc.; 1998: 247-259.

Allen A. The gastrointestinal system. In: Schultz SG, Forte JG, Rauner BB. eds. Handbook of physiology. vol. III, Section 6. Bethesda, MD: Am. Physiol. Soc.; 1989:359-382.

Atuma C, Strugala V, Allen A, Holm L. The adherent gastrointestinal mucus gel layer: thickness and physical state in vivo. Am J Physiol Gastrointest Liver Physiol 280: G922-G929; 2001.

Balaban D, Yammamoto Y, Liu J, Pehlivanov N, Mittal RK. Identification of sustained esophageal contraction at the time of chest pain using high frequency intraluminal ultrasonography. Gastroenterology. 116:29-37; 1999.

Barrett KE, Donowitz M. Gastrointestinal transport, molecular physiology Vol 50. San Diego: Academic Press, 2000.

Berger MJ, Seltzer MS. Bremsstrahlung and photoneutrons from thick tungsten and tantalum targets. Phys Rev. C2:621-631; 1970.

Berger MJ, Seltzer SM. ETRAN, Monte Carlo code system for electron and photon transport through extended media. Oak Ridge, Tennessee: Oak Ridge Natl. Lab.; Documentation for RSIC computer code package, CCC-107; 1973.

Berger MJ, Wang R. Multiple-scattering angular deflections and energy-loss straggling in electron transport calculations. In: Nelson WR, Jenkins TM, Rindi A, Nahum AE, Rogers DWO, eds. Monte Carlo transport of electrons and photons below 50 MeV. New York: Plenum Press; 1989: 21-56.

Bickel M, Kauffman GL. Gastric gel mucus thickness: effect of distension, 16-16 dimethyl prostaglandin $E_2$ and carbenoxolone. Gastroenterology. 80:770-775; 1981.

Bolch WE. The anatomical and physiological bases for internal dosimetry. In: Bolch WE. ed. Practical applications of internal dosimetry. Madison, Wisconsin: Medical Physics Publishing, Health Physics Society; 2002: 14-23.

Blomquist RN, Gelbard EM. An assessment of existing Klein-Nishina Monte Carlo sampling methods. Nucl Sci Eng 83:380; 1983.

Briesmeister JF. ed. MCNP—A general Monte Carlo N-particle transport code. Version 4B. Los Alamos, NM: Los Alamos National Laboratory; Report LA-12625-M; 1997.

Carlson, T. A. Photoelectron and Auger spectroscopy. New York: Plenum Press; 1975.

Cheng H, Leblond CP. Origin, differentiation and renewal of the four main epithelial cell types in the mouse small intestine. V. Unitarian theory of the origin of the four epithelial cell types. Am. J. Anat. 141:537-561; 1974.

Christensen J. The large intestine: Physiology, pathophysiology, and disease. New York: Raven Press, 1991.

Coffey JL. A revised mathematical model of the heart for use in radiation absorbed dose calculations. M. S. Thesis, Knoxville, TN: University of Tennessee; 1978.

Colbert HM. SANDYL, a computer program for calculating combined photon-electron transport in complex system. Livermore, California: Sandia Laboratories; Sandia Rep SLL-74-0012; 1974.

Cristy M. Mathematical phantoms representing children of various ages for use in estimates of internal dose. U.S. Nuclear Regulatory Commission Rep. NUREG/CR-1159 (also Oak Ridge National Laboratory Rep. ORNL/NUREG/TM-367); 1980.

Davies H, Bethe HA, Maximom LC. Theory of bremsstrahlung and pair production. Phys Rev 93:788; 1954a.

Davies H, Bethe HA, Maximom LC. Integral cross section for pair production. Phys Rev 93; 1954b.

Ellett WH, Callahan AB, Brownell GH. Gamma-ray dosimetry of internal emitters: Monte Carlo calculations of absorbed dose from point sources. Brit. J. Radiol. 37:45-52; 1964.

Ellett WH, Callahan AB, Brownell GH. Gamma-ray dosimetry of internal emitters II: Monte Carlo calculations of absorbed dose from uniforms sources. Brit. J. Radiol. 38:541-544; 1965.

Ewart GM, Rogers DWO. Calculated thick target bremsstrahlung angular distributions and shielding calculations. Ottawa, Canada: National Research Council of Canada; Rep. PXNR-2640; 1982.

Eve, I. S. A review of the physiology of the gastrointestinal tract in relation to radiation doses from radioactive material. Health Phys. 12:131-161; 1966.

Everett CJ, Cashwell ED. MCP code fluorescence-routine revision. Los Alamos, New Mexico: Los Alamos Scientific Laboratory; LA-5240-MS; 1973.

Fawcett, D. W. A textbook of histology. 12th ed. New York: Chapman & Hall; 1994: 617-636.

Fisher HL, Snyder WS. Distribution of dose in the body from a source of gamma rays distributed uniformly in an organ. Oak Ridge, Tennessee: Oak Ridge National Laboratory; ORNL-4168/UC-41; 1967.

Fisher HL, Snyder WS. Distribution of dose in the body from a source of gamma rays distributed uniformly in an organ. In: Proc. First Internat. Congr. Radiat. Protection. Rome, Italy, September 5-10, 1966; Oxford: Pergamon Press; 1968:1473-1486.

Flemstrom G, Hallgren A, Nylander O, Engstrand L, Wilander E, Allen A. Adherent surface mucus gel restricts diffusion of macromolecules in rat duodenum in vivo. Am. J. Physiol. Gastrointest. Liver Physiol. 277:G375-G382; 1999.

Florey H. Mucin and the protection of the body. Proc. R. Soc. (Biol.) (London); 143:144-158; 1955.

Ford RL, Nelson WR. The EGS code system (version 3). Stanford, California: Stanford University; SLAC Rep 210; 1978.

Goudsmit S, Saunderson JL. Multiple scattering of electrons. Phys Rev 57:24-29; 1940.

Ganong WF. Review of medical physiology. 9th ed. Palo Alto, California: Lange Medical Publications; 1979.

Glasgow JFT, Corkey CWB, Molla A. Critical assessment of small bowel biopsy in children. Arch. Dis. Child. 54:604-608; 1979.

Golden R. Radiological examination of the small intestine. 2nd ed. Springfield, Illinois: Thomas; 1959.

Gordon JI, Hermiston ML. Differentiation and self-renewal in the mouse gastrointestinal epithelium. Curr. Opin. Cell Biol. 6:795-803; 1994.

Graaff VD, Kent M, Fox SI. Concepts of human anatomy and physiology. 5th ed. New York: McGraw-Hill; 1999.

Gray H. Gray's anatomy. Philadelphia: Running Press; 1974: 911-921.

Grosswendt B, Waibel E. Determination of detector efficiencies for gamma-ray energies up to 12 MeV. Nucl Instrum Methods 131:143-156; 1975.

Guyton AC. Text book of medical physiology. 9th ed. Philadelphia: W. B. Saunders Company; 1996.

Halbleib JA, Vandevender WH. CYLTRAN-cylindrical geometry multimaterial electron of photon Monte Carlo transport code. Oak Ridge, Tennessee: Radiation Shielding Information Center, Oak Ridge National Laboratory; ORNL Rep CCC-280; 1976.

Halbleib JA, Melhorn TA. ITS: the integrated TIGER series of coupled electron/photon Monte Carlo transport codes. Albuquerque, New Mexico: Sandia National Laboratories; Sandia Rep SAND84-0073; 1984.

Haubrich WS, Schaffner F. Bockus gastroenterology. 5th ed. Philadelphia: W. B. Saunders Company; 1995: 885-892.

Hendricks JS. MCNP4B, LANL memorandum. Los Alamos, New Mexico: Los Alamos National Laboratory; 1997.

Hine GJ, Brownell GL. Radiation dosimetry. New York: Academic Press Inc.; 1956: 722-730.

Hollander F. The two component mucus barrier. Its activity in protecting the gastroduodenal mucosa against peptic ulceration. Arch. Int. Med. 93:107-120; 1954.

Hubbell JH, Veigele WJ, Briggs EA, Brown RT, Cromer DT, Howerton RJ. Atomic form factors, incoherent scattering functions, and photon scattering cross sections. J Phys Chem Ref Data 4:471-538; 1975.

Hubbell JH, Øverbo I. Relativistic atomic form factors and photon coherent scattering cross sections. J Phys Chem Ref Data 8:69-105; 1979.

Hughes HG, Prael RE, Little RC. MCNPX-The LAHET/MCNP code merger. Los Alamos, New Mexico: Los Alamos National Laboratory; XTM-RN(U) 97-012; 1997.

Hwang JML, Shoup RL, Poston JW. Modifications and additions to the pediatric and adult mathematical phantoms. Oak Ridge, Tennessee: Oak Ridge National Laboratory; ORNL/TM-5454; 1976.

International Commission on Radiological Protection (ICRP). Report of Committee II on permissible dose for internal radiation. Oxford: Pergamon Press; ICRP Publication 2; 1959.

International Commission on Radiation Units and Measurements. Stopping powers for electrons and positrons. Bethesda, Maryland; ICRU Report 37; 1984.

International Commission on Radiation Units and Measurements. Tissue substitutes in radiation dosimetry and measurement. Bethesda, Maryland; ICRU Publication 44; 1989.

Jabbur RJ, Pratt RH. High-frequency region of the spectrum of electron and positron bremsstrahlung. Phys Rev 129:184; 1963.

Jabbur RJ, Pratt RH. High-frequency region of the spectrum of electron and positron bremsstrahlung. Phys Rev 133:1090; 1964

Johnson LR, Christensen J, Jackson MJ, Jacobson ED, Walsh JH. Physiology of the gastrointestinal tract. 2nd ed. Vol. 2. New York: Raven Press; 1987: 975-1249.

Kahn H. Applications of Monte Carlo. The Rand Corporation; AEC-3259; 1956.

Kaur P, Potten CS. Cell migration velocities in the crypts of the small intestine after cytotoxic insult are not dependent on mitotic activity. Cell Tissue Kinet. 19:601-610; 1986.

Kerss S, Allen A, Garner A. A simple method for measuring thickness of the mucus gel layer adherent to rat, frog and human gastric mucosa: influence of feeding, prostaglandin, N-acetylcysteine and other agents. Clin. Sci. 63:187-195;1982.

Koblinger L. Direct sampling from the Klein-Nishina distribution for photon energies above 1.4 MeV. Nucl Sci Eng 56:218; 1975.

Landau L. On the energy loss of fast particles by ionization. J Phys (Moscow) 8:201-205; 1944.

Lawrence JH, Tennant R. The comparative effects of neutrons and X-rays on the whole body. J. Exp. Med. 66:667; 1937.

Leeson RC, Leeson TS, Paparo AA. Textbook of histology. 5th ed. Philadelphia: W. B. Saunders Company; 1985: 343-352.

Lipkin M, Sherlock P, Bell B. Cell renewal in stomach, ileum, colon, and rectum. Gastroenterology. 45:721; 1963.

Loevinger R, Berman MA. Schema for absorbed dose calculations from biologically distributed radionuclides. MIRD Pamphlet No. 1 New York: Society of Nuclear Medicine; 1968.

Loevinger R, Berman MA. Revised schema for calculating the absorbed dose from biologically distributed radionuclides. MIRD Pamphlet No. 1, Revised. New York: Society of Nuclear Medicine; 1976.

Marieb EN. Human anatomy and physiology. 4th ed. Reading, Massachusetts: Addison Wesley Longman, Inc.; 1998.

Martin CL, Rogers FT. Intestinal reaction to erythema dose. Amer. J. Roentgenol. 10:11; 1923.

McClean P, Dodge JA, Nunn S, Carr KE, Sloan JM. Surface features of small-intestinal mucosa in childhood diarrheal disorders. J Ped. Gastroent. Nut. 23:538-546; 1996.

MacDonald WC, Trier JS, Everett NB. Cell proliferation and migration in the stomach, duodenum, and rectum of man: radioautographic studies. Gastroenterology. 46:405; 1964.

Magee DF, Dalley AF. Digestion and the structure and function of the gut. Farmington, Connecticut: Karger Continuing Education Series, Vol 8. 1986.

Miller LS, Liu JB, Colizzo FP, Ter H, Marzano J, Barbarevech C, Hedwig K, Leung L, Goldberg BB. Correlation of high frequency esophageal ultrasonography and manometry in the study of esophageal motility. Gastroenterology. 105:832-837; 1995.

Moe H. On goblet cells, especially of the intestine of some mammalian species. Int. Rev. Cytol. 4:299-334; 1955.

Molière GZ. Theorie der Streuung Schneller Geladener Teilchen II Mehrfach- und Vielfachstreuung. Z Naturforsch A 3A:78-79; 1948.

Morel JE, Lorene LJ. Recent developments in discrete ordinates electron transport. Trans Am Nucl Soc 52: 384-385; 1986.

Morris GP, Harding PK, Wallace JL. A functional model for extracellular gastric mucus in the rat. Virchows Arch. (Cell Pathol.). 46:239-251; 1984.

Moussa HM, Eckerman KF, Townsend LW, Pevey R. Estimation of electron absorbed fractions in the extrathoracic airways. Health Phys. 80:12-15; 2001.

National Bureau of Standards. Maximum permissible body burdens and maximum permissible concentrations of radionuclides in air and in water for occupational exposure. Recommendations of the National Committee on Radiation Protection (NCRP), Handbook 69, U. S. Department of Commerce, June 5, 1959.

National Council on Radiation Protection and Measurements. Evaluating the reliability of biokinetic and dosimetric models and parameters used to assess individual doses for risk assessment purposes. Bethesda, Maryland: National Council on Radiation Protection and Measurements; NCRP Commentary No. 15; 1998.

Nelson WR, Hirayama H, Rogers DWO. The EGS4 code system. Stanford, California: Stanford Linear Accelerator Center; Report SLAC-265-UC-32; 1985.

Nicosia MA, Brasseur JG, Liu J, Miller LS. Local longitudinal muscle shortening of the human esophagus from high-frequency ultrasonography. Am. J Physiol Gastrointest Liver Physiol. 281:G1022-G1033; 2001.

Olsen H. Outgoing and ingoing waves in final states and bremsstrahlung. Phys Rev 99:1335; 1955.

Penna FJ, Hill ID, Kingston D, Robertson K, Slavin G, Shiner M. Jejunal mucosal morphometry in children with and without gut symptoms and normal adults. J Clin. Pathol. 34:386-392; 1981.

Pehlivanov N, Liu J, Kassab GS, Puckett JL, Mittal RK. Relationship between esophageal muscle thickness and intraluminal pressure: an ultrasonographic study. Am. J Physiol Gastrointest Liver Physiol. 280:G1093-G1098; 2001.

Potten CS. Extreme sensitivity of some intestinal crypts to X and γ-irradiation. Nature 269:518-521, 1977.

Potten CS. A comprehensive study of the radiological response of the murine (BDF1) small intestine. Int. J. Radiat. Biol. 58:925-973; 1990.

Potten CS, Booth C, Pritchard DM. The intestinal epithelial stem cells: the mucosal governor. Int. J. Exp. Pathol. 78:219-243, 1997a.

Potten CS, Wilson JW, Booth C. Regulation and significance of apoptosis in the stem cells of the gastrointestinal epithelium. Stem Cells 15:82-93, 1997b.

Potten CS, Booth C. Personal communication, Paterson Institute for Cancer Research, Manchester, England; 2000.

Prael RE, Lichtenstein H. User guide to LCS: The LAHET code system. Los Alamos, New Mexico: Los Alamos National Laboratory; LA-UR-893014; 1989.

Pratt RH, Tseng HK, Lee CM, Kissel L, MacCallum C, Riley M. Bremsstrahlung energy spectra from electrons of kinetic energy 1 keV ≤ T ≤ 2000 keV incident on neutral atoms 2 < Z < 92. Atom Data and Nucl Data Tables 20:175; 1977; errata in 26:477; 1981.

Pullan RD, Thomas GA, Rhodes M, Newcombe RG, Williams GT, Allen A, Rhodes J. Thickness of adherent mucus gel on colonic mucosa in humans and its relevance to colitis. Gut. 35:353-359; 1994.

Riley ME, MacCallum CJ, Biggs F. Theoretical electron-atom elastic scattering cross sections. Selected elements, 1 keV to 256 keV. Atom Data and Nucl Data Tables 15:443; 1975.

Rogers DWO. Low energy electron transport with EGS. Nucl Instrum Methods Phys Res A227: 535-548; 1984a.

Rogers DWO. Fluence to dose equivalent conversion factors calculated with EGS3 for electron from 100 keV to 20 GeV and photons from 11 keV to 20 GeV. Health Phys 46:891-914; 1984b.

Rogers DWO, Bielajew AF. Difference in electron depth-dose curves calculated with EGS and ETRAN and improved energy range relationships. Med Phys 13: 687-694; 1986.

Rogers DWO, Bielajew AF. Monte Carlo techniques of electron and photon transport for radiation dosimetry. In: Kase KR, Bjärngard, Attix FH, eds. The dosimetry of ionizing radiation. New York: Academic Press, Inc.; 1990: 427-539.

Ross MH, Reith ED. Histology: a text and atlas. New York: Harper & Row Publishers; J. B. Lippincott Company; 1985: 426-427.

Sakata T, Engelhardt WV. Luminal mucin in the large intestine of mice, rats, and guinea pigs. Cell Tissue Res. 219:629-635; 1981.

Seltzer SM, Berger MJ. Bremsstrahlung spectra from electron interactions with screened atomic nuclei and orbital electrons. Nucl. Instr. Meth. Phys. Res. B12:95-134; 1986.

Seltzer SM. Cross sections for bremsstrahlung production and electron impact ionization. In: Jenkins TM, Nelson WR, Rindi A, eds. Monte Carlo transport of electrons and photons. New York: Plenum Press; 1988a: 81.

Seltzer SM. An overview of ETRAN Monte Carlo methods. In: Jenkins TM, Nelson WR, Rindi A, eds. Monte Carlo transport of electrons and photon. New York: Plenum Press; 1988b: 153.

Seltzer SM. An overview of ETRAN Monte Carlo methods for coupled electron/photon transport calculation. In: Nelson WR, Jenkins TM, Rindi A, Nahum AE, Rogers DWO, eds. Monte Carlo transport of electrons and photons below 50 MeV. New York: Plenum Press; 1989: 151-181.

Shreider YA. ed. The Monte Carlo method. Oxford: Pergamon Press; 1966.

Smith EM. Activities of the medical internal radiation dose committee. MIRD Supplement No. 1. New York: Society of Nuclear Medicine; 1968.

Snyder WS, Ford MR, Warner GG, Fisher HL, Jr. Estimates of absorbed fractions for monoenergetic photon sources uniformly distributed in various organs of a heterogeneous phantom. MIRD Pamphlet No. 5. New York: Society of Nuclear Medicine; 1969.

Solomon EP, Davis PW. Understanding human anatomy and physiology. New York: McGraw-Hill Book Company; 1978: 316-334.

Stenling R, Fredrikzon B, Nyhlin H, Helander HF. Surface ultrastructure of the small intestine mucosa in healthy children and adults: a scanning electron microscopic study with some methodological aspects. Ultrastruct. Pathol. 6:131-140; 1984.

Sternheimer RM, Peierls RF. General expression for the density effect for the ionization loss of charged particles. Phys Rev B3:3681-3692; 1971.

Sternheimer RM, Berger MJ, Seltzer SM. Density effect of the ionization loss of charged particles in various substances. Phys Rev B26:6067; 1982.

Stubbs JB. A new mathematical model of gastrointestinal transit that incorporates age and gender-dependent physiological parameters. In: Watson EE, Schlafke-Stelson A, eds. Proceedings of the fifth international symposium on radiopharmaceutical dosimetry. National Technical Information Service, Springfield, Virginia; 1991: 229-242.

Stubbs JB. Results from a new mathematical model of gastrointestinal transit that incorporates age and gender-dependent physiological parameters. Radiat. Prot. Dosim. 41: 63-69 (1992).

Sullivan MF, Hackett PL, George LA, Thompson RC. Irradiation of the intestine by radioisotopes. Radiat. Res. 13: 343-355; 1960.

Takeuchi K, Magee D, Critchlow J, Matthews J, Silen W. Role of pH gradient of mucus in protection of gastric mucosa. Gastroenterology. 84:331-340; 1983.

Taniguchi DK, Martin RW, Trowers EA, Dennis MB, Odegaad S, Silverstein FE. Change in esophageal wall layer during motility: measurement with a new miniature ultrasound device. Gastrointest Endosc 39:146-152; 1993.

Tipton IH, Snyder WS, Cook MJ. Elemental composition of standard man. Oak Ridge, Tennessee: Oak Ridge National Laboratory, Health Phys. Div. Annu. Prog. Rep. ORNL-4007; 1966.

Tipton IH, Cook MJ. Weight of total gastrointestinal tract and its subfractions. Oak Ridge, Tennessee: Oak Ridge National Laboratory, Health Phys. Div. Annu. Prog. Rep. ORNL-4446; 1969.

Tortora G J, Evans RL. Principles of human physiology. 2nd ed. New York: Harper & Row Publishers; 1986: 608-613.

Trier JS, Winter HS. Anatomy, embryology, and developmental abnormalities of the small intestine and colon. In: Sleisenger MH, Fordtran JS. eds. Gastrointestinal disease – pathophysiology, diagnosis, and management. 4th ed. Philadelphia: W. B. Saunders Company; 1989: 991-1021.

Tseng HK, Pratt RH. Exact screened calculations of atomic-field bremsstrahlung. Phys Rev A3:100; 1971.

Tseng HK, Pratt RH. Electron bremsstrahlung from neutral atoms. Phys Rev Lett 33:516; 1974.

Tsuzuki M. Experimental studies on the biological action of hard roentgen rays. Amer. J. Roentgenol. 16:134;1926.

Vander AJ, Sherman JH, Luciano DS. Human physiology. 2nd ed. New York: McGraw-Hill; 1970.

Weber DA, Eckerman KF, Dillman LT, Ryman JC. MIRD: radionuclide data and decay schemes. New York: The Society of Nuclear Medicine; 1989.

Whitehead R. Gastrointestinal and oesophageal pathology. New York: Churchill Livingstone, 1989.

Yamamoto Y, Liu J, Smith TK, Mittal RK. Distension related responses in the circular and longitudinal muscles of the esophagus: an ultrasonographic study. Am. J. Physiol. Gastrointest Liver Physiol. 275:G805-G811; 1998.